Simulation of Slamming on a Fiber Reinforced Composite Structure Using the ALE/Eulerian Numerical Approach

submitted on July 18, 2019

by

LADEIRA Ícaro

Supervisor:
Pr. Hervé Le Sourne
ICAM Nantes

First Reviewer:
Pr. Patrick Kaeding
University of Rostock
Rostock, Germany

Second Reviewer:
Pr. Hervé Le Sourne
Institut Catholique d'arts et métiers
Nantes, France

developed at the Institut Catholique d'arts et métiers, Nantes
in the framework of the
"EMSHIP"
Erasmus Mundus Master Course
in "Integrated Advanced Ship Design"

MASTER THESIS

[This page intentionally left blank]

DECLARATION OF AUTHORSHIP

I, **Icaro José Ladeira Napoleão de Souza**, declare that this thesis and the work presented in it are my own and have been generated by me as the result of my own original research.

Where I have consulted the published work of others, this is always clearly attributed.

Where I have quoted from the work of others, the source is always given. With the exception of such quotations, this thesis is entirely my own work.

I have acknowledged all main sources of help.

Where the thesis is based on work done by myself jointly with others, I have made clear exactly what was done by others and what I have contributed myself.

This thesis contains no material that has been submitted previously, in whole or in part, for the award of any other academic degree or diploma.

I cede copyright of the thesis in favour of the University of Rostock.

Date: 18/07/2019

Signature: 

Contents

Abstract

Slamming impact on marine structures constitutes a major concern for designers. Characterized by severe impulsive loads with short duration, this highly non-linear fluid-structure interaction can lead to significant structural damage. Several analytical models have been developed to predict the loads generated on slamming events. However, existent models are still not sufficiently accurate to be applied on industrial level.

This thesis presents a numerical slamming model developed with the ALE/Eulerian approach on *LS-DYNA*. Primarily, the classical two-dimensional rigid wedge is used for an overview on the functioning of the applied penalty contact algorithm and calibration of its governing parameters. The model is validated through comparison with experimental results of the vertical slamming force available on the literature. Sensitivity analyses on parameters such as the penalty factor, damping coefficient and number of coupling points are performed. Additionally, simulations with a three-dimensional version of the rigid wedge are presented with the objective of demonstrating the influence of 3D flow effects on the resulting force. The models produce satisfactory results, reproducing fairly well the slamming force and the free-surface behavior on the rigid structure.

On a third stage, the model is applied to an elasto-plastic flat plate. Good agreement with experimental results is found for the hydro-elastic behavior of the plate. Accurate measurements of the local pressure, however, could not be obtained.

The model is finally extended to a practical application proposed by the company Calcul-Méca, a fiber reinforced composite sonar dome subjected to slamming. As a preliminary approach, a two-dimensional model with an approximated parabolic rigid body is developed. However, results obtained are not conclusive. Severe leakage occurs on the Lagrangian structure and could not be properly fixed. The slamming force seems to be incoherent with the expected physical behavior. These issues are probably associated to the low deadrise angle of the parabola combined with the high imposed constant velocity, which create extreme conditions for the penalty contact algorithm.

List of Figures

List of Tables

1. Introduction

1.1. Background

Slamming is a phenomenon that occurs when a structure impacts the water surface with high accelerations, creating severe impulsive loads with very short duration. It can occur in different situations in the marine environment. For instance, one of the most common cases is hull slamming, where a section of the hull, aft or forward, exits the water due to a wave crest and quickly reenters the surface.

Loads generated by slamming impact can be extremely dangerous, possibly resulting in structural damage or even collapse, as illustrated by the accidents with the passenger ferry *Estonia* in 1994 and the container ship *MSCNapoli* in 2007 (see Fig. 1), both catastrophically damaged by slamming loads. Additionally, the global dynamic response of marine structures subjected to slamming, called whipping, can lead to fatigue or high local stresses in some cases (Faltinsen, 2005 [46]).

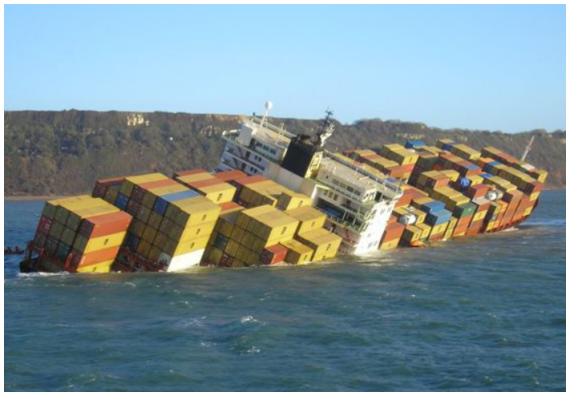

Figure 1: MSC Napoli stranded off the of coast of France after suffering catastrophic hull damage on the crossing of the English Channel (From: [62]).

Slamming is an issue not only in a safety perspective, but also economically, as operators frequently need to change speed and course in order to avoid the issue. It is known to be one of the major reasons for change of speed and course in shipping operations, having therefore an important influence on the margins of ship operators (Kapsenberg, 2011 [36]).

The topic of slamming has been under investigation since the beginning of the 20th century, and there is extensive literature on the subject. However, it is a highly complex phenomenon and reliable tools for the prediction of such impulsive loads and associated dynamic responses are still not available. Most existent analytical models are limited, relying on several simplified assumptions. Numerical methods are presented as an alternative, but are still very time consuming and require validation through experimental or analytical results. Moreover, experimental research on slamming is useful as a benchmark tool for validating other methods, however, it is unpractical in an industrial context. So, even

though a great amount of development has been done on the subject in the past decades, it is still insufficient to properly advise designers on the issue.

Another aspect that adds to the challenge, is the fact that ships have grown larger and more complex structurally, and advanced materials such as composites are becoming common on marine applications. All these factors reaffirm the need for practical and reliable tools capable of predicting slamming loads.

In this context, the project SUCCESS was created in France, through a cooperation between ICAM Engineering School, private companies, such as Calcul-Méca (design office) and Multiplast (composite vessel shipyard), and the French Navy. The main goal of the project is the study of the behavior of composite marine structures such as sonar domes, submarine acoustic windows or sailing ship hulls subjected to impulsive hydrodynamic loads, including slamming.

This Master Thesis was performed under the supervision of Professor Hervé Le Sourne (ICAM) and Jean Christophe Petiteau (Calcul-Méca) in the framework of the project SUCCESS and the academic final dissertation of the ERASMUS MUNDUS program EMSHIP (8th Cohort). During this project, the academic research was performed at ICAM Nantes campus and at the engineering design office of Calcul-Méca.

1.2. Objectives

The main objectives of this work are listed bellow:

- To understand the physical phenomena involved on slamming impact, identifying the most relevant factors that characterize this type of fluid-structure interaction.
- To develop a numerical model of slamming based on the Arbitrary Lagrangian Eulerian approach capable of reproducing the kinematics and kinetics of the phenomenon, providing an estimation of hydrodynamic loads and structural response of bodies subjected to water impact.
- To extend the model for Fiber Reinforced Composite structures, implementing available failure criteria on *LS-DYNA* to assess damage.

1.3. Literature Review

1.3.1. Theoretical Models of Slamming

The first analytical formulation on slamming was presented by Von Karman (1929) [79], who proposes an asymptotic solution based on momentum conservation to predict the loads to which the floaters of hydroplanes were subjected in water landing. The theory is based on the two-dimensional model of a wedge upon entry on calm water, assuming that

the movement of the free surface can be neglected. When applied to wedges with small deadrise angles, this idealization underestimates the impact loads.

Wagner (1932) [25] later modified the formulation, including a linear free-surface effect and taking into account the piled-up water on the wedge due to the elevation of the surface. He assumes that the wet portion of the body is approximated by a plate with an equivalent width. This development is effective for predictions of the overall pressure loads at initial stages of the entry. However, Wagner's pressure formula is singular at the edges of the idealized plate and results are only coherent if the deadrise angle of the wedge is lower than 20°. Besides, the air cushioning effect is not considered and the model is not applicable for angles smaller than 3°, when there is air trapped between the two surfaces (Okada and Sumi, 2000 [74]).

Several developments have followed these pioneering works. In particular, attempting to implement the non-linear behaviour of the fluid at the interface between the wedge and the free surface. For instance, Watanabe (1986) [30] and Zhao and Faltinsen (1993) [71] use the method of matched asymptotic expansion to combine Wagner's plate approximation with a nonlinear solution for the splash region. Cointe (1989) [66] and Howison et al. (1991) [18] propose a similar approach to the problem.

Models such as the one proposed by Logvinovich (1969) [81] were developed based on the idea of adding extra terms to the velocity potential distribution in order to correct Wagner's formulation. According to Logvinovich (1969) [81], these additional terms describe more precisely the flow in the periphery of the wetted region, where maximum pressures occur. However, the solution can only be applied to the two-dimensional vertical entry of a blunt and symmetric rigid body and the mathematical justifications of the model are still not consolidated, as stated in Korobkin (2004) [5].

Zhao et al. (1996) [72] present a semi-analytical formulation based on the generalized Wagner theory. By simplifying only the boundary conditions applied to the free-surface, the water jet height and penetration depth can be calculated using Wagner's assumption. These parameters are then used to solve the boundary-value problem at each time-step with the boundary element method. The evaluation of the free-surface profile is done by integrating numerically the distribution of velocity obtained, which provides the height of the water jet and penetration depth to be used in the next iteration. Due to the flow singularity present at the extremity of the wetted region, pressures estimated on these areas by nonlinear Bernoulli equation are negative. To overcome this issue, Zhao et al. (1996) [72] proposes the integration of the hydrostatic pressure only where values are positive. Results for the pressure distribution and hydrodynamic force obtained numerically with the presented method agree well with experimental drop tests.

Alternatively, Mei et al. (1999) [82] develops a fully analytical formulation based on the generalized Wagner theory by using the conformal mapping of the flow domain projected

onto a half-plane. The solution can only be found analytically for entry problems with known conformal mapping, such as a wedge or a cylinder. For general shapes, the solution must be performed numerically.

Scolan and Korobkin (2001) [54], extend Wagner's formulation to three-dimensional bodies with exact solutions. These solutions approximate the body to an equivalent flat elliptical disc analogous to Wagner's flat plate.

1.3.2. Experimental Models of Slamming

An extensive number of experimental slamming tests have been developed for the assessment of loading conditions and structural responses on plates, wedges and other more realistic model sections, such as bow flares.

Earlier works on drop-tests of two-dimensional wedges can be traced back to the 1950s with systematic experiments performed by Bisplinghoff and Doherty (1952) [39] to assess the impact force. In the 1960s and 1970s, further developments on rigid and elastic wedges have been done by Chuang (1966) [41], Chuang (1970) [40], where the relation between maximum pressure and deadrise angle is observed. Ochi and Motter (1973) [38] carried out several tests to derive the pressure-time distribution on a wedge.

Several relevant studies were developed in the 1990s. In particular, Kvalsvold and Faltinsen (1993) [34] observed the influence of the hydro-elasticity of a flat plate supported by stiffeners on the slamming loads, simulating the impact of a wave crest on the wet-deck of a multi-hull vessel. It was showed that the lower deformation modes govern the maximum strain. Zhao et al. (1996) [72] perform drop-tests with a 30° wedge and a bow flare section in order to validate the theoretical formulations developed on the study for the prediction of slamming loads. Three-dimenional flow effects in the experiments are theoretically estimated. Analytical results agree well with experimental values. Faltinsen et al. (1997) [49] performs similar tests with a flat plate, simulating wet-deck slamming. The hydro-elastic behaviour of the plate is assessed. It is concluded that for small deadrise angles the maximum pressures are very sensitive to external conditions and cannot be used as a measure of maximum local bending stresses.

More recently, Tveitnes et al. (2008) [78] carried out drop tests on wedges with imposed constant velocities. Various configurations of wedge geometries were analyzed for entry and exit cases. Huera-Huerta and Gharib (2011) [33] present a series of experiments focused on the characterization of the slamming loads on flat plates within the first phase of entry. The significance of the effect of air entrapment in decreasing loads is demonstrated. Tassin et al. (2011) [7] validate a simplified method for the analysis of hydrodynamic loads for the water entry of three-dimensional solids using a hydraulic impact machine. An elliptic paraboloid, a wedge with conical ends and a square pyramid are tested. The method

is found to be able to predict slamming forces with relatively good accuracy. Yettou et al. (2006) [20] and Tenzer et al. (2015) [56] further develop experimental literature by presenting extensive results on free-falling and constant velocity slamming wedges.

Experiments performed by Vincent et al. (2018) [43] and Panciroli et al. [70] present results on wedges, but with a special focus on the hydrodynamic phenomena involved in slamming. High speed cameras are used to observe the formation of the splash and cavitation zones.

1.3.3. Numerical Models of Slamming

More recently, increasing computing capability has enabled the use of numerical methods to simulate the slamming phenomenon. Three main aspects are usually observed: the prediction of slamming loads with rigid bodies, the effect of hydro-elasticity on the slamming response and the effect of air cushioning.

An extensive number of numerical models based on the experimental drop-test carried out by Zhao and Faltinsen (1996) [72] has been developed. Le Sourne et al. (2003) [23], for example, reproduces the wedge drop-test using the ALE formulation in the Explicit FEM code *LS-DYNA*. Two and three-dimensional models are compared in order to demonstrate the effects of three-dimensional flow on the extremities of the wedge. Stenius (2006) [26] and Luo et al. (2011) [24] apply a similar numerical approach to a 2D rigid wedge. The influence of parameters such as mesh density and contact stiffness on the convergence characteristics is observed. Stenius and Rosén (2007) [26] extends the model to an elastic wedge. Aquelet et al. (2006) [61] develops a model for a 2D rigid wedge in *LS-DYNA* to assess the capabilities of the penalty-contact algorithm.

Different numerical schemes, including Volume of Fluid (VOF) and Smoothed Particle Hydrodynamics (SPH) methods have also been used in the modeling of the water-entry problems; for example, on arbitrary bow sections (Ghadimi et al., 2013 [65]) and symmetric/asymmetric wedges (Farsi and Ghadimi, 2015 [50]), respectively. Kamath et al (2016) [4] uses a Reynolds-Averaged Navier-Stokes CFD (Computational Fluid Dynamics) solver to analyze a free-falling wedge on water impact. Hwang et al. (2015) [73] presents a fully Lagrangian coupled Fluid-Structure Interaction (FSI) solver based on the Moving Particle Semi-implicit (MPS) method to model the water entry of flexible wedges.

Examples of numerical slamming models for alternative geometries are found in Vepa et al. [76] and Tassin et al. (2012) [7]. The first studies a 2D composite cylinder impact with the SPH model. The second analyzes different three-dimensional bodies, such as an elliptical paraboloid, with the use of a numerical formulation developed with basis on Wagner's theory and the Boundary Elements Method (BEM). Yu et al. (2018) [84]

recreates experiments for the elastic horizontal plate from Faltinsen et al. (1997) [49] using ALE Explicit FEM.

More practical developments are found in Bae and Zakki (2011) [16] and Vezina and Firoozrai (2010) [57], where ALE Explcit FEM is used for the drop test of a lifeboat and a speedboat respectively.

1.4. Structure of the Report

This report is divided as following:

- **Chapter 2**: A theoretical background on slamming is presented.
- **Chapter 3**: The theoretical basis for the explicit finite element model developed in this work is presented.
- **Chapter 4**: A theoretical review on fundamental concepts for Fiber Reinforced Composites and the methodology for implementing such materials in *LS-DYNA* is presented.
- **Chapter 5**: A two-dimensional model of a rigid wedge upon water-entry is developed. Results for the numerical simulation are compared against experimental drop-tests in order to validate the model. A study on the sensitivity of the main governing parameters of the contact algorithm is performed.
- **Chapter 6**: A three-dimensional model of a rigid wedge upon water-entry is developed in order to provide an overview on the limitation of the 2D case.
- **Chapter 7**: The slamming model is applied to an elastic flat plate. Localized pressure and deflections are compared with experimental results.
- **Chapter 8**: The slamming of a fiber reinforced composite sonar dome is proposed. No conclusive results are obtained.
- **Chapter 9**: The conclusion of the work and possible further developments are presented.

2. Slamming

2.1. Slamming Theory

Slamming is a highly non-linear multi-physical phenomenon that occurs when a structure impacts a fluid at a small relative angle between the two surfaces, resulting in a sudden acceleration of the fluid in the contact interface. Typically, the slamming force has a duration of milliseconds, generating high localized pressure peaks with short duration. This type of fluid-structure interaction (FSI) is similar to an explosion in terms of load profiles and can lead to severe structural damage even at low impact speeds (Kapsenberg, 2011 [36]).

The phenomenon is an issue specially for ships sailing in rough seas, when steep waves force the forward part of the vessel to emerge and reenter the water with high acceleration, subjecting the bow to extreme impact loads (see Fig. 2). In the case of aft-body slamming, appendages such as azimuth propellers and rudders can be particularly vulnerable (Kapsenberg et al., 2006 [37]).

Figure 2: Slamming on the frigate De Grasse (From: Tassin, 2011 [6]).

Figure 3: Damage caused by wet-deck slamming in the high-speed catamaran HSS 1500 Stena (From: Lavroff et al., 2010 [35]).

Critical slamming loads, possibly resulting in damage and loss of structural integrity, can also be observed in situations such as the breaking of waves in the wet-deck of high-speed catamarans (see Fig. 3) and columns of semi-submersible platforms.

Slamming is a relevant matter concerning marine safety and there is a great interest in developing formulations for predicting slamming loads. The problem is commonly idealized as a two-dimensional wedge, representing the section of a ship's hull that impacts a calm water surface, as shown in Fig. 4.

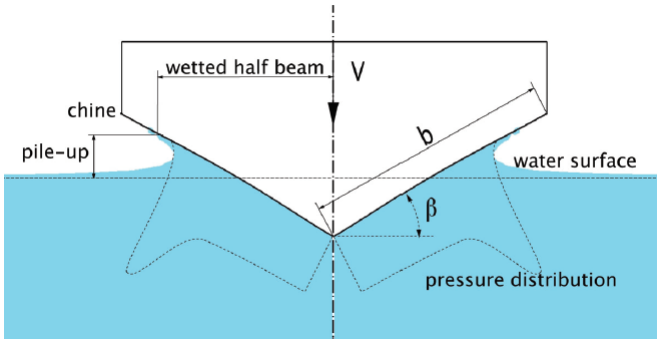

Figure 4: Schematic diagram of an idealized hull subjected to slamming. The free-surface development and the pressure distribution are depicted (From: Stenius and Rosén, 2007 [27]).

The typical free-surface development and the characteristic pressure distribution can be observed. As the wedge enters the surface, the fluid accumulates at the intersection between body and fluid, creating a pile-up region. This accumulated volume later generates a water jet that is launched away from the wedge. Two main stages are distinguished: a dry-chine and a wet-chine stage. The first is characterized by a highly localized pressure peak that occurs in the pile-up region, followed by a lower and fairly constant pressure distribution in the submerged portion of the wedge (see Fig. 4). In the second stage, the wedge is completely bellow the initial free-surface and the pressure is approximately uniform (Stenius and Rosén, 2007 [27]).

According to Faltinsen (2000) [47], slamming is mainly governed by two parameters: the impact velocity V and the impact angle β. Slamming loads are directly proportional to the velocity of the impact, while inversely proportional to the angle of incidence. This relation has been demonstrated in several experimental studies.

However, for angles below 5°, the phenomenon becomes more complex due to the occurrence of the air cushioning effect. Air entrapment (termed as ventilation) combined with a cavitation process, creates an air pocket between the structure and the fluid surface. As a result of the high compressibility of this air volume, slamming pressures are decreased. This phenomenon is difficult to reproduce accurately and in a controlled manner in scaled experiments (Faltinsen, 2017 [48]), which affects the reliability of slamming experiments in small deadrise angles.

Furthermore, the hydro-elasticity of the structure has also an effect on the slamming loads. This is further explained in Sec. 2.2. It is important to note that for bodies undergoing severe deformations, even for higher deadrise angles, cavitation might originate, as demonstrated by Panciroli et al. (2018) [70].

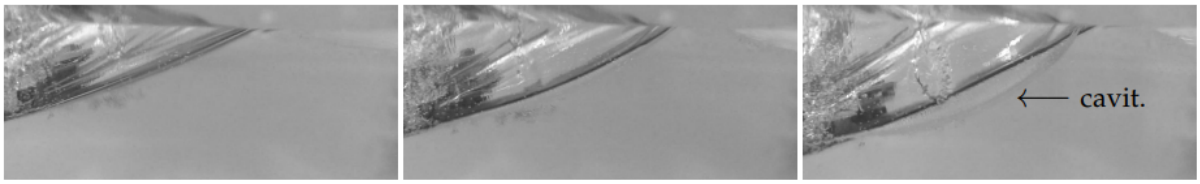

Figure 5: Experiment performed by Panciroli et al. (2018) [70]) on the water entry of an elastic wedge. The development of an air-pocket created by cavitation is observed as the wedge progresses into the water ($\beta = 20°$).

Several analytical methods have been developed to predict slamming loads. For instance, the classical model developed by Wagner (1932) [25] estimates the hydrodynamic pressure in the fluid with the use of the unsteady Bernoulli equation described by (Vincent et al., 2018 [43]):

$$p = -\rho \left(\frac{\partial \phi}{\partial t} - \frac{1}{2} |\vec{\nabla} \phi|^2 \right) \tag{1}$$

The velocity potential of the fluid acting on the wedge is given by:

$$\phi = -V(t) \sqrt{c(t)^2 - x^2} \tag{2}$$

Where $V(t)$ is the entry velocity and the wet portion of the body is approximated by a horizontal plate with an equivalent width $c(t)$ (see Figure 6).

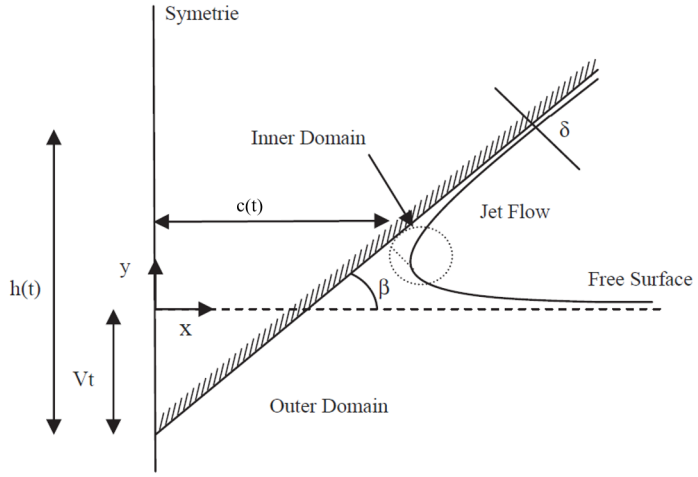

Figure 6: Wagner's wedge slamming formulation (Peseux et al., 2005 [10]).

The parameter $c(t)$ is actually the location point where the water jet initiates and is given by Wagner's condition:

$$c(t) = \frac{\pi V t}{2tan\beta} \tag{3}$$

Zhao and Faltinsen (1993) [71] propose a solution for small deadrise angles developed with the asymptotic method. It is assumed that the flow is divided into an inner and outer flow domains. This composite formulation allows the inclusion of the effects of the water jet that occurs on the inner flow region (see Fig. 6). The pressure distribution is described as:

$$p = \rho V c \frac{dc}{dt}(c^2 - x^2)^{-\frac{1}{2}} - \rho V c \frac{dc}{dt}[2c(c-x)]^{-\frac{1}{2}} + 2\rho \left(\frac{dc}{dt}\right)^2 |\tau|^{\frac{1}{2}}(1 + |\tau|^{\frac{1}{2}})^{-2} \tag{4}$$

The parameter τ relates the wetted surface length and the thickness of water jet. The maximum slamming pressure on the wedge is given by Eq. 5.

$$p_{max} = \frac{1}{2}\rho V^2 \left(\frac{\pi}{4}\right) \cot \alpha^2 \tag{5}$$

Alternatively, Faltinsen (1993) [63] proposes the solution of Eq. 1 as a simplified boundary value problem. Since the rate of change of ϕ with time is larger than the rate of change of ϕ with respect to position, the term $\vec{\nabla}\phi$ is neglected. The obtained pressure distribution is:

$$p = \rho V \frac{c}{\sqrt{c^2 - x^2}} \frac{dc}{dt} + \rho \frac{\partial V}{\partial t} \sqrt{c^2 - x^2} \tag{6}$$

Equation 6 is composed by two terms: the added mass pressure and the slamming pressure. The first term is related to the rate of change of momentum of the added mass, while the second describes the dynamic pressure contribution.

It is important to note that $c(t)$ is not differentiable when the contact angle between surface (α) and impacting body is zero. The slamming pressure goes to infinity as the angle approaches zero, which is obviously not physical. Therefore, for an analytical solution of a flat plate, the angle of impact considered must be larger than 0°, assuming for example an initial imperfection of the plate.

A maximum pressure along the surface occurs in the middle of the plate. It can be estimated with the formula presented in Eq. 7.

$$p_{max} = \frac{1}{2}\rho V^2 \pi \cot \alpha \tag{7}$$

Many other formulations have been developed for the slamming case, mostly based on Wagner's classical approach. However, the scope of this study is kept on the formulations

by Zhao and Faltinsen (1993) [71] and Faltinsen (1993) [63], which were validated with experimental results used in comparison with numerical models here developed.

2.2. Hydro-elastic Structural Response

Hydro-elastic slamming impacts occur when hydrodynamic loads cause the structure to undergo elastic deformations, which simultaneously affects the fluid flow, decreasing the resulting pressure field. This coupled interaction is generally significant for local impacts at small relative surface-structure angles, if the resonance period of the structure is larger than the impact duration (Kapsenberg, 2011 [36]). Typically the case for plates with deadrise angles smaller than 5°, associated to highly concentrated short duration peak pressures. For larger deadrise angles, such as in bow-flares, the hydro-elastic influence can generally be neglected. Results from Faltinsen (1999) [47] on the experimental investigation of water impact of elastic wedge sections demonstrates this relation.

According to Bereznistki (2001) [1], the ratio between the impact duration and the first natural dry period (natural period of the structure on air) is also a key factor to define whether hydro-elasticity effects are negligible or not. A numerical investigation on this aspect is performed with a model of slamming for beams with different stiffness values and deadrise angles. Responses are compared in terms of maximum deflections (see Fig. 7).

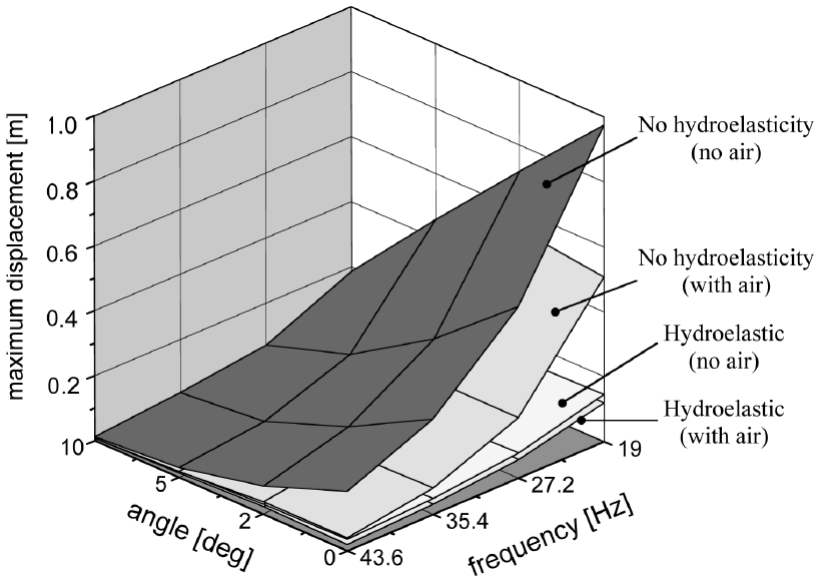

Figure 7: Results from the numerical model proposed by Bereznistki (2001) [1] to analyze the role of hydro-elasticity on slamming. The maximum deflection increases as incidence angle and natural frequency are decreased.

As the natural period increases (natural frequency decreases) the maximum deflection increases. Additionally, it can be observed that the air entrapment has an influence on the

response, further decreasing the slamming loads (as explained in Sec. 2.1) and resultant deformations.

2.3. Experimental Slamming

Hull-water impact problems have been assessed experimentally in a number of studies. Zhao and Faltinsen (1993) [71] and Faltinsen (1997) [49], in particular, carried out tests in the facilities of MARINTEK, in Norway, to validate the theoretical methods developed in their works.

A typical drop-test rig used in slamming experiments consists basically of a vertical guide rail, a trolley and an attachment for the test section and ballast, as shown in Fig. 8. The test section is driven to a calm water surface bellow the drop rig either on free-fall or with the use of an impulsion mechanism, usually hydraulic. Velocity and impact angle can be adjusted.

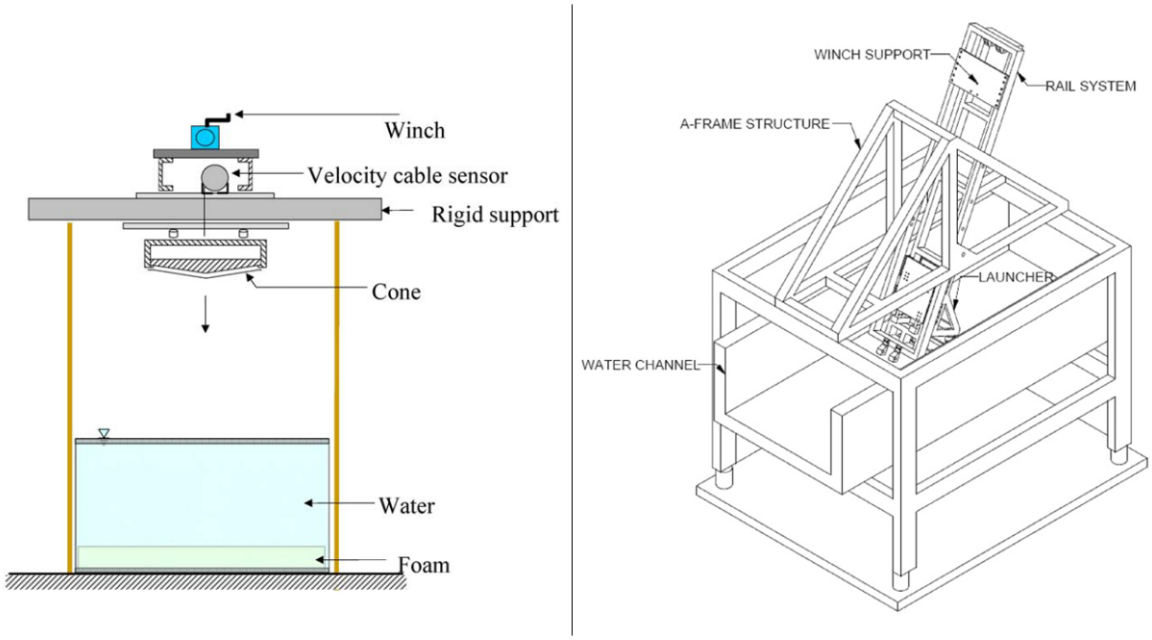

Figure 8: Free-fall drop rigs used in the experiments by Donguy et al. (2001a) [8] (left) and Huera-Huarte et al. (2011) [33] (right).

Generally, these tests are focused on the measurement of pressure or hydrodynamic force time-histories (see Fig. 9) and structural responses of the impacting bodies in terms of deflections and stresses. Force and displacement transducers, pressure and strain gauges and accelerometers are used for these applications. High speed cameras can be applied in the analysis of the free-surface behavior and hydrodynamic phenomena such as cavitation (see Fig. 5).

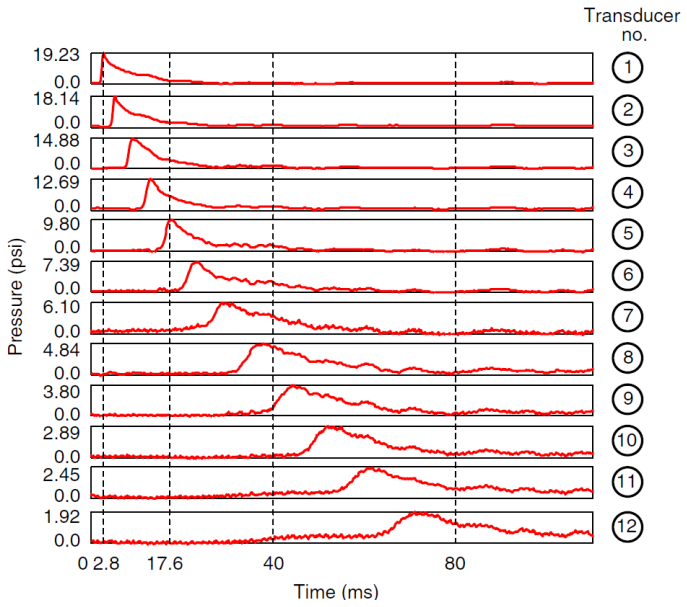

Figure 9: Pressure time-history on a free-falling wedge ($\beta = 25°; m = 94kg$) obtained by Yettou et al. (2006) [20]. Pressure transducers are placed sequentially from keel to chine (1 to 12). A pronounced impulsive peak pressure at the first instants of the impact gradually lowers and becomes relatively smooth as the wedge progresses into the water.

A slamming experiment is complex; the duration of impact loads is very short and sensors with high sampling rates, in the order of 5-10kHz, are required from the (Kapsenberg, 2011 [36]). Additionally, the concentrated peak pressures are very sensitive to small differences in physical conditions and, therefore, the repeatability of the experiments is compromised. It is reported by Faltinsen (2005) [46], that for small deadrise angles ($< 5°$), the experimental measurement of maximum pressures becomes considerably inaccurate. The results of maximum pressures for different velocities were very dispersed, as shown in Fig. 10.

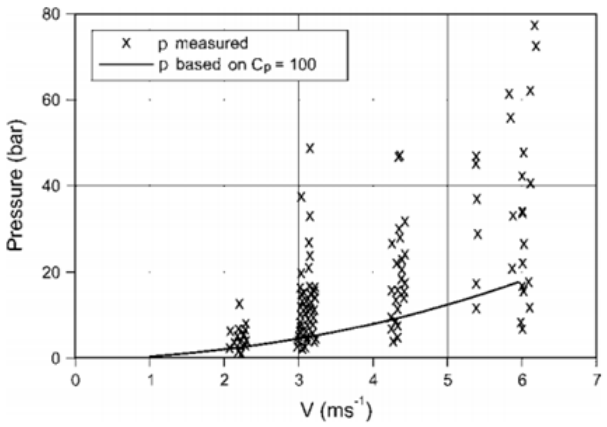

Figure 10: Experimental results obtained in the drop-test. (From: Faltinsen, 2005 [46]). Maximum pressures measured at each velocity are highly dispersed.

Furthermore, the effect of air cushioning, which also has a significant influence on the results, is difficult to exactly reproduce at each test.

According to Faltinsen (2005) [46], from a point of view of structural response, the pressure peaks are not relevant and the estimation of impulse, represented by the integral of the pressure-time curve, is more reliable.

3. Finite Element Analysis: Application to Slamming Impact

Slamming impacts are phenomena that occur in short duration periods and involve highly non-linear fluid-structure interactions (FSI) and material deformations. The use of robust numerical models capable of dealing with these characteristics is crucial in the development of accurate simulations of such events.

In this study, slamming models are developed with the explicit non-linear finite element (FE) code *LS-DYNA* using the Arbitrary Lagrangian-Eulerian (ALE) formulation in combination with the penalty contact algorithm, suitable for impact problems.

3.1. Explicit Finite Element Analysis

In a vast number of engineering problems, loads are applied at slow rates and acceleration effects can be neglected. This class of problems can be described by quasi-static FE models that are time-independent and generally rely on implicit solution schemes of the governing motion equations. A simple cantilever beam with a distributed load is an example of a quasi-static process. However, dynamic events such as slamming, are time-dependent problems, where bodies are subjected to high accelerations that must be taken into account. Explicit solutions are more suitable for these cases. The two approaches are explained in this section, with focus on the explicit method used in this study.

In the case of a dynamic analysis, the governing equation of motion is:

$$[M]\{x''\} + [C]\{x'\} + [K]\{x\} = \{F\} \tag{8}$$

where M is the mass matrix of the system, C is the damping matrix, K is the stiffness matrix or in a more general case, for large displacements/deformations, K can be a function of the displacement, and F is the external force. The three unknown variables x, x' and x'' are, respectively, the displacement, velocity and acceleration of the system, which are obtained with the use of one the numerical approaches aforementioned.

For instance, an explicit solution is a time-dependent scheme, on which the state of the system in the current time-step is calculated with respect to the state achieved in the previous step. In practice, that means that at time-step n, the governing equation (Eq. 8) is solved for the acceleration x'' through inversion of the mass matrix M. Usually, the mass is defined as a lumped body, represented by a diagonal matrix which is relatively simple and straightforward to invert. Once the acceleration is calculated at time-step n, velocity and displacement for increment $(n + 1)$ can be obtained.

The explicit solution is generally less costly in terms of computation time, since the inversion of the mass matrix is less complex. However, it is not based an iterative integration scheme, and therefore, it is not unconditionally stable. In other words, the algorithm requires very small time-steps in order to be stable. According to Courant–Friedrichs–Lewy (CFL) stability condition, the time-step must be small enough so that no information is able to propagate through more than one element at each step (this will be further explained).

Alternatively, in an implicit solution, the displacement is not a function of time, so x is constant, $x" = 0$ and $x' = 0$, which cancels out the mass and damping terms in Eq. 8 and yields:

$$[K]\{x\} = \{F\} \tag{9}$$

The equilibrium of internal and external forces described by Eq. 9 is solved for x at each time-increment. In this case, the solution requires the inversion of the stiffness matrix, which is a highly expensive iterative process (Euler integration scheme). Differently from the explicit method, an implicit solution is unconditionally stable and larger time-steps can be used. This method is suitable for static analyses, where larger time-steps can be applied, decreasing computation time without loss in numerical stability.

In summary, explicit analyses rely on several small time-steps to keep numerical stability and reach convergence, while implicit analyses can be performed with a smaller number of larger time-steps. For dynamic problems with large deformations, which take place in a time frame of milliseconds and require great numbers of degrees of freedom, explicit solutions are more practical, being capable of handling the large mass matrices more efficiently.

Regarding the numerical stability of explicit solutions, it is explained in the *LS-DYNA* Theory Manual [15] that the time-step size should be smaller than the propagation time of an acoustic wave through an element using the shortest characteristic distance, defined as the critical time-step $\Delta t_{critical}$. This ensures the fulfillment of the CFL stability condition and guarantees coherence between numerical and physical domains (Laney, 1998 [9]). Effectively, a critical time-step size is given by:

$$\Delta t_{critical} = \alpha \left(\frac{l_e}{c_e} \right) \tag{10}$$

Where l_e is the characteristic length of the element, c_e is the wave propagation speed for a specific material and α is a safety factor. In *LS-DYNA*, the time-step is defined automatically, by searching the smallest time-step among all elements in the previous increment. A scale factor (*TSSFAC*) from the card CONTROL_TIMESTEP can be used to calibrate the parameter.

3.2. Fluid-structure Interaction Formulations

Different numerical formulations such as pure Lagrangian, Eulerian, Arbitrary Lagrangian-Eulerian (ALE) and Smoothed Particle Hydrodynamics (SPH) can be applied in the modeling of FSI problems. Each of these methods has particular advantages and drawbacks depending on the application context. In this section, these methods are briefly presented and compared. The ALE method used during the present master thesis work in the modeling of slamming impact is explained in detail.

3.2.1. Lagrangian Formulation

In a pure Lagrangian formulation, the finite element mesh follows exactly the material displacement. The nodes of the mesh are attached to the material and both translate, rotate and deform together. The sequence shown in Fig. 11 illustrates the high speed impact of a soft body upon a rigid fixed plate, where the moving impactor is described by a Lagrangian mesh.

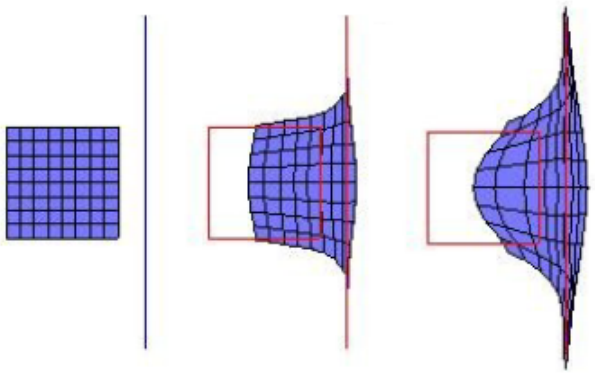

Figure 11: Sequence of impact of a soft body impact upon a fixed plate. Both parts are described by Lagrangian meshes, but the impactor is in motion while the plate is fixed (From: Day, 2010 [32]).

Material flow between adjacent elements is not allowed in the Lagrangian formulation and material boundaries can be automatically and easily tracked. As a result of this, lower computation time is required relative to other formulations. This method is usually applied to problems where small deformations and smooth flows are expected, being accurate and computationally efficient in these particular cases. However, in applications where large material deformations are present, severe mesh distortions can occur, leading to low accuracy, negative volume elements or excessively small time-steps.

3.2.2. Eulerian Formulation

A pure Eulerian formulation, on the contrary, relies on a mesh fixed in space and materials are allowed to move and deform within this fixed computational grid. In the sequence shown

in Fig. 12 the soft body advects, that is, travels through the Eulerian mesh, which remains static. Small amounts of material flow from element to element at each time-step. In a multi-material model, different materials can be contained in an element simultaneously, e.g., water and air in slamming problems.

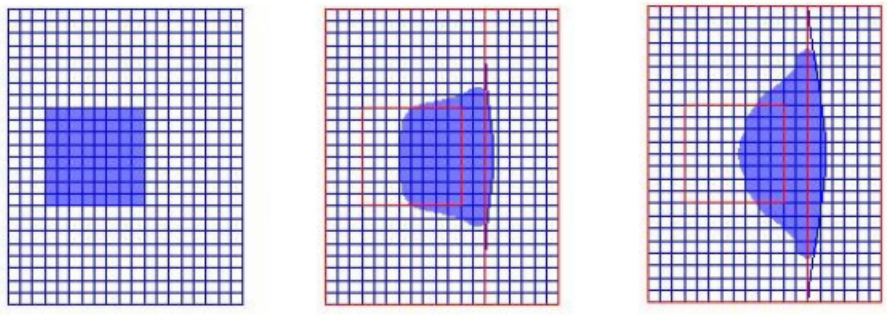

Figure 12: The soft body moves through the Eulerian mesh, which remains fixed in space (From: Day, 2010 [32]).

The Eulerian formulation is more suitable for cases where large deformations occur. A fixed mesh combined with a strong advection algorithm helps minimize the issue of mesh distortion encountered in the Lagrangian method (see Fig. 13). However, the computational cost is relatively higher due to the advection process required at each time-step. Another disadvantage of this particular formulation lies on the fact that the whole spatial domain covered throughout the simulation needs to be meshed, which reflects in computation cost.

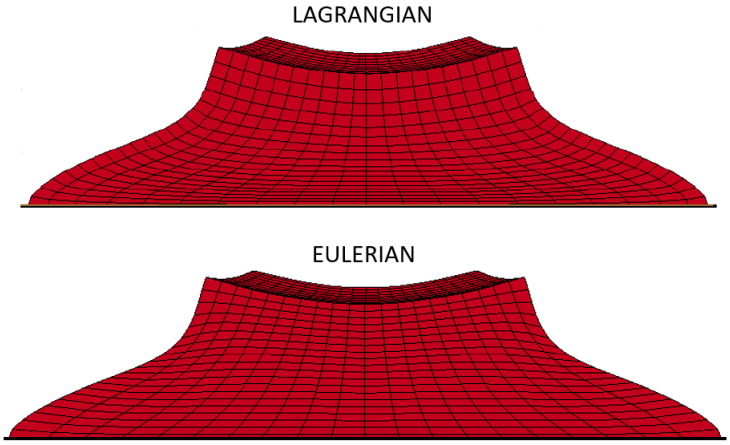

Figure 13: Comparison of the two methods when applied to large deformation. It is possible to observe highly distorted elements in the center region of the upper Lagrangian mesh (From: Olovsson, 2003 [42]).

3.2.3. Arbitrary Lagrangian Eulerian Formulation

A third approach to FSI models, called Arbitrary Lagrangian Eulerian (ALE), consists in combining characteristics of both Eulerian and Lagrangian methods. In Fig. 14, the same impact scenario is presented with an ALE model. The fixed plate is composed of

Lagrangian elements, while the impactor is defined by an Eulerian mesh. However, in this case, the Eulerian grid is allowed to move along with the material, unlike the fully Eulerian method where it remains fixed. A third moving mesh is placed on the background of the fluid domain. This mesh describes an arbitrary motion that allows for a smooth advection of the material, while decreasing computational cost, as it eliminates the need for coverage of the entire spatial domain.

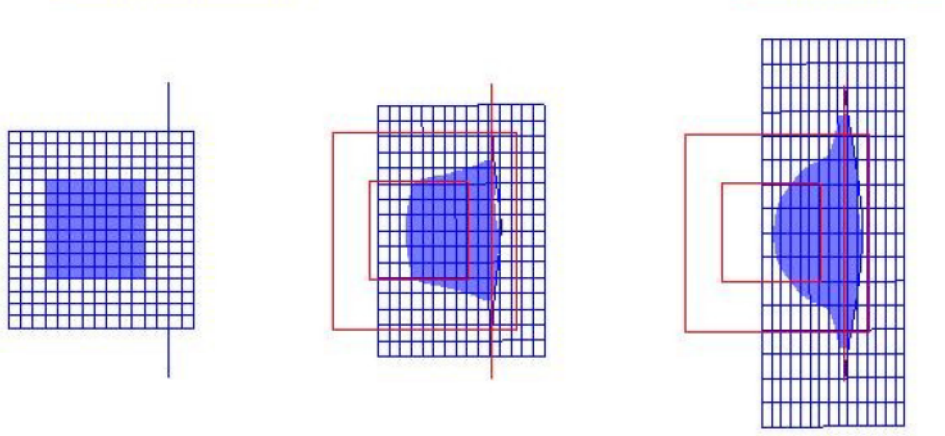

Figure 14: A soft body impact described with an ALE model. The Eulerian mesh moves along with the body. An arbitrary background mesh is used to enable a smooth advection process (From: Day, 2010 [32]).

It is noted that the Eulerian formulation is in fact a special case of ALE, where the velocity of the arbitrary mesh is zero, so it remains fixed in the spatial domain. For slamming models, the Eulerian particular case is generally used, as fluid domains are fixed in relation to the impacting Lagrangian body and an adaptive mesh is not necessarily required (see Fig. 15). Furthermore, a fully Eulerian approach eliminates the problem of mesh distortion.

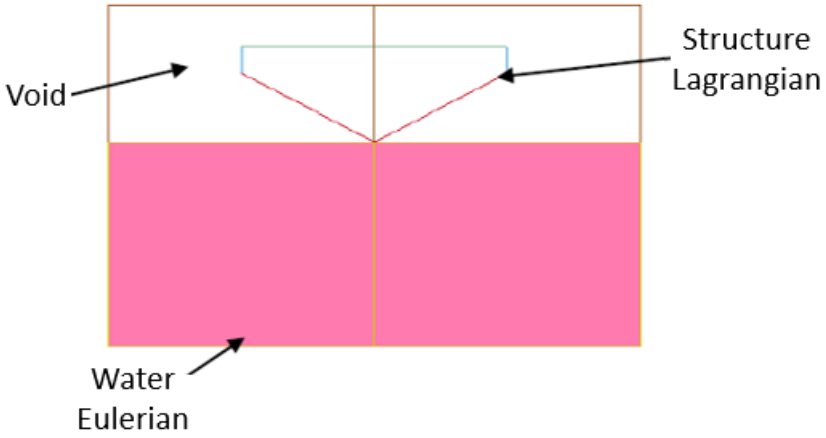

Figure 15: Wedge slamming model in ALE. The water is described by a fixed Eulerian mesh and the wedge is defined as a Lagrangian structure (From: Aquelet and Souli, 2012 [59]).

The ALE formulation is based on conservation laws described by the following governing equations (Aquelet et al., 2006 [61]):

- Conservation of Mass

$$\frac{\partial \rho}{\partial t} + \rho \nabla . \vec{v} + (\vec{v} - \vec{w}) \nabla \rho = 0 \tag{11}$$

- Conservation of Momentum

$$\rho \frac{\partial \vec{v}}{\partial t} + \rho(\vec{v} - \vec{w}) \overline{\overline{\nabla}} \vec{v} = (\vec{\nabla} . \overline{\overline{\sigma}} + \vec{f}) \tag{12}$$

  The stress tensor $\overline{\overline{\sigma}}$ is given by:

$$\overline{\overline{\sigma}} = -p \overline{\overline{\delta}} + \mu(\overline{\overline{\nabla}} \vec{v} + \overline{\overline{\nabla}} \vec{v}^{\,T}) \tag{13}$$

- Conservation of Energy

$$\rho \frac{\partial E}{\partial t} + \rho(\vec{v} - \vec{w}) \vec{\nabla} E = \overline{\overline{\sigma}} : \overline{\overline{\nabla}} \vec{v} + \vec{f} . \vec{v} \tag{14}$$

Material density is denoted by ρ, p is the pressure, δ is the material deformation and μ is the dynamic viscosity of the fluid. The external force is represented by f and the internal energy is E. The term $(v - w)$ describes the relative velocity between fluid and ALE mesh, where v is the material velocity and w is the mesh velocity. In the Eulerian formulation, the mesh is fixed, and therefore, $w = 0$.

In a single material model, the fully-coupled equations can be directly solved. On the other hand, for a more complex multi-material ALE, a split operator is required. This operator divides the calculations into two phases, Lagrangian and advection, uncoupling Lagrangian and Eulerian domains at each time-step. Governing equations remain the same as in a single material model, but in this case, calculations are performed iteratively for each material group in the element.

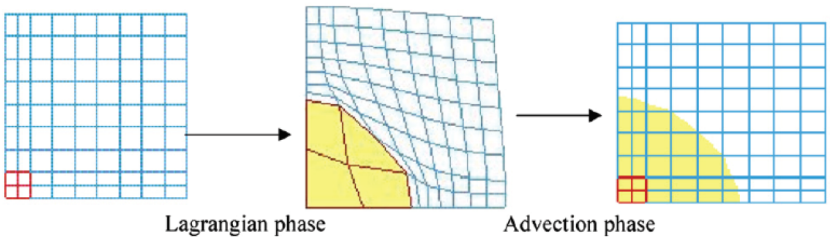

Figure 16: Lagrangian and advection phases used in a split operator algorithm for multi-material ALE. The model describes an explosion (From: Messahel and Souli, 2013 [69]).

No material flow occurs across element boundaries in the Lagrangian phase, and so, mass is automatically conserved. In the advection phase; mass, energy and momentum transport between elements is computed. This process may be understood as a reconstruction of the displaced mesh in the Lagrangian phase. Smoothing algorithms are used to redefine the mesh back to the original Eulerian or ALE configuration, as shown in Figure 16 (Messahel and Souli, 2013 [69]).

A typical multi-material ALE algorithm time-step is summarized as following (*LS-DYNA* Theory Manual [15]):

- Lagrangian Phase: The equations of motion for the Lagrangian domain are solved and the velocity fields are updated;
- Advection Phase: An advection algorithm with the typical following steps is performed:
  - Identification of the nodes which will be moved;
  - Boundaries nodes are moved;
  - Interior nodes are moved;
  - Transport of the element-centered variables is calculated;
  - Momentum transport is calculated and velocity is updated.

Smoothing algorithms remap the mesh in the first two stages of the advection phase. In some particular approaches, the arbitrary computational grid conforms closely with the external boundaries of the material. However, in more general and robust algorithms the mesh usually does not match exactly (Day, 2010 [32]).

According to *LS-DYNA* Theory Manual [15], the advection step has a significant influence both in the total calculation time and in the accuracy of the model, generally representing from two to five times the cost of the Lagrangian time-step. This high computational cost is mostly associated to the transport calculation of the element-centered variables (i.e., density, internal energy, the stress tensor and history variables).

An efficient algorithm must be capable of properly rezoning the arbitrary mesh, performing as few advection time-steps as possible, whilst avoiding distortion. In *LS-DYNA*, the element advection will only be performed if more than 20% of its volume is transported, that is, when the gain in time-step size is greater than the advection calculation cost. Advection algorithms such as first-order advection or Van Leer scheme are commonly used.

In *LS-DYNA*, the card CONTROL_ALE is used to configure the ALE model. The parameter *METH* is used to define the advection method used in the algorithm. In this case, the donor cell with Half Index Shift (HIS), first order accurate algorithm, *LS-DYNA's* is selected.

3.2.4. Smoothed Particle Hydrodynamics Formulation

The Smoothed Particle Hydrodynamics formulation (SPH), first developed for application in the field of astrophysics, was later extended to high velocity impact in solid mechanics, Navier-Stokes governed CFD, fluid-structure interaction problems and other applications. It is a mesh-free discretization scheme based on the Lagrangian formulation, where materials are represented by sets of particles that interact with each other (see Fig. 17). Each particle has its own mass and carries hydrodynamic and thermodynamic properties of the fluid at that discrete point in the continuum (Guida, 2008 [52]).

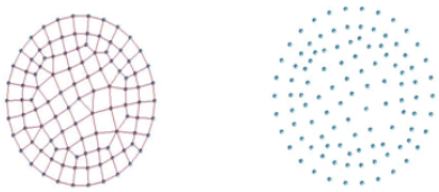

Figure 17: Comparison of FEM (left) and SPH (right) meshes (From: Messahel and Souli, 2013 [69]).

SPH particles are, in fact, interpolation points where functions that define the instantaneous material behaviour and their derivatives can be estimated. Connectivity between particles is defined by a smoothing kernel function (Smith and Stojko, 2004 [14]).

This method is interesting in the modeling of high velocity impact (see Fig. 18); since, due to its grid-free nature, it is relatively efficient to reproduce large deformations without the issue of severe mesh distortion or element tangling associated to the Lagrangian formulation (or ALE to a lesser extent). In general, SPH is well suited for impact problems. Nonetheless, the method demands high computational cost and is prone to numerical instabilities in some cases. In this study, the focus is kept on the ALE formulation, which has been extensively applied to slamming and is well proven.

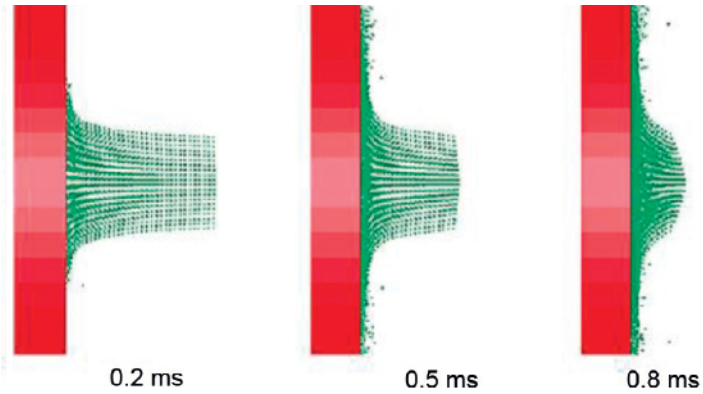

Figure 18: SPH impact model of a bird-strike. The impactor that represents the bird is described by particles (From: Hedayati and Ziaei-Rad, 2013a [68]).

3.3. Fluid-Structure Coupling: Penalty Contact Algorithm

One of the most important aspects of a dynamic fluid-structure interaction problem is how to couple solid and fluid domains and properly track the transient contact interfaces. The way structure and fluid interact is closely related to the accuracy of results.

This task is performed by specific coupling algorithms, such as the kinematic or the penalty contact methods, which are the most common approaches. These algorithms designate master and slave roles for the stationary and moving parts, respectively, in the case of FSI problems (Aquelet et al., 2006 [61]). According to *LS-DYNA* Keyword User's Manual [44], the penalty contact algorithm is, in general, more accurate and should be preferred.

The first approach, the kinematic method, constrains master and slave nodes to the same velocity. Total momentum is conserved, but not total energy. In the second approach, the penalty contact, the Lagrangian and Eulerian meshes are allowed to interpenetrate at a first stage and a resisting force proportional to the penetration depth is then applied between the interacting nodes (Souli and Benson, 2013 [55]). This force acts in opposite directions on the slave and master nodes in order to satisfy equilibrium.

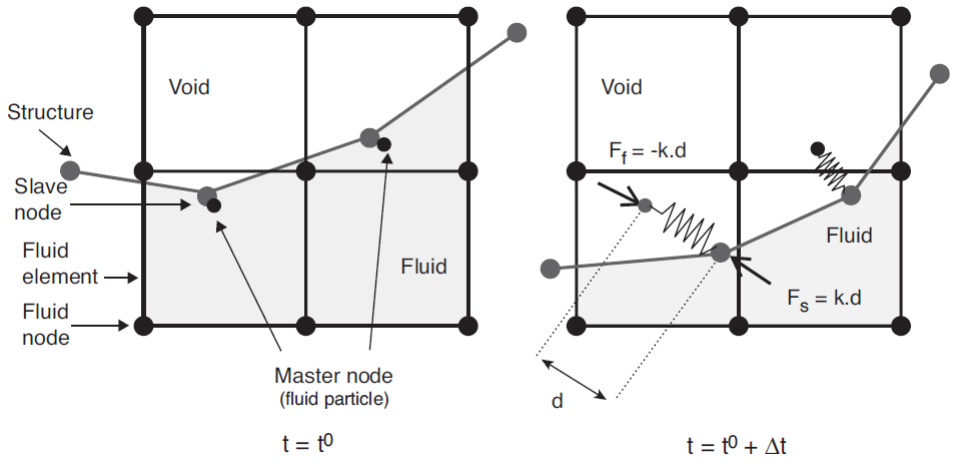

Figure 19: Description of the penalty contact algorithm applied to an ALE model. The Lagrangian mesh penetrates the surface of the Eulerian fluid in the first stage, which is subsequently restored by an applied resisting force (From: Souli and Benson, 2013 [55]).

In practice, a penalty coupling behaves like a virtual spring attached between the master and slave nodes, as shown in Fig. 19. The coupling force is described by:

$$F = k.d \tag{15}$$

Where k is the stiffness of the spring and d is the penetration. This resisting force acts directly on the nodes of the structures, whereas for the fluid elements, it is distributed among the nodes with the use of shape functions. The parameter k is defined as:

$$k = p_f \frac{KA^2}{V} \tag{16}$$

With K, V and A representing, respectively, the bulk modulus of the fluid, the volume of the fluid element and the average area of the Lagrangian elements connected to the slave node involved in the coupling. The scalar factor p_f, $0 \leqslant p_f \leqslant 1$, is introduced to enable the calibration of the k, since the contact stiffness is problem dependent (Aquelet et al., 2006 [61]).

In fact, one of the main concerns when implementing this technique lies on how to define properly the stiffness of the coupling. As the stiffness is increased, the interpenetration of structure and fluid is decreased until a perfect interface condition, when $d = 0$, is reached. However, numerical instabilities may arise from an excessively stiff contact, affecting convergence stability and generating noise on the results (see Fig. 20). This is mainly due to two factors: the high eigenfrequency associated to stiff elastic systems and a phenomenon called release, on which slave and master nodes couple and separate in the same time-step (From: Souli and Benson, 2013 [55]). The latter, can be avoided by bounding the contact force by a contact force between two spheres. This method, called pinball algorithm, is explained in detail in Belytschko and Neal (1991) [77]. The first factor, however, is more complicated and will be further discussed.

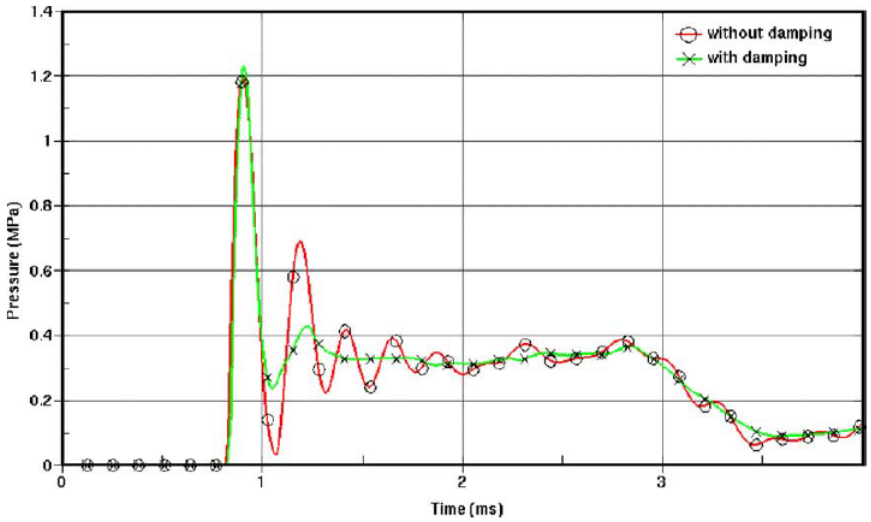

Figure 20: Pressure time history obtained for a slamming model. Red curve: without damping, green curve: with damping (From: Aquelet et al., 2006 [61]).

On the other hand, if the penalty contact is not high enough, large non-physical penetrations occur, leading to disturbances on the flow filed and leakage on the Lagrangian structure (Stenius and Rosén, 2007 [27]). This is specially problematic in high velocity impacts.

As mentioned previously, an important issue inherent to the penalty contact algorithm is the numerical noise caused by high frequency oscillations generated in the coupling. In

order to mitigate such problem, a viscous contact damping is added to the system (see Fig. 21).

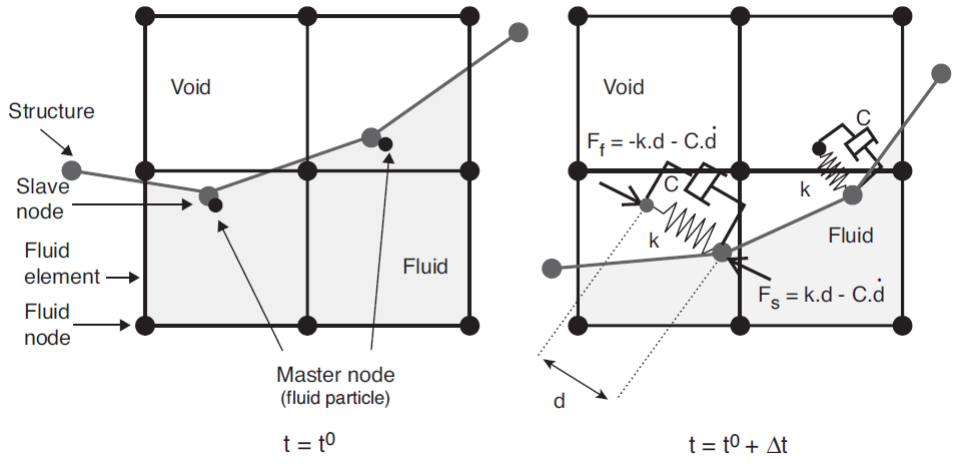

Figure 21: Penalty contact algorithm with added viscous damping (From: Souli and Benson, 2013 [55]).

With the addition of the damping term, Eq. 15 becomes:

$$F = k.d + C.\dot{d} \tag{17}$$

where the damping coefficient C is described by:

$$C = \xi\sqrt{k.M} \tag{18}$$

M is the equivalent mass. The damping factor ξ is analogous to the penalty factor and is used to scale the applied damping. According to Souli and Benson (2013) [55], when ξ is critical, damping is optimal. For $\xi = 2$, numerical oscillations are completely damped out. It is important to observe, however, that this approach, might affect physical characteristics of the model if not correctly set. This occurs when numerical stiffness k is close to physical stiffness, which is generally not the case.

In conclusion, the definition of the contact algorithm is a complex task that requires an intensive process of trial and error. A previous notion of the overall behaviour of the fluid and the structure combined with preliminary estimations of the maximum loads are, therefore, essential in this process.

In *LS-DYNA*, the contact algorithm is defined through the card CONSTRAINED_LAG RANGE_IN_SOLID, shown in Fig. 22.

```
*CONSTRAINED_LAGRANGE_IN_SOLID
$#    slave    master     sstyp     mstyp     nquad     ctype     direc     mcoup
         1         2         2         0         0         4         1         1
$#    start       end      pfac      fric    frcmin      norm   normtyp      damp
       0.0       0.0       0.5       0.0       0.0         0         0       0.9
$#       cq      hmin      hmax     ileak     pleak   lcidpor     nvent  blockage
       0.0       0.0       0.0         0       0.0         0         0         0
$#   iboxid   ipenchk   intforc   ialesof    lagmul    pfacmm      thkf
         0         0         0         0       0.0         0       0.0
```

Figure 22: *LS-DYNA* card used to define the contact algorithm.

The card is explained in detail on the *LS-DYNA* Keyword User's Manual [44]. However, it is important to point out the main controlling parameters: *PFAC*, the penalty factor; *DAMP*, the damping factor; and *NQUAD*, the number of coupling points per Lagrangian element. These parameters are later investigated in this study.

Other parameters of interest for slamming models are: *SLAVE* and *MASTER*, used to define the coupling parts; *CTYPE*, to select the coupling algorithm; and *MCOUP*, which defines the ALE materials for coupling.

3.4. Equations of State

An Equation of State (EOS) is a thermodynamic relation that describes the state of a material in a physical condition in function of variables such as temperature, pressure, density and internal energy (Hedayati and Sadighi, 2015 [67]). In other words, the thermodynamic behaviour of a fluid or solid in a given set of environmental conditions is described by such equation. A well-known example is the ideal gas law.

In the case of non-ideal fluids, several semi-empirical EOSs have been developed for different applications. For instance, the Linear Polynomial and the Gruneisen equations of state are the most commonly used for fluid domains in the numerical modeling of slamming. Both EOSs are available in *LS-DYNA* and are used in the development of the models in this study.

The Linear Polynomial EOS, is a polynomial equation of state combined with a linear internal energy per initial volume E (*LS-DYNA* Theory Manual [15]). The pressure p is given by:

$$p = C_0 + C_1\mu + C_2\mu^2 + C_3\mu^3 + (C_4 + C_5\mu + C_6\mu^2)E \tag{19}$$

Where C_0, C_1, C_2, C_3, C_4, C_5 and C_6 are user defined constants. The parameter μ is described by:

$$\mu = \frac{1}{V} - 1 \tag{20}$$

With V as volume. For a gas model:

$$C_0 = C_1 = C_2 = C_3 = C_6 = 0 \tag{21}$$

$$C_4 = C_5 = \gamma - 1 \tag{22}$$

Where γ is the ratio of specific heats (C_p/C_v). With C_p the specific heat of the fluid at constant pressure and C_v at constant volume.

The Gruneisen EOS defines the pressure for compressed materials based on the cubic shock velocity-particle velocity (*LS-DYNA* Theory Manual [15]). The pressure is defined as:

$$p = \frac{\rho C^2 \mu \left[1 + \left(1 - \frac{\gamma_0}{2}\right)\mu - \frac{\alpha}{2}\mu^2\right]}{\left[1 - (s_1 - 1)\mu - s_2 \frac{\mu^2}{\mu+1} - s_3 \frac{\mu^3}{(\mu+1)^2}\right]} + (\gamma_0 + \alpha\mu)E \tag{23}$$

Where E is the internal energy per volume unit, C is the intercept of the cubic shock velocity-particle velocity curve, γ_0 is the Gruneisen gamma and α is the first order volume correction. Constants C, s_1, s_2, s_3, γ_0 and α are user defined parameters in *LS-DYNA*. The parameter μ is given by Eq. 20.

A comparison of results of slamming impact with different EOSs is presented in Sec. 5.7.6.

4. Fiber Reinforced Composite Materials

A composite material is a combination of two or more insoluble constituents that produce a single material with improved properties. A composite ply is formed by a matrix and a dispersed reinforcement, either fibers or particles, arranged in a random or structured manner. The matrix is a continuous material; usually a polymer, that encases the dispersed elements, defines the shape of the component and guarantees that loads are transferred between reinforcements. The reinforcements, in most cases, provide the load-bearing capability, being harder, stronger and stiffer than the matrix (Campbell, 2010 [13]).

One of the main advantages of composites is their high stiffness and strength associated to a low density. A composite component can be much lighter than a similar part fabricated in a metallic alloy without loosing in terms of mechanical properties. Additionally, by properly selecting the proportion matrix-reinforcement, the arrangement and orientation of the reinforcements, the material can be specifically optimized for a certain application.

Composites have been widely applied in the marine industry since the mid 1940's when they first started being applied in the hulls of patrol boats (Selvaraju and Ilaiyavel, 2011 [75]). These lightweight, strong, corrosion resistant materials present an attractive alternative to steel and aluminum alloys in a number of applications, not only in the naval sector, but also in the leisure, sporting and commercial shipbuilding industries.

Figure 23: Port bow view of the USS Cowpens (CG 63) shows its sonar dome (From: [80]).

An example of an advanced marine application for composites are bow sonar domes. These hydro-dynamically shaped components are mounted on the keel of naval vessels, serving as a protective case for the sensitive sonar equipment (see Fig. 23). Composite materials are ideal for these elements, providing structural strength and durability, while being lightweight, acoustically transparent and reducing resonance.

Composites can be classified according to the type and arrangement of the reinforcements, being fiber or particle reinforced. The first type is categorized into discontinuous or continuous long fibers with unidirectional, bidirectional or random orientation. Furthermore, a basic composite element, formed by a single sheet of the combination matrix-fiber, is called a ply or layer.

The current study is focused on Fiber Reinforced Plastics (FRP) with unidirectional continuous long fibers, which are applied in components such as the sonar dome mentioned previously.

An overview on the fundamental mechanical properties of these particular composites, the corresponding modeling techniques used in *LS-DYNA* and the applied failure criteria is presented in the next sections. The purpose is to provide a theoretical background for the analysis of a composite sonar dome subjected to slamming performed in Sec. 8.

4.1. General Aspects

Materials that present different mechanical properties for each direction at a certain point in the body are denominated anisotropic materials (see Fig. 24). As no material symmetry planes exist, the response to loading is a function of the application direction (Campbell, 2010 [13]).

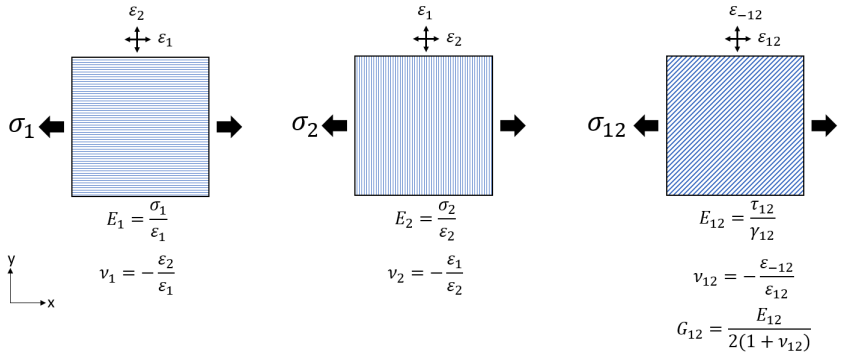

Figure 24: Schematic diagram showing the anisotropic behavior of a FR composite material. The blue lines represent the fiber direction. The index on the parameters is related to the material coordinate system.

Unidirectional fiber reinforced composites, in particular, are classified as orthotropic, a subclass of anisotropic materials where three perpendicular axes define the mechanical properties of the ply (see Fig. 25). These reference material axes are referred to as the principal material coordinate system.

The moduli of elasticity E, shear G and the Poisson's coefficient ν of the material are shown with the corresponding indices for each direction of the principal material coordinate system in Fig. 24.

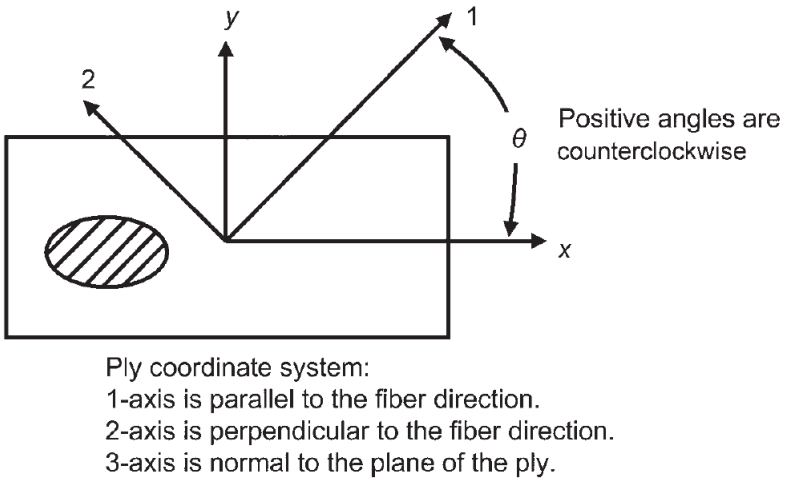

Figure 25: Principal material coordinate system describing the mechanical properties of a unidirectional composite ply. (From: Campbell, 2010 [13]).

In a unidirectional ply, the fiber has the role of supporting longitudinal tension and compression loads (parallel to axis 1), whereas the matrix guarantees the distribution of the loading between the fibers in tension and prevents them from buckling in compression. The matrix is the main carrier in inter-laminar shear and transverse tension (parallel to axis 2).

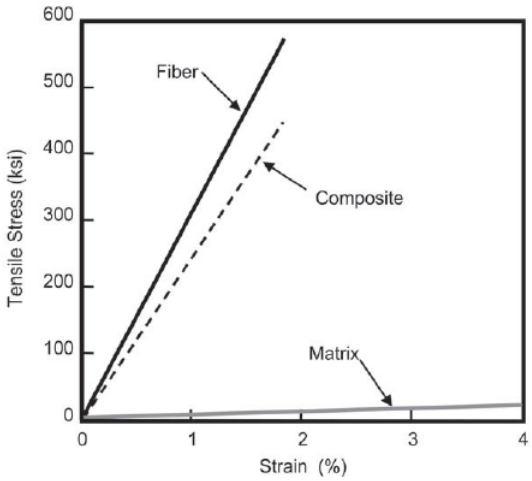

Figure 26: Comparison of tensile properties for fiber, matrix and composite. (From: Campbell, 2010 [13]).

So considering the ply in Fig. 25; for a load applied parallel to axis 1, the response is governed by the high-strength fiber. In this case, the modulus of elasticity of the ply in direction 1 E_1 approximates that of the reinforcement, as demonstrated in Fig. 26. However, if a load is applied perpendicular to the fiber direction in axis 2, the material response is governed by the matrix, with a modulus of elasticity E_2. Generally, E_2 is lower than E_1. The stress-strain relation for composites is shown in Fig. 26, where the relative

role of fiber and matrix is demonstrated.

A FR composite is generally formed by several single thin layers of material stacked on top of each other, as illustrated in Fig. 27. When all the plies are aligned in a single direction, the lay-up is called a lamina. However, since the material has direction dependent properties, the plies can be stacked at different relative angles, thus reinforcing the material in specific directions. This configuration is called a laminate.

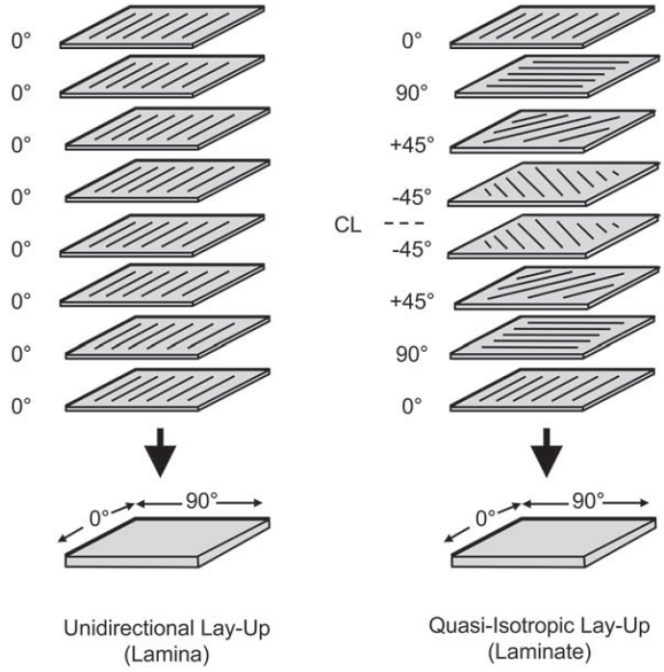

Figure 27: Lay-up composite configurations. (From: Campbell, 2010 [13]).

The unidirectional lamina shown in Fig. 27 is stronger and stiffer in the 0° direction, aligned with the fiber orientation. In the 90° direction, however, the polymeric matrix must carry the load and the composite is weaker. A quasi-orthotropic laminate, on the other hand, is strong and stiff in all four directions (0°, 90°, 45° and −45°). A laminate can be assembled with different relative angles, number of layers and stack-up sequence according to the structural requirements the application.

4.2. Fundamental Property Relationships

One of the most important factors governing the properties of composites is the relative proportion of matrix (m) and fibers (f) in a ply. These values, defined as volume or weight fractions (V_f, V_m, W_f, W_m) are given by the following equations:

$$V_f = \frac{v_f}{v_c} \; and \; V_m = \frac{v_m}{v_c} \tag{24}$$

$$W_f = \frac{w_f}{w_c} \; and \; W_m = \frac{w_m}{w_c} \tag{25}$$

Where v_f, v_m, v_c, w_f, w_m and w_c are, respectively the volume and weight of the fiber, the matrix and the composite.

The longitudinal modulus of elasticity E_1 of a unidirectional FR lamina or laminate is given by the following equation:

$$E_1 = E_f V_f + E_m V_m \tag{26}$$

Where E_f, E_f, V_F and V_m are the moduli of elasticity and the volume fractions for fiber and matrix.

For a longitudinal load, assuming that all the fibers fail at the same time and that the matrix fails immediately after the fibers, the ultimate longitudinal strength σ_1 of the composite is given by:

$$\sigma_1 = \sigma_f V_f + \sigma_m V_m \tag{27}$$

σ_f and σ_m are the ultimate strengths of fiber and matrix. According to Barbero, 2017 [31], as the properties of the fibers usually dominate in most loading situations, the volume fraction of the matrix can usually be neglected. Therefore equations 26 and 27 are reduced to:

$$E_1 \approx E_f V_f \tag{28}$$

$$\sigma_1 \approx \sigma_f V_f \tag{29}$$

In the transverse direction, E_2 is given by:

$$\frac{1}{E_2} = \frac{V_f}{E_f} + \frac{V_m}{E_m} \tag{30}$$

The Poisson's ratio ν_{12} and the shear modulus G_{12}:

$$\nu_{12} = \nu_f V_f + \nu_m V_m \tag{31}$$

$$\frac{1}{G_{12}} = \frac{V_f}{G_f} + \frac{V_m}{G_m} \tag{32}$$

According to Campbell, 2010 [13]), these micro-mechanical relationships can be applied as a first approach to estimate the properties of a lamina if no experimental data is available.

However, the simplifying assumptions such as considering that all fibers are perfectly aligned and homogeneous, have an impact on the accuracy of these equations.

In practice, micro-defects associated to manufacturing are not taken into account. For design purposes, more accurate values are required and, therefore, laminate properties are determined experimentally.

4.3. Failure Criteria on FR Composite Laminates

One of the most critical design aspects is the prediction of the limit loads to which a structural element can be safely subjected and its failure behavior. As a general definition: failure occurs when a component is no longer able to perform its designed function. Depending on the application of the component, different failure modes might be more or less important. For example, a specific structural element might be considered failed when excessive deflections occur, even if the component has not sustained any damage. So predicting not only when, but also how a component will fail is of extreme importance.

The failure of composites is a complex multi-stage process. Mechanical interactions that take place at intra and inter-laminar levels have a key influence on the way damage and fracture develop. A variety of failure modes that may interact or not results from these mechanisms (Barbero, 2017 [31]). They can be generally divided into matrix cracking, delamination and fiber failure. The most common modes are shown in Fig. 28.

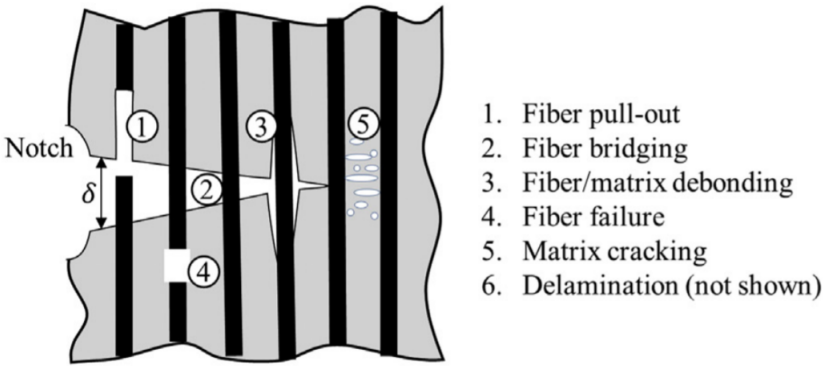

Figure 28: Typical failure modes of a unidirectional ply (From: Bergan et al., 2016 [2]).

The prediction of failure consists essentially in determining the strength and failure mode of a material subjected to a multi-axial stress state. For isotropic materials, the strength of the material is independent of the direction, which rather simplifies the process. In a composite, as a result of its orthotropicity, maximum stresses might not necessarily be aligned with the direction of maximum strains. This property combined with the complex failure mechanisms create a context where conventional failure criteria are insufficient.

Several criteria for fiber reinforced composites have been developed in the last decades. The World Wide Failure Exercises, for instance, were a international program established to compare existent criteria for composites. Around 20 different criteria were compared between themselves and against experimental data for bi-axial lamina and laminate tests. No final conclusion, however, was reached for a definitive criterion capable of accurately predicting rupture for all loading configurations (Gay, 2014 [17]).

Failure criteria are essentially polynomial equations adjusted to fit experimental results on single unidirectional ply failure. A failure envelope is then built based on this approximation. However, the criterion must also be extendable to laminates with varying fiber directions. This is usually done by complementing the criterion with laminate failure analysis for the first ply of the laminate (FPF). Further description of the material failure behavior beyond the first ply failure can only be performed with an understanding of the progressive damage mechanics, as stated by Barbero, 2017 [31].

Most of the existent criteria can be classified into two different approaches: directly considering failure modes and not directly considering failure modes (Paris and Jackson, 2001 [21]). Criteria that use the first approach are, for example, Tsai-Hill and Tsai-Wu. In the second approach, Maximum Stress and Strain, Hashin and Chang-Chang criteria can be cited.

The current study addresses the Tsai-Wu and the Chang-Chang criteria, which are both available in the material formulation used in *LS-DYNA*.

4.3.1. Tsai-Wu Failure Criterion

The Tsai-Wu criterion is an empirical model based on the maximum distortion energy of the material, analogous to the Von Mises criterion for isotropic materials. It uses a quadratic polynomial approximation and assumes the existence of a failure surface in the stress space and strength similarity in plane shear (Gay, 2014 [17]).

A plane stress state for a unidirectional ply is described by:

$$\left(\frac{1}{X_t}-\frac{1}{X_c}\right)\sigma_1+\left(\frac{1}{Y_t}-\frac{1}{Y_c}\right)\sigma_2+\frac{1}{X_tX_c}\sigma_1^2+\frac{1}{Y_tY_c}\sigma_2^2+\frac{1}{S_c^2}\tau_{12}^2-\frac{\sigma_1\sigma_2}{\sqrt{X_tX_cY_tY_c}}=1 \quad (33)$$

Where X_t and X_c are the longitudinal tensile and compressive strengths, Y_t and Y_c are the transverse tensile and compressive strengths and S_c is the in-plane shear strength.

The criterion accounts for tensile and compressive stress through linear terms. It uses stress invariants, being therefore, practical for implementation in computational algorithms.

4.3.2. Chang-Chang Failure Criterion

The Chang-Chang criterion, unlike Tsai-Wu, evaluates the different modes that occur during the progressive failure of the composite. This allows for a more detailed observation of the failure mechanism in a composite laminate at ply-level, which can be desirable in some contexts, e.g., analysis of fatigue and impacts (Chen et al, 2003 [83]).

The three in-plane failure modes considered are: matrix failure, fiber failure and a third one termed fiber-matrix shearing, which is associated to fiber pull-out and debonding (see Fig. 28). The defining equations are presented in Sec. 4.4.1, where the implementation of the criterion in *LS-DYNA* is discussed.

4.4. Modeling of Fiber Reinforced Composites in *LS-DYNA*

There are three basic methods of modeling for laminate composite materials in FEM, differing mainly on the type of elements used. A laminate can be modelled as a single shell element with multiple integration points defining the layers along its thickness; as a stack of 2D shell elements; or as a stack of 3D solid elements representing layers (see Fig. 29).

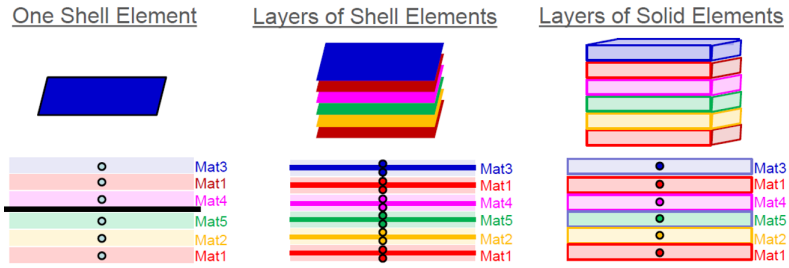

Figure 29: Methods of modeling for composites in FEM. (From: Galal, 2018 [51]).

The selection of the technique depends on the scope of the simulation. For instance, the first approach is the most efficient in terms of computational cost, due to the use of a single shell element. This approach is capable of modeling the elastic response and intra-laminar failure. However, it is not applicable for modeling inter-laminar processes such as delamination. In this case, an approach that uses individual layers of shell or solid elements is required.

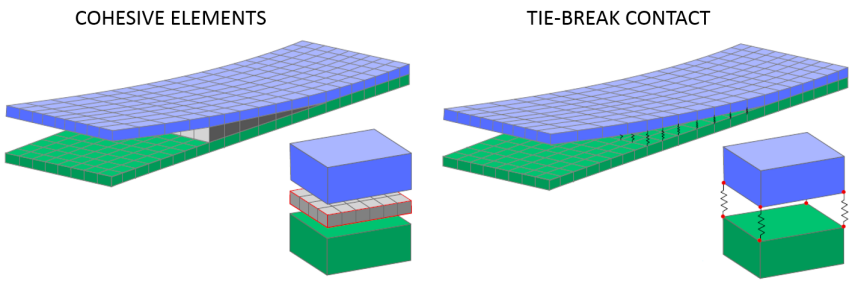

Figure 30: Inter-laminar cohesion techniques. (From: Galal, 2018 [51]).

In order to represent bonding mechanisms and allow the reproduction of inter-laminar damage in these cases, cohesive elements or tie-break contacts can be defined in between layers (see Fig. 30).

Nonetheless, these techniques require intensive calibration of the (de)bonding mechanisms, which combined with the increased computational cost associated to multi-element modelling methods, result in a less attractive alternative in an industrial context.

Several material models for composites are available in *LS-DYNA*. In fact, according to Cherniaev et al. (2018) [3], more than 25 models for composites are suitable for general impact simulations. Some of the most commonly used are summarized in Fig. 31.

	Element	Failure criteria	Comments
***MAT_022:** COMPOSITE_DAMAGE	Shell, Tshell, Solid	Chang-Chang	No fibre compression failure Simple brittle model No crash front algorithm
***MAT_054/55:** ENHANCED_COMPOSITE_DAMAGE	Shell, Tshell, Solid	54: Chang-Chang 55: fibre:Chang-Chang matrix: Tsai-Wu	Improvement of MAT_022 Crash front algorithm Minimum stress limit factor
***MAT_058:** LAMINATED_COMPOSITE FABRIC	Shell, Tshell (1,2)	Modified Hashin. Three different failure criteria: 1. multi-surface, 2. smooth failure surface, 3. faceted failure	Smooth stress-strain relation Non-linear shear behaviour Minimum stress limit factor Exponential softening
***MAT_059:** COMPOSITE_FAILURE_MODEL	Shell, Tshell, Solid, SPH	Modified Hashin	Similar to MAT_054 Crash front algorithm Minimum stress limit factor
***MAT_158:** RATE_SENSITIVE_COMPOSITE_FABRIC	Shell, Tshell	Modified Hashin	Same as MAT_058 Rate sensitive
***MAT_261:** LAMINATED_FRACTURE_DAIMLER_PINHO	Shell, Tshell, Solid	Pinho: Considers the state of the art Puck's criterion for inter-fibre failure	Physical based failure criteria Continuum damage model Linear softening evolution based on fracture toughness
***MAT_262:** LAMINATED_FRACTURE_DAIMLER_CAMANHO	Shell, Tshell, Solid	Camanho: Considers the state of the art Puck's criterion for inter-fibre failure	Physical based failure criteria Continuum damage model Bi-linear/linear softening evolution based on fracture toughness

Figure 31: Material models in *LS-DYNA*. The table demonstrates some commonly used models (From: Galal, 2018 [51]).

The models presented in Fig. 31 rely on different elasto-plastic material behaviors and strategies to predict failure, based either on Progressive Failure (PFM) or Continuum Damage mechanics (CDM). They also vary according to the type of degradation scheme used to reduce the material properties once failure has initiated. For the materials using PFM (MAT022, MAT054, MAT058, MAT059, MAT158), failure criteria such as Chang-Chang, Tsai-Wu or Modified Hashin can be applied.

Selecting the proper material depends on the objective and context of the analysis. This study addresses exclusively MAT054, often utilized in dynamic simulations to assess progressive damage failure. This material formulation is specifically designed to model arbitrary orthotropic materials, such as unidirectional tape composite laminates. It is relatively simple to configure and more computation efficient as opposed to other

formulations, requiring a reduced number of experimental input parameters (Feraboli et al., 2011 [64]).

4.4.1. MAT054 Enhanced Composite Damage

MAT054 Enhanced Composite Damage is a progressive failure material model that uses a ply discount method to reproduce the degradation of the material due to damage. The model is defined in *LS-DYNA* through the input card shown in Fig. 32.

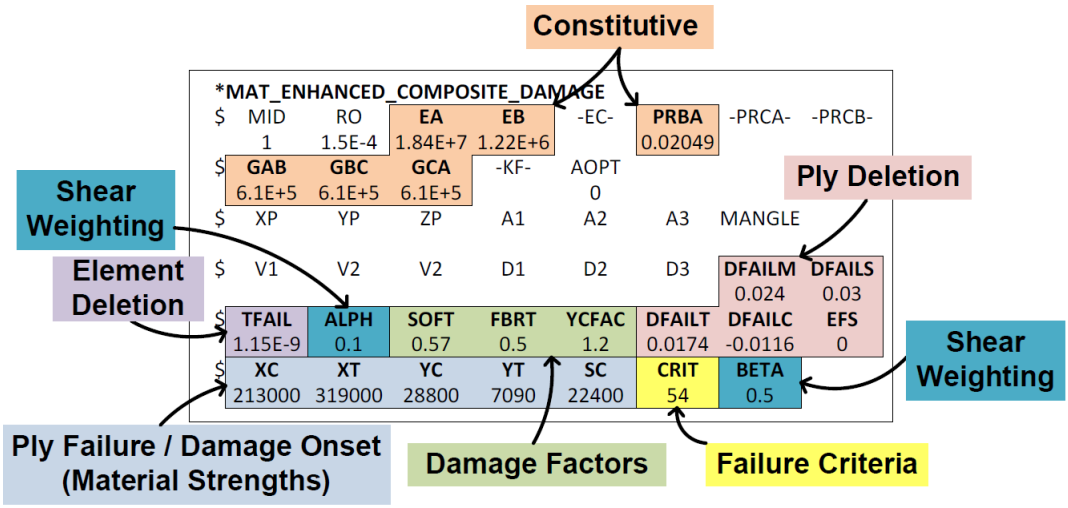

Figure 32: *LS-DYNA* card used to define MAT054 (From: Osborne, 2013 [53]).

The formulation input is composed of a set of constitutive material properties, definition parameters for the material coordinate system and other particular parameters that are used to calibrate material erosion, crash-front softening and material behavior after initiation of the failure. These model-specific parameters, such as TFAIL, SOFT, FBRT, YCFAC, ALPH, BETA and EFS are either non-physical or cannot be measured experimentally. Therefore, a process of trial and error is required to assess their influence on the model responses (Jackson et al., 2014 [19]).

Input parameters highlighted in orange define the constitutive material properties in tension/compression and shear: elasticity (EA and EB) and shear (GAB, GBC and GCA) moduli, and Poisson's ratio (PRBA). These parameters describe the stress-strain behavior of the element in the elastic domain for fiber (1 or A-direction), matrix (2 or B-direction) and shear (12 or AB-direction), respectively:

$$\varepsilon_1 = \frac{1}{E_1}(\sigma_1 - \nu_{12}\sigma_2) \tag{34}$$

$$\varepsilon_2 = \frac{1}{E_2}(\sigma_1 - \nu_{21}\sigma_1) \tag{35}$$

$$2\varepsilon_{12} = \frac{1}{G_{12}}\tau_{12} + \alpha\tau_{12}^3 \tag{36}$$

Where ε are the strains, σ and τ are the normal and shear stresses, E and G are the elastic and shear moduli, and ν is Poisson's coefficient. The parameter ALPH is a shear weighting factor used to correct the non-linear shear stress term in the stress-strain relationship. It must be calibrated by trial and error if shear is expected.

After the elastic limit is reached, two different failure criteria are available: Chang-Chang or Tsai-Wu. The selection of the criterion is done with input CRIT, where 54 is Chang-Chang and 55 is Tsai-Wu. Parameters highlighted in light blue on Fig. 32: XT, XC, YT, YC and SC are, respectively, the ply longitudinal tensile strength, longitudinal compressive strength, transverse tensile strength, transverse compressive strength, and shear strength. They define the limit stresses on ply-level and mark the initiation of lamina degradation (see Fig. 33). These parameters are obtained experimentally.

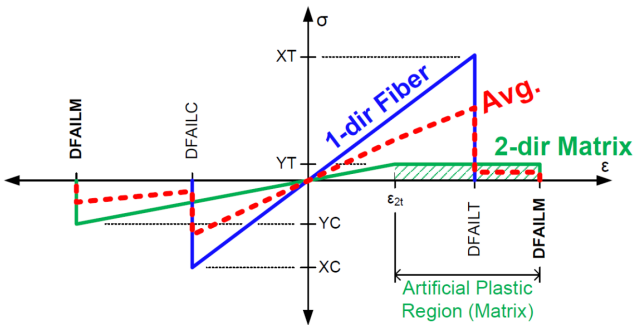

Figure 33: Stress-strain behavior of a lamina. Stress-strain curves for matrix, the fiber and the average are shown (From:Osborne, 2013 [53]).

The failure modes for the strength-based Chang-Chang criterion for a linear elastic material are given by (*LS-DYNA* Theory Manual [15]):

- for the tensile fiber mode, where $\sigma_1 \geq 0$:

$$e_f^2 = \left(\frac{\sigma_1}{X_t}\right)^2 + \beta\left(\frac{\tau_{12}}{S_c}\right)^2 - 1 \quad \begin{cases} e_f^2 \geq 0 & \text{failed} \\ e_f^2 < 0 & \text{elastic} \end{cases} \tag{37}$$

  Upon failure: $E_1 = E_2 = G_{12} = \nu_{12} = \nu_{21} = 0$

- for the compressive fiber mode, where $\sigma_1 < 0$:

$$e_c^2 = \left(\frac{\sigma_1}{X_c}\right)^2 - 1 \quad \begin{cases} e_c^2 \geq 0 & \text{failed} \\ e_c^2 < 0 & \text{elastic} \end{cases} \tag{38}$$

  Upon failure: $E_1 = \nu_{12} = \nu_{21} = 0$

- for the tensile matrix mode, where $\sigma_2 \geq 0$:

$$e_m^2 = \left(\frac{\sigma_2}{Y_t}\right)^2 + \beta\left(\frac{\tau_{12}}{S_c}\right)^2 - 1 \quad \begin{cases} e_m^2 \geq 0 & \text{failed} \\ e_m^2 < 0 & \text{elastic} \end{cases} \tag{39}$$

  Upon failure: $E_2 = \nu_{21} = G_{12} = 0$

- for the compressive matrix mode, where $\sigma_2 < 0$:

$$e_d^2 = \left(\frac{\sigma_2}{2S_c}\right)^2 + \left[\left(\frac{Y_c}{2S_c}\right)^2 - 1\right]\frac{\sigma_2}{Y_c} + \left(\frac{\tau_{12}}{S_c}\right)^2 - 1 \quad \begin{cases} e_d^2 \geq 0 & \text{failed} \\ e_d^2 < 0 & \text{elastic} \end{cases} \tag{40}$$

  Upon failure: $E_2 = \nu_{12} = G_{12} = 0$

In the Tsai-Wu criterion, tensile and compressive fiber modes are treated in the same way as in the Chang-Chang criterion, according to *LS-DYNA* Theory Manual [15]. For the matrix tensile and compressive failure modes, the following formulation is given:

$$e_{md}^2 = \frac{\sigma_2^2}{Y_c Y_t} + \left(\frac{\tau_{12}}{S_c}\right)^2 + \frac{(Y_c - Y_t)\sigma_2}{Y_c Y_t} - 1 \quad \begin{cases} e_{md}^2 \geq 0 & \text{failed} \\ e_{md}^2 < 0 & \text{elastic} \end{cases} \tag{41}$$

Parameters e_f, e_c, e_m, e_d and e_{md} are history variables that mark the failed plies for each of the modes (see Fig. 34).

History Variable	Description	Value	LS-PREPOST History Variable
1. *ef* (*i*)	tensile fiber mode	1 – elastic 0 – failed	1
2. *ec*(*i*)	compressive fiber mode		2
3. *em*(*i*)	tensile matrix mode		3
4. *ed*(*i*)	compressive matrix mode		4
5. *efail*	max[*ef* (*ip*)]		5
6. *dam*	damage parameter	-1 - element intact 10-8 - element in crashfront +1 - element failed	6

Figure 34: Definition of history variables in *LS-DYNA* (*LS-DYNA* Theory Manual [15]).

Where the index i defines corresponding integration point.

The parameter β (BETA in the input card) is a user-defined shear weight factor that determines the influence of shear in the tensile fiber mode. For BETA=1, the original Hashin failure criterion is applied. For BETA=0, the Maximum Stress criterion is selected.

The failure process occurs in the following manner: as one of the failure conditions is reached in a ply within the element, the elastic properties of the ply are set to zero. This

reduction of properties, is done by imposing the stress state just before failure on the next time-steps and preventing the failed ply to support any additional stress, instead of reducing stresses to zero (see Fig. 35).

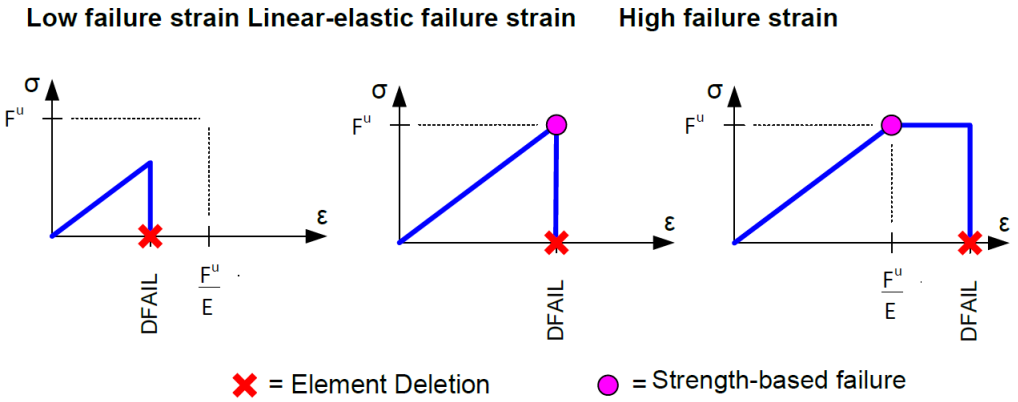

Figure 35: Three basic stress-strain behaviors defined by MAT054. The first and second one on the left present a low strain failure limit and the third one, on the right, presents a high failure strain and an artificial plastic behavior (From:Wade et al., 2012 [11]).

In this numerical process, the ply is not actually failed, but rather remains intact and loses its load carrying capacity, differently from what would occur in reality. This is clearly demonstrated in the third case in Fig. 35. A sort of artificial plasticity is maintained beyond the elastic limit until a determinate limit strain value (DFAIL) triggers ply deletion, reducing stresses in the ply to zero.

The five critical strain parameters observed in pink on Fig. 32: DFAILT, DFAILC, DFAILM and DFAILS are, respectively, the strain failure in fiber tension, fiber compression, in the matrix direction and in shear. These values are obtained experimentally through coupon-level tests (Osborne, 2013 [53]). However, if these values are not known beforehand, an alternative non-physical parameter available in *LS-DYNA* can be used, the Effective Failure Strain (EFS), given by (*LS-DYNA* Theory Manual [15]):

$$EFS = \sqrt{\frac{4}{3}(\varepsilon_1^2 + \varepsilon_1\varepsilon_2 + \varepsilon_2^2 + \varepsilon_{12}^2)} \tag{42}$$

By calculating ε_1, ε_2 and ε_{12} at element failure and applying Eq. 42, a critical EFS can be determined. The default value of EFS is zero.

The deletion of a shell element with MAT054 occurs when all the integration points (plies) in the element exceed one of the strain parameters (DFAIL or EFS). Additionally, element deletion can also be imposed to elements that present severe distortion, in which case the required time-step size becomes very small. This optional method of element deletion can be calibrated with the parameter TFAIL.

After an element is deleted, an algorithm of strength reduction of the surrounding elements

takes place in order to reproduce damage propagation. The surrounding elements become part of a crash-front region (see Fig. 36), where the strength reduction is controlled through parameters SOFT, FBRT and YCFAC, highlighted in green in Fig. 32.

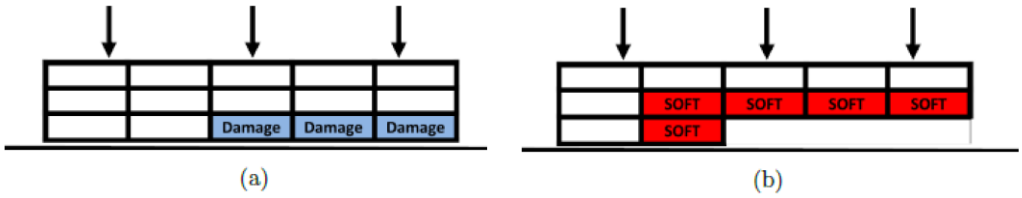

Figure 36: Crash-front algorithm used to perform the strength reduction of elements affected by surrounding damage (From:Andersson and Liedberg, 2014 [45]).

From Fig. 36, in (a) the elements in blue are failed through the strength based criterion. In (b) these elements reach critical strain and are deleted. Elements in red become part of crash-front region. The damage factor SOFT is applied in crush simulations, whereas FBRT and YCFAC are required for matrix compressive failure. These parameters cannot be obtained experimentally and, therefore, need to be tuned by trial and error.

In conclusion, according to Feraboli et al. (2011) [64], MAT054 is commonly applied on impact simulations on composites due to its relative simplicity and low computational cost. However, the model also presents significant drawbacks regarding the non-physical parameters. The process of calibrating these values requires an intensive sensitivity analysis, which can become quite challenging. Nonetheless, the model can be used with reasonable accuracy to predict the behavior at higher structural level, such as components or full-scale models. This material is further applied in this study.

4.4.2. Coordinate Systems for Composites in *LS-DYNA*

There are three different coordinate systems (CS) considered for reference in the modeling of composite materials in *LS-DYNA*: the global CS [X,Y,Z], the element or local CS [x,y,z] and the material CS [a,b,c], as presented in Fig. 37.

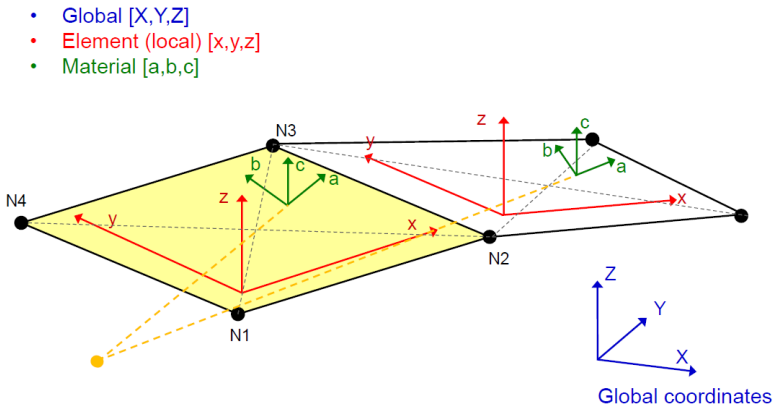

Figure 37: Coordinate systems used for composite shell elements (From: Galal, 2018 [51]).

In order to properly model a laminate, it is critical to define the correct material CS for each element, since the ply direction is set according to this specific reference. Additionally, in *LS-DYNA*, the results for stresses and strains can be displayed in any one of the coordinate systems, and post-processing these values in the material CS is generally more comprehensive. This is specially the case for more complex geometries, where global and material stresses/strains can be greatly different.

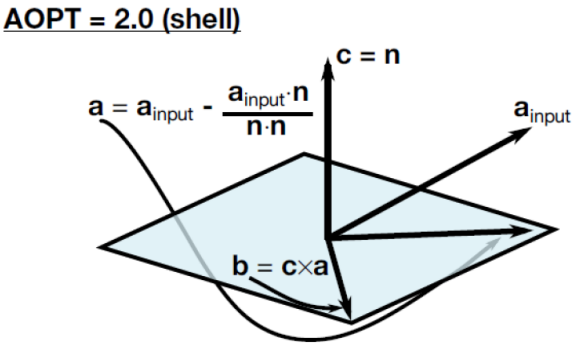

Figure 38: Material Coordinate System defined for a shell element AOPT=2 (From: Galal, 2018 [51]).

The selection of the coordinate system on which results are displayed is done in card DATABASE_EXTENT_BINARY. Moreover, according to the element type, the material CS is formulated in different manners. For globally orthotropic shell elements, the CS is designated as shown in Fig. 38. The parameter AOPT in MAT054 defines the type of material CS. The direction of each ply is defined in the card PART_COMPOSITE.

5. Case Study 1: 2D Rigid Wedge

As a first approach to validate the settings of the ALE formulation in *LS-DYNA*, a 2D model of the slamming of a rigid wedge is developed and compared against experimental results obtained in the drop test study by Zhao et al. (1996) [72].
Finite Elements models of the experiment developed in Stenius and Rosén (2007) [27], Yu et al. (2019) [84] and Aquelet (2004) [58] are used as reference for the numerical setup.

Once the results obtained with the 2D rigid wedge are satisfactory, the complexity of the simulation can be further increased by implementing elasto-plastic materials, extending to a three-dimensional model and finally implementing anisotropic materials.

5.1. Experimental Setup

Zhao et al. (1996) [72] carried out drop tests in order to validate the two proposed theoretical methods for slamming prediction. The experimental drop rig is described in detail in Sec. 2.3. The compared test section consists of a V-shaped wedge with a deadrise angle (α) of 30°. It has a total length of $1m$ and a breadth of $0,5m$, with a defined measuring section of $0,2m$ in the center (see Fig. 39). The maximum drop height is $2m$.

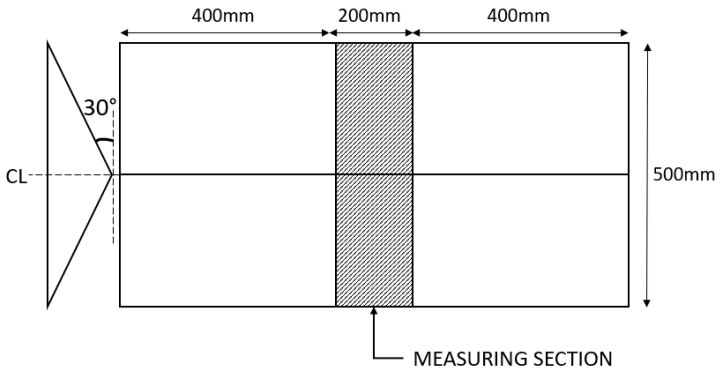

Figure 39: Transverse and longitudinal dimensions of the test section.

Table 1: Wedge dimensions and mass distribution from Zhao et. al (1996) [72].

Breadth of section	500 mm
Length of measuring sections	200 mm
Length of each dummy sections	400 mm
Total length	1000 mm
Weight of drop rig (without ballasts)	141 kg
Ballast weight	100 kg
Total weight of the drop rig	241 kg
Weight of the measuring section	14,5 kg

Ballast can be added to the horizontal attachment so weight adjustments are possible. General dimensions and weights are presented in Table 1:

The ends of the measuring section are connected to the rig with two force transducers, which register the impact force. To assess the pressure distribution along the wedge, transducers are placed in specific points on the measuring section, as shown in Fig. 40.

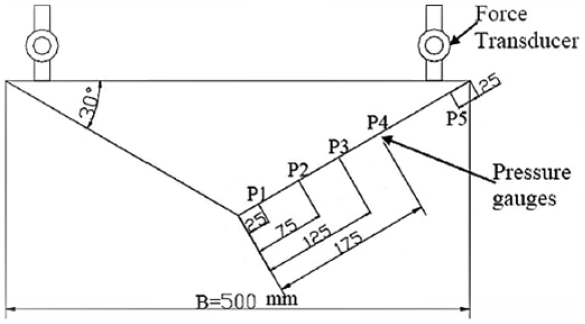

Figure 40: Transversal dimensions of the wedge and position of pressure transducers. (From: Zhao et al. (1996) [72])

5.2. Model Geometry and Boundary Conditions

The model geometry, presented in Fig. 41, is composed of the wedge and the fluid domain divided in two parts: water and air. General dimensions of the fluid domain are defined primarily according to the geometry in Yu et al. (2019) [84]. However, a sensitivity study on the geometry is presented in Sec. 5.7.7.

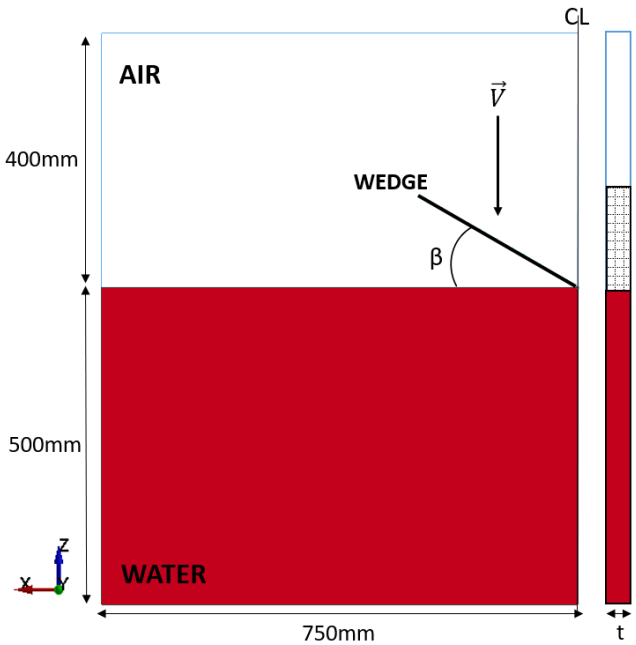

Figure 41: Model setup of the rigid wedge. CL is the symmetry axis. Top, left and bottom edges are non-reflecting boundaries. Dimension t is defined by the minimum mesh element size.

The problem is symmetric, and therefore only half of the geometry is modeled. The nodes of the fluid domain located in the symmetry axis are constrained in X direction. Non-reflecting boundaries are applied at all edges, except on the middle plane. This condition assures that there is no influence of reflected waves on the pressure field generated by the impact. Furthermore, to enforce the two-dimensional assumption, all nodes are constrained in Y direction.

An initial velocity of $6,15m/s$ is applied to the wedge, corresponding to the velocity of the body just before impact, as observed in the experiment by Zhao et. al (1996) [72].

5.3. Material Properties and Equations of State

Material properties for the fluids are set with the card MAT_NULL, while the wedge is defined with MAT_RIGID, as presented in Table 2. The pressure cutoff coefficient is initially set to zero. Gravity and viscosity of the water are neglected.

Table 2: Material properties.

	Material Type	Density (kg/m^3)
Wedge	RIGID	2700
Water	NULL	1026
Air	NULL	1,23

For an observation of the effects of the Equation of State (EOS) in the results, two formulations are tested: Gruneisen and linear polynomial. Parameters for both formulations are listed in Tables 3 and 4.

Table 3: Coefficients for the Gruneisen EOS. (From: Wu et al. 2018) [12])

	C	S_1	S_2	S_3	γ_0	A	E_0	V_0
Water	1480	1,92	0	0	0	0,1	0	0
Air	0	0	0	0	0	0	0	0

Table 4: Coeffcients for the linear polynomial EOS. (From: Bae and Zakki [16])

	C_0	C_1	C_2	C_3	C_4	C_5	C_6	E_0	V_0
Water	0	2002	8436	8010	0,4394	1,3937	0	0,2086	1,0
Air	0	0	0	0	0	0	0	0,25	1,0

The card ELEMENT_MASS is used to distribute the mass of the wedge between all the nodes of the Lagrangian mesh. It is noted that the mass must be defined proportionally to the size of the model with a simple ratio calculation between the total length of the wedge

($1000mm$), the total ballasted weight of one half wedge ($241kg/2$) and the longitudinal length of the 2D model (size of minimum element).

5.4. Selection of Mesh

A parameter of critical relevance is the mesh density. Discretization must be sufficiently fine in order to capture correctly pressure gradients and still reasonably coarse in order to be efficient in terms of computational cost (Stenius and Rosén, 2007 [27]).

Both fluids are represented by uniform multi-material Eulerian meshes of 8-node brick elements, while the wedge is described by a Lagrangian strip of uniform shell elements. The chosen element formulation for the shells is Belytschko-Tsay. Lagrangian and Eulerian meshes have a longitudinal thickness of one element as only a section of the model is considered in the 2D setup.

According to the model proposed by Yu et al. (2019) [84], an element size of $2,5mm$ yields a good compromise between accuracy and computation cost. Nevertheless, a sensitivity analysis is performed with $2,5mm$, $5mm$ and $10mm$ meshes. The wedge and the fluids are meshed with elements of the same size.

5.5. FSI Settings

One of the main concerns of the modeling of slamming is the calibration of the parameters that govern the fluid-structure interaction. According to Olovsson (2003) [42], the penalty-based contact formulation is the most appropriate for hull-water impact problems. However, defining the governing parameters of the algorithm, such as the penalty factor (*PFAC*), damping coefficient (*DAMP*), time-step scaling (*TSSFAC*) and number of coupling points per element (*NQUAD*), can be challenging. The calibration depends on the problem being analyzed and results can be very sensitive.

The simulations are performed with a penalty coupling for shell and solid elements (CTYPE=4 in *LS-DYNA*) using different combinations of parameters for an overview of the effect of the FSI configurations on the results. Values used are summarized in Table 5.

Table 5: Tested FSI parameters.

PFAC	0,002	0,01	0,1	0,5
DAMP	0,1	0,5	1,0	2,0
NQUAD	2	4	6	

Moreover, regarding the ALE control settings, the default advection method is chosen; donor cell with Half Index Shift (HIS), first order accurate.

5.5.1. Penalty Factor

One particularly important parameter is the penalty factor, which defines the contact stiffness. If the penalty factor is too high, the contact stiffness might become excessive, leading to numerical instabilities. On the other hand, a too low contact stiffness produces leakage in the Lagrangian structure (Aquelet and Souli, 2003 [60]). Tuning the penalty factor is a trial and error process and a previous knowledge of the magnitude of the involved loads is necessary (Stenius and Rosén, 2007 [27]).

In the case of slamming, the impact force or the contact reaction of the fluid on the structure, is a function of the angle of incidence of the wedge, the velocity and the mass of the body. Aquelet (2004) [58] performs a study where the appropriate penalty factor associated to different deadrise angles is assessed. Results from the study are provided in Table 6. Alternatively, Yu et al. (2019) [84] applies the default value of the card (*PFAC*=0,1).

Table 6: Penalty factor values in function of the wedge angle (Aquelet, 2004 [58]).

Angle [°]	0	1	2	3	4	5	10	20	30
PFAC	10	7	0,340	0,085	0,034	0,018	0,009	0,008	0,002

5.5.2. Damping Coefficient

On slamming simulations, numerical noise in the results might appear, either due to the incompressibility of the fluid that generates high frequency oscillations on the structure or due to an excessive contact stiffness that might affect the eigenfrequency of the virtual coupling system. This numerical instabilities have a negative effect on the accuracy of results. Estimated loads can be unreliable when high levels of numerical noise are present.

Therefore, introducing damping in the algorithm filters out these high frequency oscillations and improves results. Nevertheless, it is important to set the parameter accordingly to the chosen penalty factor. An excessively high coefficient can alter the behaviour of the system by damping out the actual physical oscillations, leading to inaccurate results as well. This occurs if the numerical contact stiffness is close to the highest physical stiffness.

In *LS-DYNA*, the parameter *DAMP* is a damping scaling factor ranging from 0 to 1, where 1 represents a critically damped case. Stenius (2006) [28] recommends a value of 0,9 times the critical damping. Aquelet et al. (2006) [61] proposes the use of *DAMP*=2. Even though this value is not predicted in *LS-DYNA* Keyword User's Manual [44], it is used in the study for a better understanding of the influence of the parameter.

5.5.3. Number of Coupling Points

The parameter *NQUAD* defines the number of quadrature points that connect the Lagrangian slave part to the Eulerian master part. Depending on the relative mesh size between the parts, more or less coupling points are required. As a general guideline, *LS-DYNA* Keyword User's Manual [44] recommends using 2 or 3 coupling points per each Eulerian/ALE element. In general, the bigger the Lagrangian element in relation to the Eulerian, the more coupling points are needed. Moreover, the expansion and contraction of the meshes also need to be taken into account.

5.5.4. Time-step Scaling Factor

Even though the time-step size is of great importance in the stability of the numerical algorithm, this study focus on the settings of the FSI contact card. So as a preliminary approach, the time-step scaling factor is set to default, as recommended in *LS-DYNA* Keyword User's Manual [44].

5.6. Geometry of the Fluid Domain

The initial set-up for the geometry of the fluid domains is based on Yu et al. (2019) [84], as previously mentioned. The boundaries of the domains have an influence on the fluid behaviour, given that the flow is limited at these areas. Therefore, loads on the wedge are also linked to the their sizes. So in order to obtain a more detailed idea of the influence of the boundaries of the geometry on the results, a sensitivity study is performed.

By varying one of the dimensions of the fluid domain, either in the horizontal direction (X) or in the vertical direction (Z), while keeping the other value fixed, the convergence of the vertical slamming force is assessed. The longitudinal in-plane direction (Y) is kept constant.

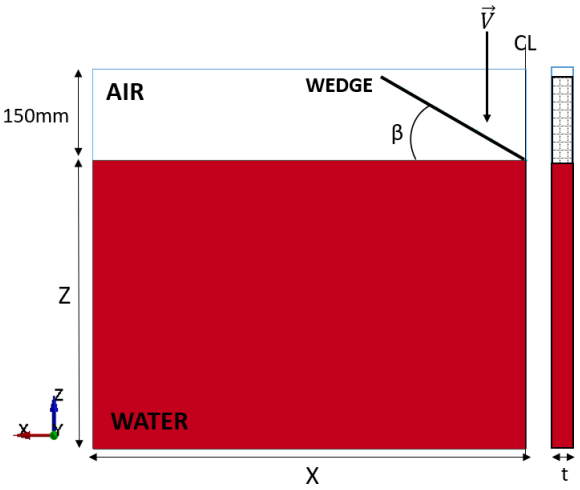

Figure 42: Dimensions Z and X are varied in this analysis ($t = 2,5mm$).

Additionally, the vertical dimension of the air domain is also fixed (see Fig. 42). The space required for this domain is only enough to allow for the motion of the wedge at the wet stages and the correct reproduction of the water splash resulting from the impact. This is also a way to optimize the simulation in terms of computational cost.

The dimensions used in the study are summarized in Table 7. It is noted that for a fixed X, convergence is reached at $Z = 1000mm$.

Table 7: Dimensions used in the sensitivity study.

Fixed Z		Fixed X	
X [mm]	Z [mm]	X [mm]	Z [mm]
300	700	750	200
500	700	750	500
700	700	750	700
1000	700	750	1000
1250	700	-	-

5.7. Results and Discussion

5.7.1. Overall Behaviour

The progression of the wedge into the water and the behaviour of the free-surface is presented in Fig. 43. As the wedge enters the water, the fluid piles up at the intersection between the wedge and the free-surface, forming a water jet that is projected away from the body. The figure was created by plotting the volume fraction. Red represents water, blue represents air and green the smoothed transition.

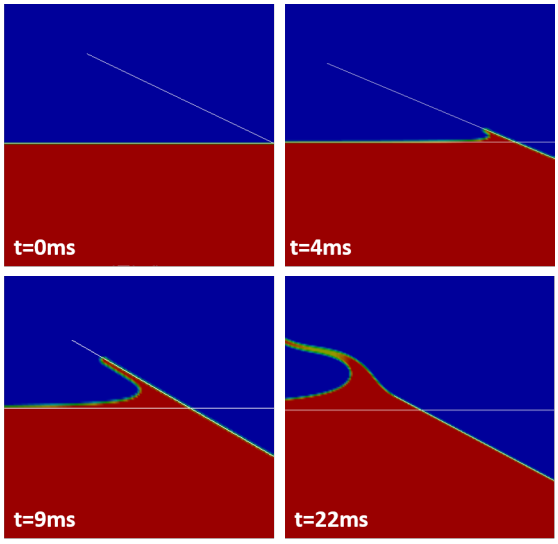

Figure 43: Interaction of the free-surface with the wedge at different instants.

Figure 44 shows a comparative diagram of the simulation at around $t = 20ms$, when the chine is almost completely submerged. The model developed in this work and the result from Yu et al. (2019) [84] yield a similar behaviour. The water jet formed with the fluid detachment can be seen.

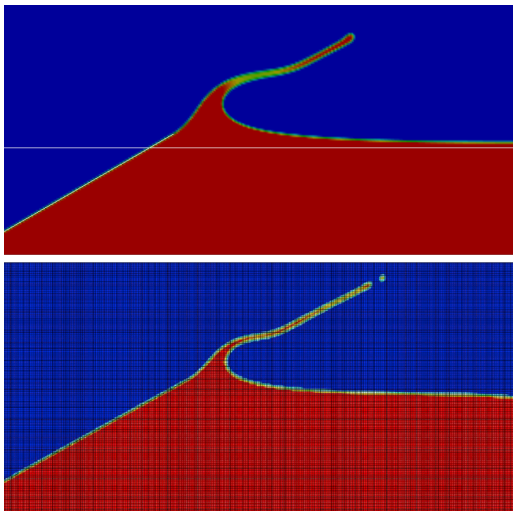

Figure 44: Comparative of the free-surface at $t = 20ms$. Present (upper), Yu et al. (2019) [84] (lower).

Two distinct stages can be observed (see Fig. 45): before the entrance of the chine into the water and after it enters the surface. These two phases are characterized by different pressure distributions.

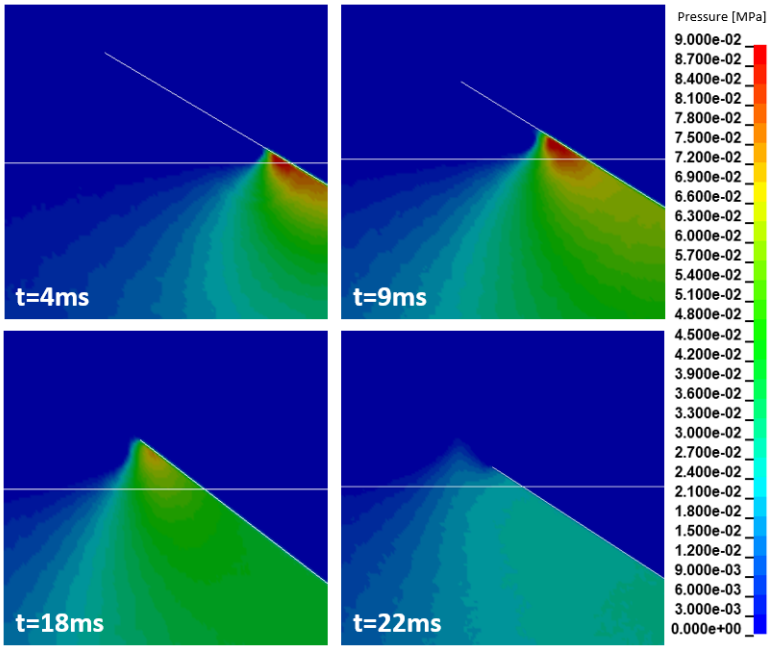

Figure 45: Average pressure evolution. Dry chine stage ($t = 4ms$ and $t = 9ms$) and wet chine stage ($t = 18ms$ and $t = 22ms$).

In the first stage, a localized pressure peak occurs on the pile-up region, while the remaining submerged part of the wedge experiences lower and fairly constant pressures ($t = 4ms$ and $t = 9ms$). In the second phase ($t = 18ms$ and $t = 22ms$), a relatively uniform pressure distribution is observed, decreasing until reaching hydrostatic pressure.

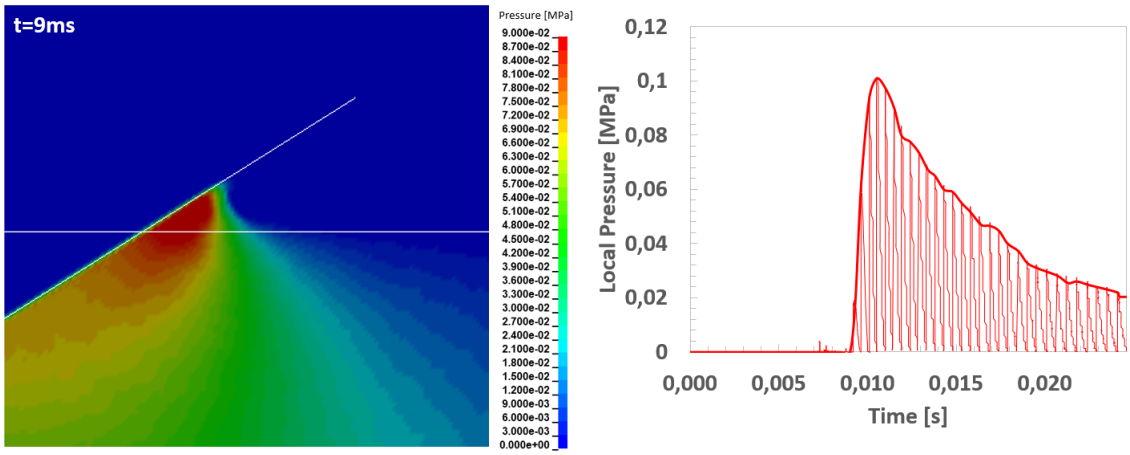

Figure 46: Free surface upon wedge entry and local pressure at the middle of the half wedge ($t = 9ms$).

The local pressure distribution measured at the middle of the half wedge agrees with the expected behaviour (see Fig. 46). A sudden peak pressure occurs when the measurement

point is at the junction of the wedge and the free-surface. As the point moves into the water, a lower pressure plateau gradually develops. Measuring local pressures accurately in *LS-DYNA* proved very difficult, a high level of numerical oscillations is observed. So in order to facilitate the visualization of the pressure distribution, the curve presented in Fig. 46 is a plot of the peak pressures, excluding the zero values that occur between each time-step.

5.7.2. Slamming Force

The slamming vertical force history obtained numerically is compared against the experimental data by Zhao et al. (1996) [72] as well as numerical results presented in Yu et al. (2019) [84], Stenius and Rosén (2007) [27] and Le Sourne et al. (2003) [23].

Results in this section refer to the optimal geometry of the fluid domain and FSI settings assessed in Sections 5.7.7 and 5.7.4. The contact card is configured with $PFAC$=0,002 and $DAMP$=0,1 and the water domain has $1250X2,5X750mm$. The calibration of parameters is further discussed in following the sections.

Figure 47 shows the evolution of the vertical force with time. A peak of $5328N$ is reached at around $15ms$ in the simulation, as opposed to $5126N$ at $13ms$ in the experimental drop-test, an overestimation of approximately 4% for the maximum force. Zhao et al. (1996) [72] estimates a maximum force 20% lower when three-dimensional flow effects are considered, which can be understood by the fact that the fluid flow is not constrained in the longitudinal extremities of the wedge on the 3D case as opposed to the 2D idealization.

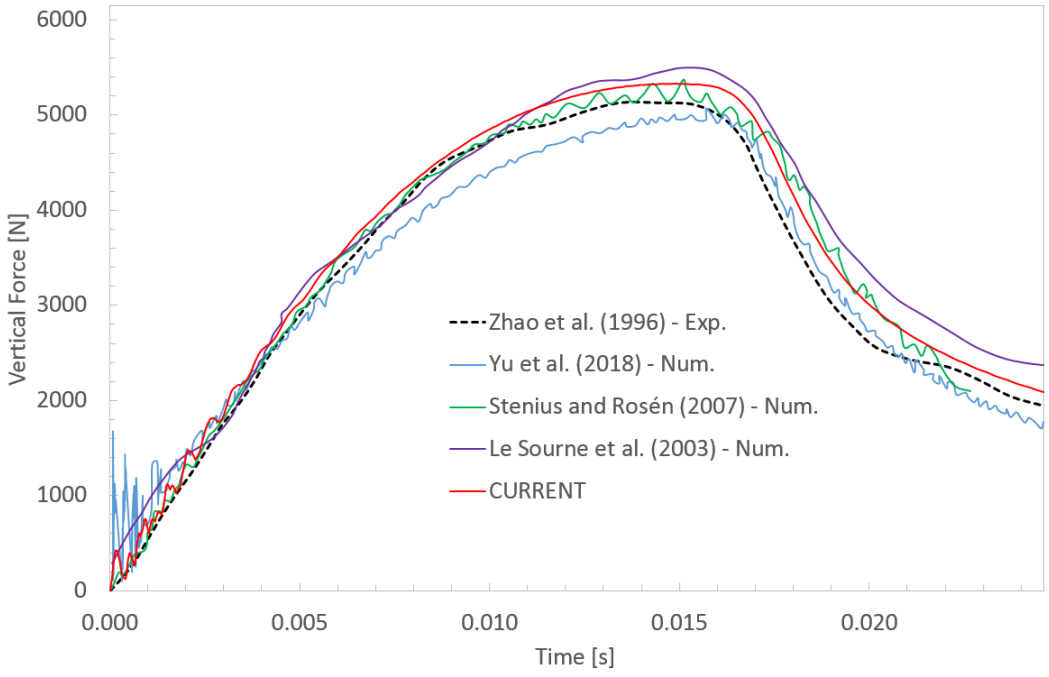

Figure 47: Comparison of the results for the slamming force.

Reference numerical studies are within an average error of 7% and therefore, the current numerical model can be validated within a reasonably good margin of error and an overall well matched profile.

It is important to note that the sensitivity studies presented in the following sections are performed with the initial selected geometry by Yu et al. (2019) [84]. Even though the discrepancy on the magnitude of the maximum force is slightly higher with this model (9%), the assessment of the sensitivity of calibration parameters remains valid.

5.7.3. Mesh Sensitivity

Details of the implemented meshes are summarized in Table 8.

Table 8: Details of the applied meshes.

Elem. size (mm)	2,5	5	10
Number of Elements	108230	27057	6779
CPU Time (min)	38	5	1,2

A comparison of the slamming force for the different meshes is presented in Fig. 48. The $2,5mm$ mesh converges to the expected result. Some numerical noise is observed in the beginning of the simulation, but the curve is overall fairly stable. For the $5mm$ mesh, the curve seems to converge, however, considerable oscillation is present. The $10mm$ mesh differs significantly from the expected result.

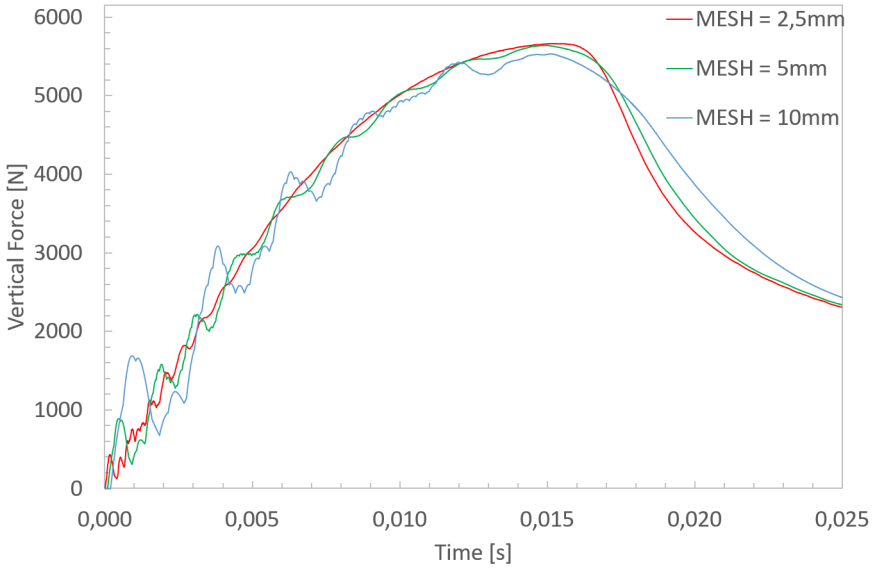

Figure 48: Mesh sensitivity of the slamming force.

The $2,5mm$ mesh is selected for the model, since it yields good results and runs at a reasonable CPU time (around 40 min). A finer mesh would not be practical and necessary for this case.

5.7.4. FSI Settings

Figures 49, 50, 51 and 52 present variations of the curve for the slamming force obtained with different combinations of penalty factors and damping coefficients. In general, except for the cases when numerical instabilities are significant, the maximum force as well as the overall shape of the curve do not change significantly for different FSI configurations.

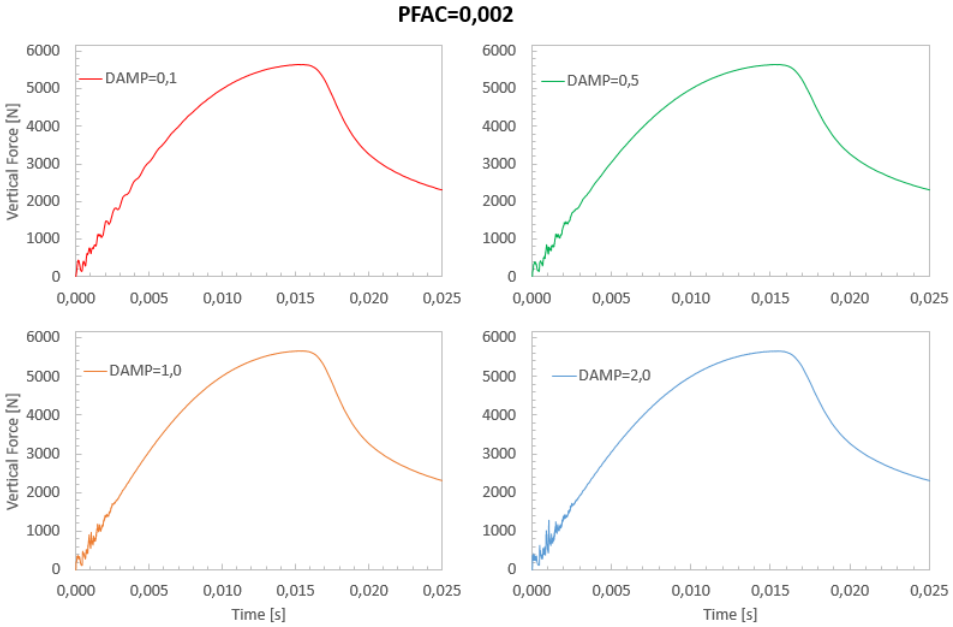

Figure 49: Damping sensitivity analysis with $PFAC$=0,02.

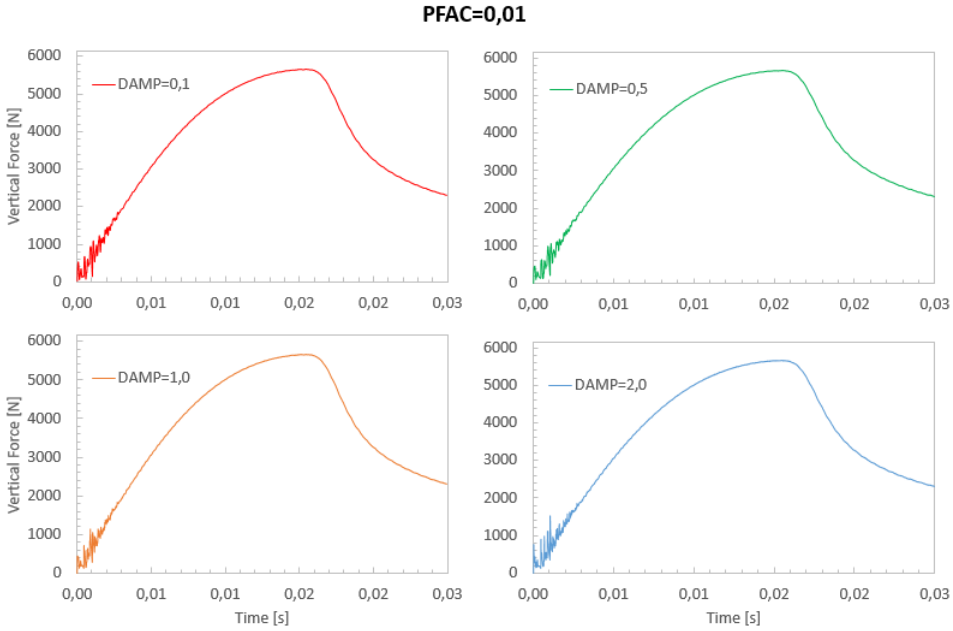

Figure 50: Damping sensitivity analysis with $PFAC$=0,01.

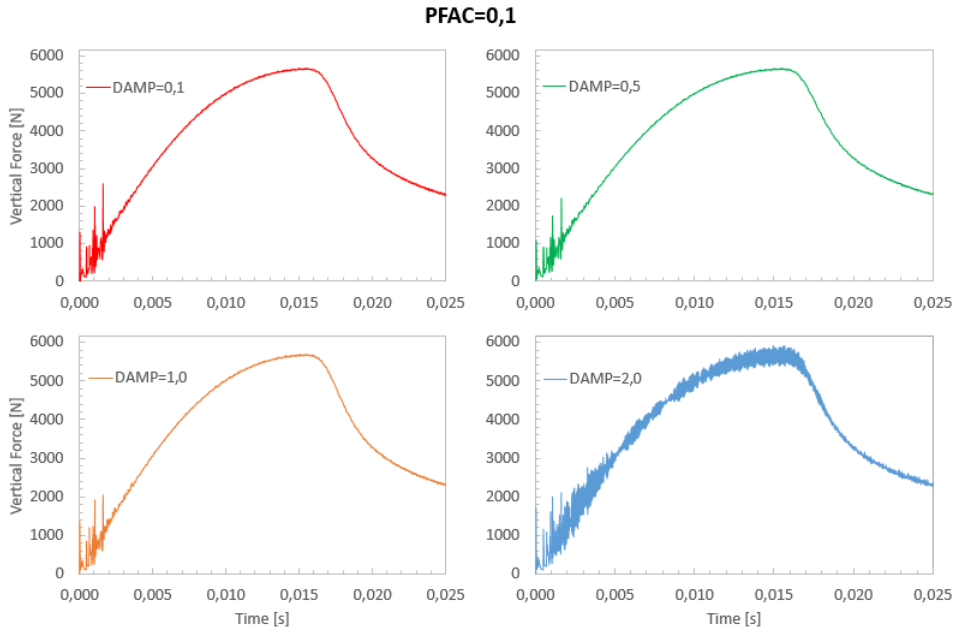

Figure 51: Damping sensitivity analysis $PFAC$=0,1.

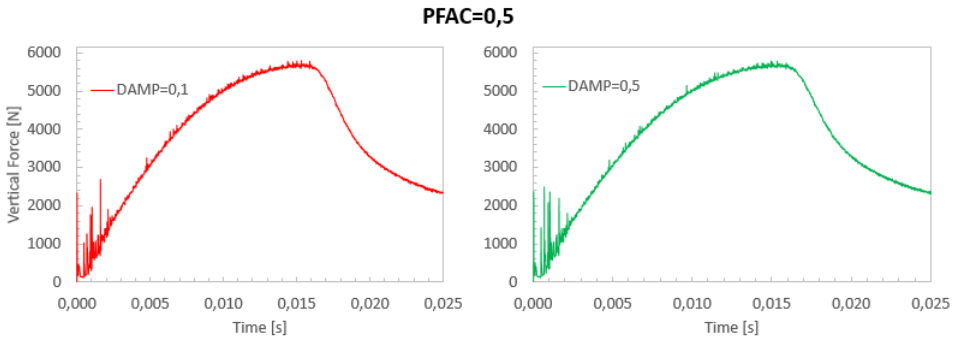

Figure 52: Damping sensitivity analysis $PFAC$=0,5.

As the penalty factor increases, numerical instabilities arise. The lowest levels of numerical noise are observed with the combination $PFAC$=0,02 and $DAMP$=0,1. With a $0,5$ penalty factor and damping coefficients higher than $0,5$, the simulation does not converge.

According to Aquelet et al. (2006) [61], the higher the penalty factor, the smaller the interpenetration allowed at the nodes of the contact interface. At a very high contact stiffness, when penetrations are zero, the interface boundary condition is satisfied. However, with this excessively stiff contact, the frequency of the virtual spring-damper system of the contact algorithm increases and numerical instabilities might appear. In order to prevent this effect, a lower stiffness with the presence of some leakage in the Lagrangian component is acceptable.

It is observed that similarly to the penalty factor, an excessively high damping coefficient can generate unstable coupling. This behaviour can be well observed when the combination $PFAC$=0,1 and $DAMP$=2,0 is used (Fig. 51).

In summary, for defining the FSI in the case of wedge slamming, the best approach is to define a contact stiffness based on the angle of incidence and tune the damping coefficient accordingly. This procedure can be probably extended to more practical scenarios involving similar geometries.

For the simulations performed in the next section, $PFAC$=0,02 and $DAMP$=0,1 are used.

5.7.5. Number of Coupling Points

Except for a certain amount of numerical noise in the beginning of the simulation, the number of quadrature points does not have a major influence on the slamming force (see Fig. 53). The optimal configuration occurs for $NQUAD$=2, producing a fairly stable curve. The Lagrangian and Eulerian meshes have a similar size and two coupling points seem to be sufficient for this relative mesh resolution.

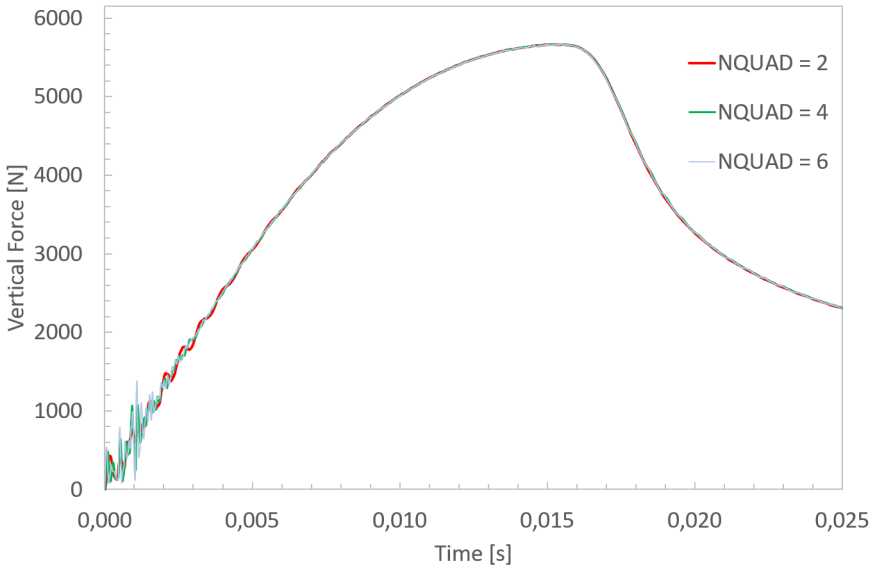

Figure 53: Influence of the number of coupling points in the slamming force.

By increasing the number of coupling points, the stiffness of the contact is consequently increased, which may lead to higher numerical instabilities.

5.7.6. Equation of State

The implemented Equations of State yield an overall similar result. However, the linear polynomial EOS is less stable. A significant oscillation occurs at around $t = 8ms$ (see Fig. 54).

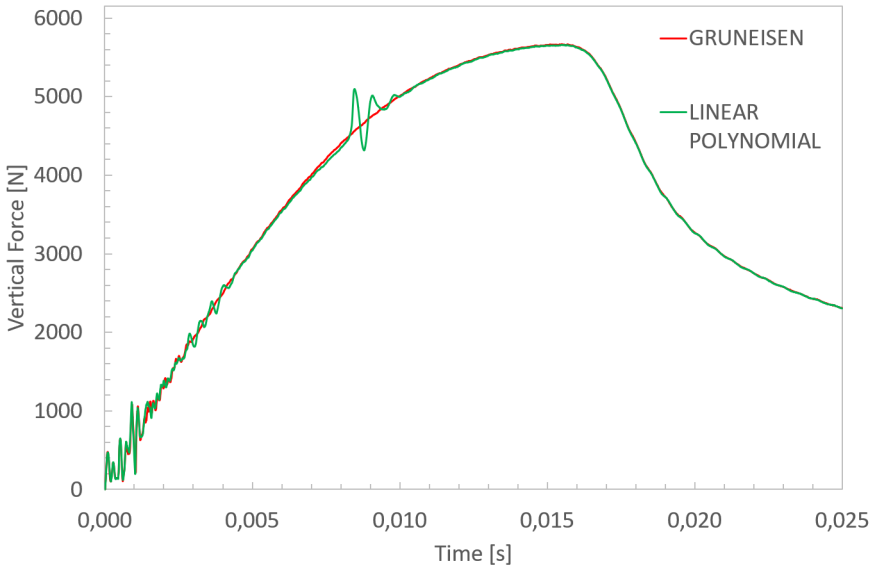

Figure 54: Comparison of the influence of the EOS in the slamming force.

Observing the pressure field at this specific instant (see Fig. 55), it is possible to see an abrupt shock-wave that begins in the middle of the fluid and expands towards the wedge, causing this oscillation on the impact load. This effect is likely not a physical behaviour and is probably associated to numerical errors caused by the polynomial approximation. In general, the linear polynomial EOS is indicated for linear deformations and might not be suitable for large deformations, as in this case.

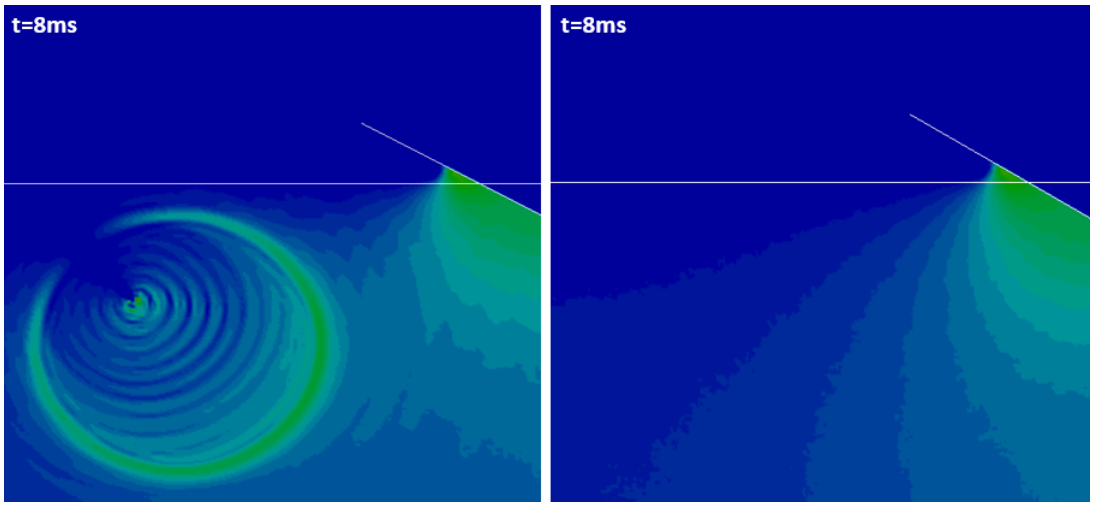

Figure 55: Pressure field observed for both EOS at $t = 8ms$. (Left: linear polynomial/Right: Gruneisen)

Since the Gruneisen EOS appears to be more stable in comparison with the linear polynomial EOS, it is used for the final model.

5.7.7. Geometry of the Fluid Domain

Results for the convergence of the vertical slamming force are presented in Fig. 56.

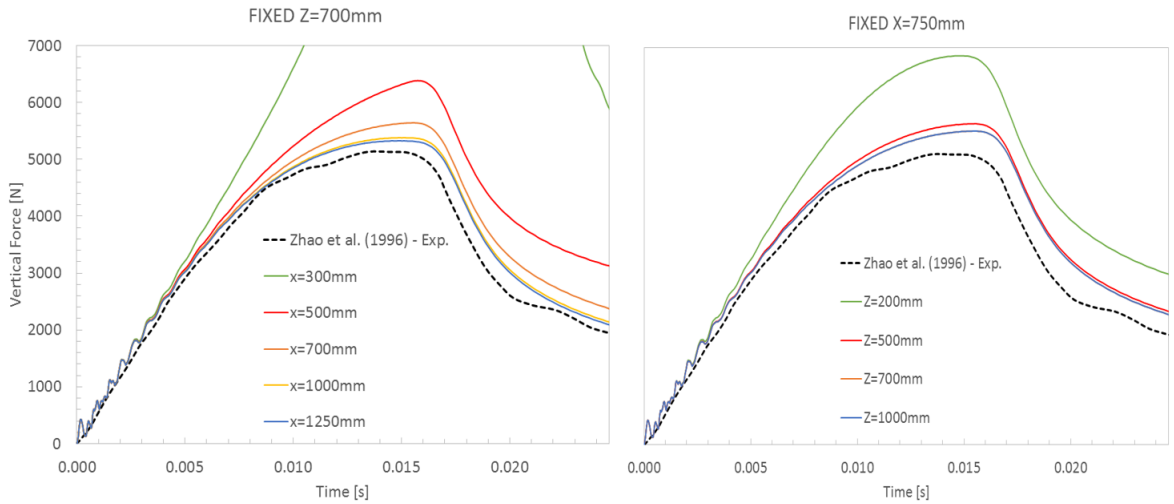

Figure 56: Slamming force for different dimensions of Z and X. Fixed $Z = 700mm$ and fixed $X = 750mm$.

For a constant $Z = 700mm$ it is possible to observe that as X is increased the slamming force approaches the experimental curve. The optimal value is $X = 1250mm$ resulting in a discrepancy of 4% in the maximum force, as already described in Sec. 5.7.2. Since values from $X = 1000mm$ and $X = 1250mm$ are very close, it can be assumed that convergence is reached at $X = 1250mm$.

For a fixed $X = 750mm$ the same behavior is observed: as Z is increased, the curve approaches the experimental result. However, in this case, convergence is reached for $Z = 700mm$. Increasing Z to $1000mm$ does not alter the profile and curves for $Z = 700mm$ and $Z = 1000mm$ match exactly. It is also noted that the red curve ($Z = 500mm$) corresponds to the geometry proposed by Yu et al. (2019) [84].

The slamming force seems to be more sensitive to the size of the horizontal dimension of the domain. This is likely associated to the development of the free surface. As the wedge enters the water, the fluid is piled-up on the structure and pushed horizontally against the borders of the domain. This interaction between the free-surface and the border influences the resulting pressure profile. So in order to mitigate this effect, a reasonable distance between the impacting structure and the edge of the domain is required. However, for the vertical dimension, the interaction of the pressure field with the border appears to be slightly less significant.

It is noted that the optimal geometry ($1250x700mm$) has dimensions X and Z approximately five times larger than the breadth and depth of the wedge ($250x144mm$). Even though other factors, such as the geometry of the impacting body, impact speed, mesh size and

FSI parameters also have an important influence on the results, this notion might be useful in an initial approach.

Another important factor is the computational time. The accuracy of the simulation depends on the size of the domains and, obviously, larger domains are more expensive in terms of computational cost. Computation time required for each of the geometries is presented in Table. 9.

Table 9: Computation time required for each geometry.

Fixed X			Fixed Z		
X [mm]	Z [mm]	CPU Time	X [mm]	Z [mm]	CPU Tme
300	700	24min	750	200	22min
500	700	37min	750	500	41min
700	700	52min	750	700	51min
1000	700	1h 12min	750	1000	1h 10min
1250	700	1h 20min	750	-	-

As observed in Table. 9, the impact of increasing the domain size does not have a critical importance on the cost of a 2D wedge simulation, since total calculation time is relatively low. However, this factor might be critical in 3D models, where computational cost might become very high.

In conclusion, the horizontal and vertical dimensions of the water domain have a significant influence on the slamming force. Setting up proper dimensions for models of slamming is, therefore, of important in both the accuracy and computational efficiency.

Further studies on the 2D wedge with a low deadrise angle and prescribed constant velocity are presented as additional material on Appendices

6. Case Study 2: 3D Rigid Wedge

A 3D model of the drop-test has been developed for a more realistic investigation on the phenomenon, since 3D effects might have significant influence on the slamming loads. Furthermore, the analysis of the stress-strain response of anisotropic materials in later stages of this work requires a three-dimensional setup, given the directional dependence of the results.

6.1. Model Setup

A higher number of finite elements is required for the 3D case and computational cost becomes significant. One of the measures taken to reduce computation time is modeling a quarter of the problem, taking advantage of its symmetry on the planes y-z and x-z (see Fig. 57). The fluid domain is extended in the Y direction so that the 3D flow close to the extremities of the wedge can be reproduced without influence of the boundaries. The wedge has 500mm Y direction and additional 300mm are kept empty.

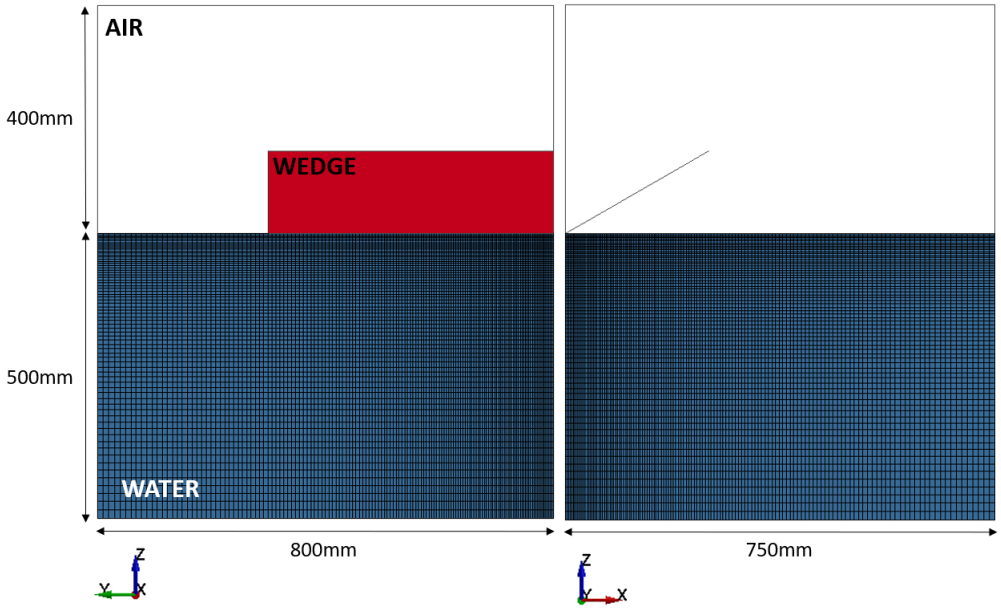

Figure 57: 3D model with refined mesh. Right and front views. The air domain is hidden for a better comprehension.

It is noted that in the 3D case, the influence of the transverse dimension of the fluid is expected to be less significant, since the domain is extended in the longitudinal direction. Therefore, in order to save computation time, the dimensions proposed by Yu et al. (2019) [84] are used.

Non-reflecting and axisymmetric boundary conditions are applied similarly to the 2D model. In addition, previously validated FSI settings ($PFAC$=0,002, $DAMP$=0,1 and $NQUAD$=2), material properties and Equations of State are implemented.

Regarding discretization, a minimum element size is defined based on the validated mesh used for the two-dimensional case ($2,5mm$). In this case, a non-uniform mesh is used in order to reduce computational costs. The mesh is refined only on the measurement area close to the symmetry axes of the model, gradually coarsening up to the extremities of the fluid domain. This approach decreases considerably the number of elements, whilst maintaining accuracy in the most relevant regions of the model. Details of the mesh are presented in Table 10.

Table 10: Details of the applied mesh.

Min. elem. size (mm)	2,5
Max. elem. size (mm)	15
Number of Elements	2637272
CPU Time	15h 15min

The total CPU time running in a 64GB 2,2GHz workstation with 8 cores is around 15 hours. Additionally, it is noted that the geometry and the meshing of the model were done in the software PATRAN, which offers better pre-processing tools more capable of handling sizable meshes.

6.2. Results and Discussion

6.2.1. Overall Behaviour

Figure 58 presents the evolution of the free-surface as the wedge enters the water. The transverse section view shows the same predicted behaviour obtained in the 2D model, with the expected pile-up effect and water jet. It is possible to observe in the longitudinal view, the rise of the water level on the left end of the wedge. Lower slamming loads are expected due to the unconstrained flow at this region, which is not reproduced in the 2D simulation.

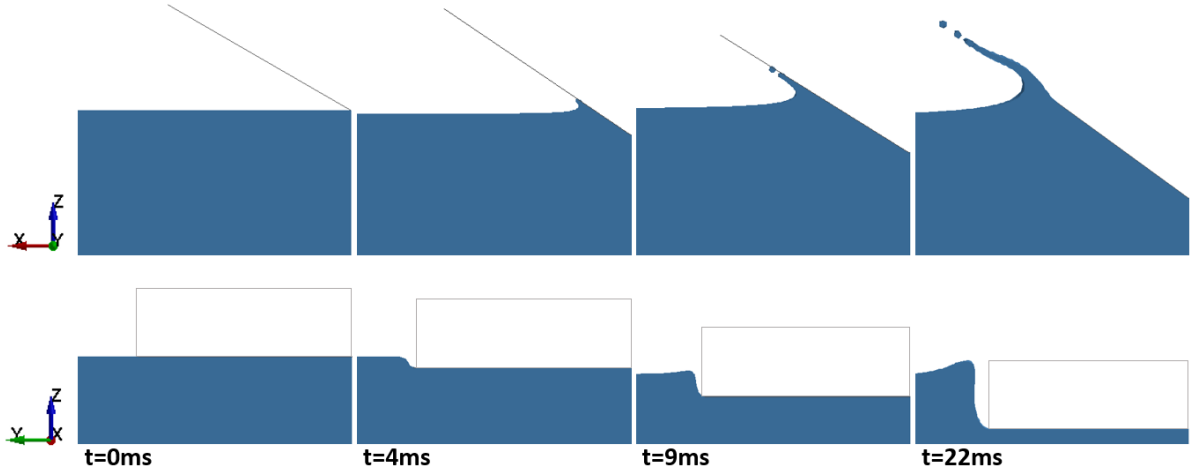

Figure 58: Free surface profile. (Upper: transv. view; lower: long. view.)

The pressure distribution on the wedge on the transverse view (Fig. 59) corresponds to the 2D model prediction, with an abrupt peak on the pile-up region. On the longitudinal section, the pressure distribution is fairly constant along the keel.

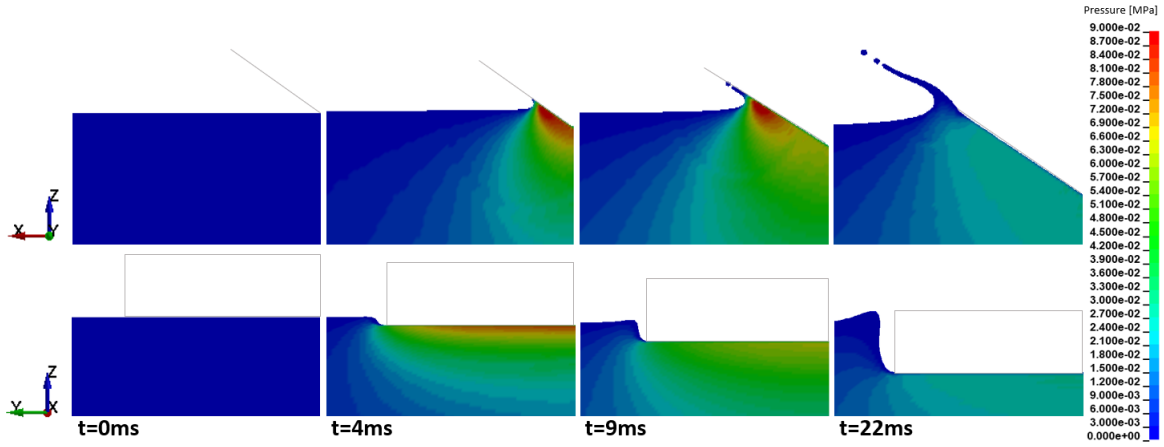

Figure 59: Pressure distribution. (Upper: transv. view; lower: long. view.)

6.2.2. Slamming Force

The predicted slamming force history is in fairly good agreement with the experimental results by Zhao et al. (1996) [72], as verified from Fig. 60. A peak force of $5236N$ is obtained, an overestimation of 2% of the experimental value.

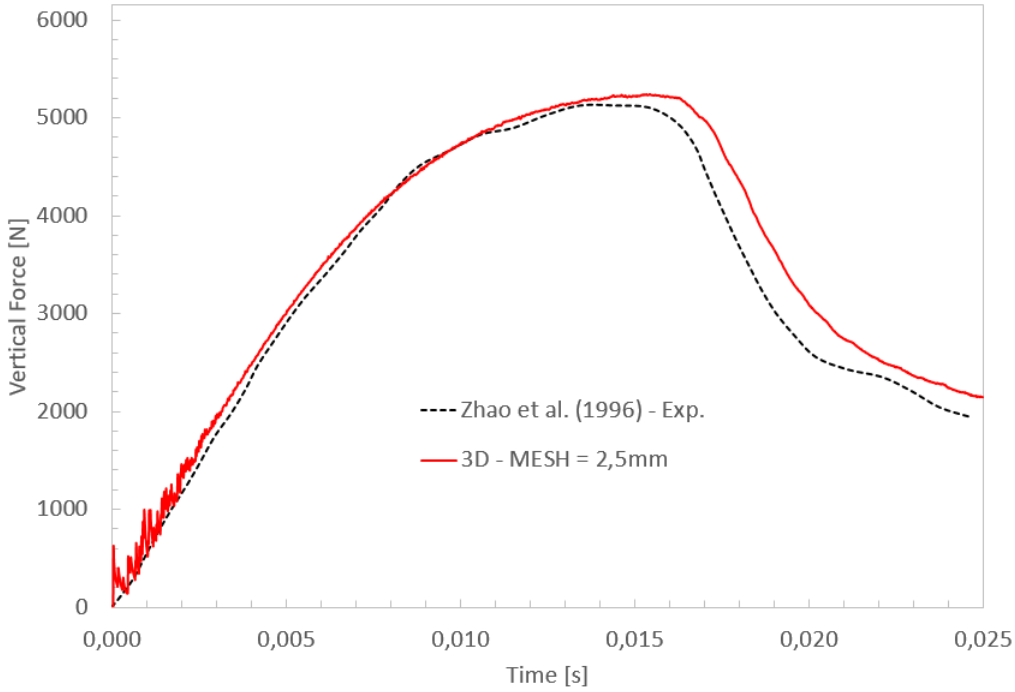

Figure 60: Comparison of the results for the slamming force for the 3D case.

Some numerical instability is observed in the beginning. It is also noted that the simulation approximates better before the peak, whereas after around $t = 15ms$ it shifts slightly forward. The discrepancy is likely related to the calibration of the FSI algorithm and does not represent a major issue. Overall, the prediction is fairly accurate.

7. Case Study 3: 2D Elastic Flat Plate

In this section, the objective is to validate a numerical model capable of predicting accurately the hydro-elastic behaviour of a horizontal plate subjected to slamming loads with a comparison with the experiment proposed by Faltinsen et al. (1997) [49]. The simulation developed in LS-DYNA combines an elasto-plastic material and previously assessed FSI configurations adapted to a flat horizontal plate. The numerical model developed in Yu et al. (2019) [84] is used as reference for the setup.

7.1. Experimental Setup

Faltinsen et al. (1997) [49] proposes theoretical methods for the prediction of slamming-induced loads in the wet-deck of a multihull vessel and performs a series of experimental drop-tests of horizontal plates to validate the formulations.

A drop rig similar to the one applied in the wedge drop-test by Zhao et al. (1996) [72] is used. The tested plate has a length of $1000mm$ and a breadth of $500mm$ with a $100mm$ measurement section in the middle. It is $8mm$ thick, made of high-strength steel. Measurements are performed with the use of strain gauges, pressure and force transducers and accelerometers placed strategically in the assembly. The complete drop rig weights $500kg$. Main dimensions of the rig and configuration of the sensors are shown in Fig. 61.

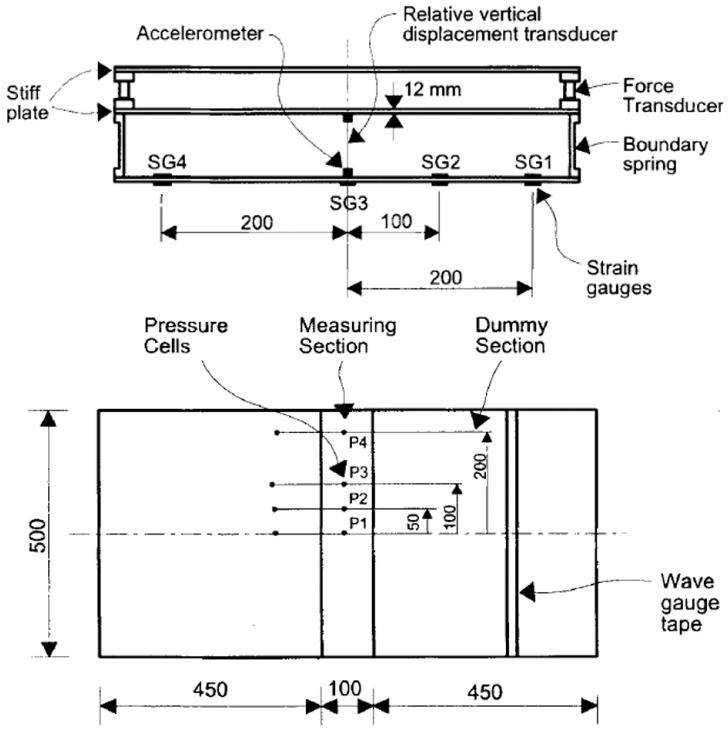

Figure 61: General dimensions of the test plate and configuration of sensors. (From: Faltinsen et al., 1997 [49]).

The test plate is connected to a rigid assembly with rotational springs at the edges. The springs allow the test plate to deflect a certain amount, while the relative translation between the rigid assembly and the plate on the fixing points is restrained. This configuration reproduces the behaviour of a typical wet-deck structure subjected to slamming. However, it is critical to define a proper rotational stiffness in order to reproduce accurately the expected behaviour. A rotational stiffness (k_θ) of $102144 Nm/(rad.m)$ is used.

7.2. Model Geometry and Boundary Conditions

A two-dimensional setup similar to the one previously developed for the rigid wedge is used in this study (Fig. 62). Half of the drop-test model is prepared, taking advantage of the axisymmetry of the problem. The fluid domain is divided into air and water with dimensions based on the study by Yu et al. (2019) [84]. The complete model has a longitudinal thickness of $t = 10mm$.

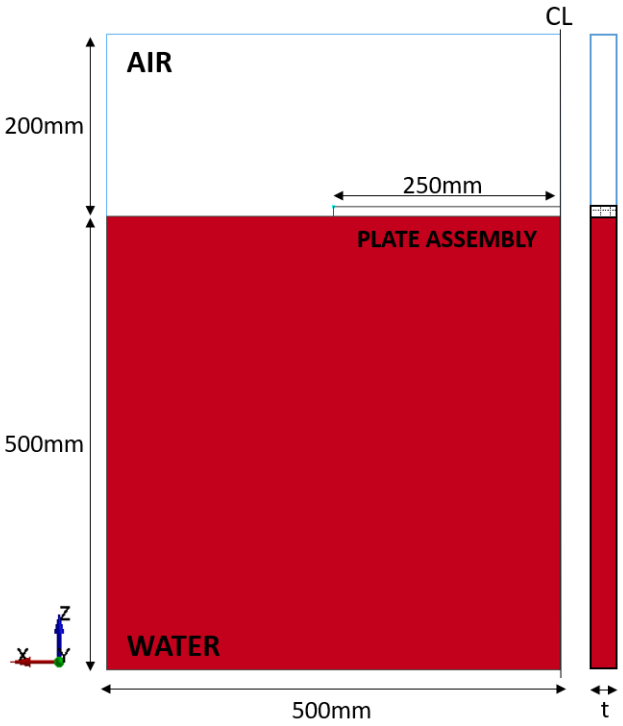

Figure 62: Model setup of the horizontal plate. Dimension t is defined by the minimum mesh element size.

Nodes on the right edge of the fluid domain are constrained in X direction, all the nodes are constrained in Y direction and non-reflecting boundaries are applied in the top, left and bottom edges of the model. Additionally, the nodes of the plate assembly located at the symmetry axis are constrained in X direction. Rotational degrees of freedom in X and Z are constrained to all nodes.

The plate assembly, shown in Fig. 63, is composed of a rigid plate, a connecting spring and an elastic plate. It is placed on the surface of the water with an initial velocity of

$3,030 m/s$, reproducing the instantaneous state of the assembly in the experiment right before impact.

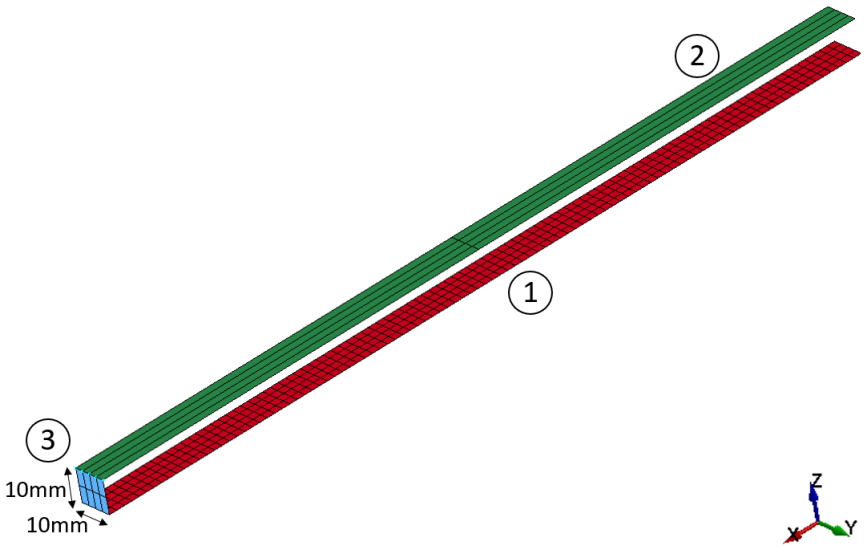

Figure 63: Numerical model of the drop assembly. Elastic plate (1), rigid plate (2) and spring (3).

The card ELEMENT_MASS is used to define the mass of the drop rig, which is calculated proportionally to the simulation section and is applied as lumped masses on the leftmost nodes of the rigid plate.

It is important to note that the three parts of the drop assembly are composed of shell elements. In the case of the connecting spring and the rigid plate, very small thicknesses are defined so the weight of the parts are negligible compared to total weight applied with ELEMENT_MASS.

7.3. Material Properties and Equations of State

Material properties for the fluids are set with the card MAT_NULL, while the rigid plate is defined with MAT_RIGID. Used parameters are described in Sec. 5.3. For the elasto-plastic plate, MAT_PLASTIC_KINEMATIC is used with the properties given in Table 11.

Table 11: Properties for HSLA steel plate used in the experiment.

Density (kg/m^3)	7850
Yield Strenth (MPa)	355
Young's Modulus (GPa)	210
Poisson's Coefficient	0,33
Tangent Modulus (MPa)	400

A MAT_ELASTIC card defines the spring. It must be carefully calibrated to reproduce the expected behaviour of the plate, as previously mentioned. The required stiffness is obtained by inputting a corresponding Young's modulus to the material; which is calculated with Eq. 43, where I is the section moment of inertia, L is the length of the spring and E is the Young's modulus.

$$k_\theta = \frac{4EI}{L} \tag{43}$$

For a rectangular section with $10mm$x$10mm$ and $L = 10mm$, $E = 3065MPa$.

Finally, EOS Gruneisen with parameters from Table 3 in Sec. 5.3 are used for both water and air, since good results were obtained for the rigid wedge.

7.4. Selection of Mesh

A uniform mesh with an element size of $2,5mm$ is used in the complete model. This mesh yields a good compromise between accuracy and computational cost as validated by Yu et al. (2019) [84]. The Eulerian parts are composed of solid elements and the Lagrangian structure is composed of shell elements, as explained before. The chosen element formulation for the shells is Belytschko-Tsay with 6 integration points through the thickness. Details are summarized in Table 12.

Table 12: Details of the applied mesh.

Elem. size (mm)	2,5
Number of Elements	224416
CPU Time	3h 40min

The simulation runs in around 3 hours and 40 minutes in a 16GB 3,0GHz workstation.

7.5. FSI Settings

Regarding the setting of the fluid-structure interaction algorithm, main parameters are defined as in Yu et al. (2019) [84], where LS-DYNA's default configuration is used (Table 13).

Table 13: FSI parameters used in the model.

PFAC	DAMP	NQUAD
0,1	0,0	2

Although Aquelet (2004) [58] proposes a penalty factor for a horizontal plate (Table 6), the value results in non-convergence when applied to the current model. Therefore, it

seemed more reasonable to follow the configuration by Yu et al. (2019) [84], since good results were obtained and geometries and meshes are essentially the same in both models.

Furthermore, the ALE control settings are defined with the default advection method.

7.6. Results and Discussion

7.6.1. Fluid Behaviour

The simulation reproduces well the expected behaviour of the free-surface upon impact, as observed in Fig. 64. The plate assembly gradually enters the surface and a water jet forms on the left edge, growing away from the structure.

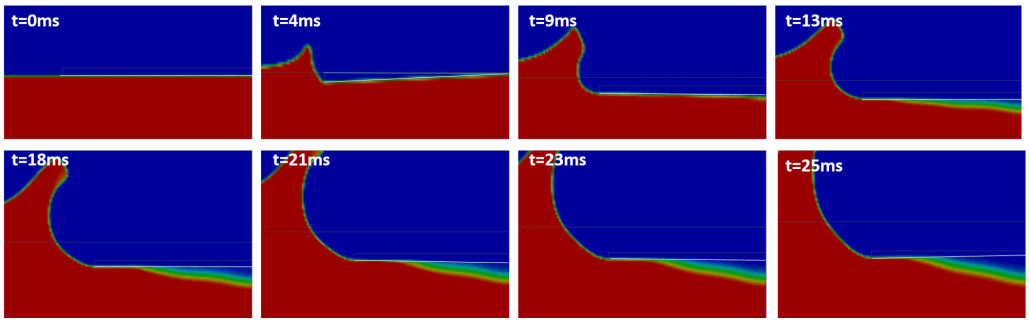

Figure 64: Development of the free-surface with the plate entry.

Air entrapment can be observed in the middle of the plate, represented by a blue (air) and green (multi-material transition) gap between the plate and the free-surface. This phenomenon, also referred as air cushioning, usually occurs for impact angles smaller than 5°. It is caused by air forced in between the plate and the free-surface at initial stages of the impact (ventilaton) and vapour created by cavitation in the region. This pocket of air and vapour significantly reduces impact pressures and produces quasi-uniform pressure distributions along the plate (Okada and Sumi, 2000 [74]).

This effect is better observed when a high negative cut-off pressure is set for the water domain. In this case, the vapour pressure is not reached and cavitation is avoided (see Fig. 65). As expected, there is no ventilation, since the plate is initially placed exactly on the water surface, impeding any air from accessing the region in between, as would occur in a free-fall with an initial height.

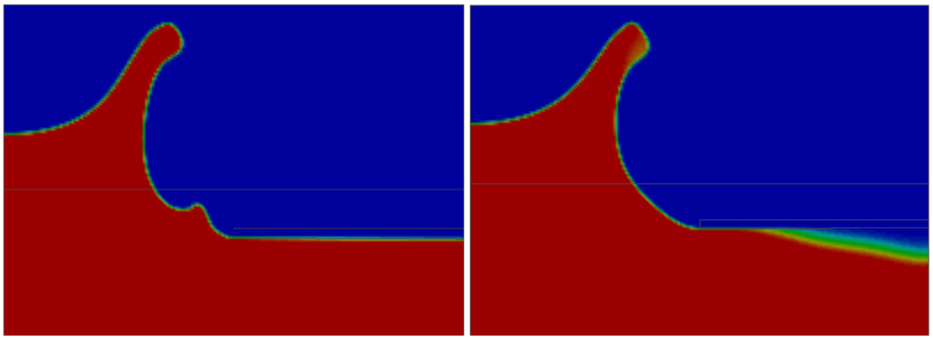

Figure 65: Comparison of the surface without (left) and with (right) cavitation. The formation of an air-pocket associated to the cavitation is seen on the right ($t = 24ms$).

7.6.2. Slamming Pressure

Figure 66 shows the average pressure distribution on the plate over time. As expected, in the first instants of the impact a shock wave is produced (see Fig. 67) and generates a highly accentuated and localized pressure peak. The maximum pressure reaches around $10MPa$, but this value is not accurate due to numerical issues which will be further discussed. For better visualization of the pressure profile, the absolute maxima are not shown in the diagram. The pressure decreases and remains more or less constant for the rest of the entry. Negative values are captured in the simulation where a cut-off pressure higher than the water pressure vapour is defined.

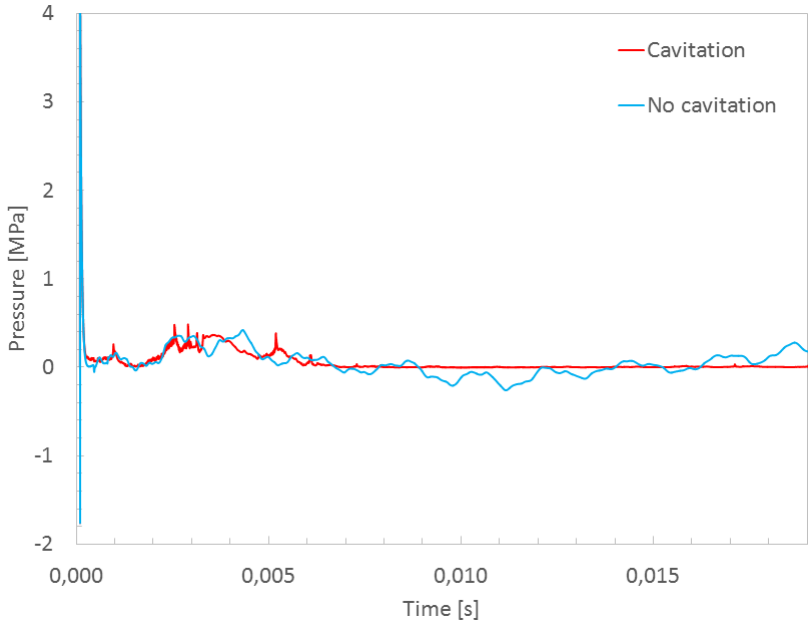

Figure 66: Average pressure distribution on the plate over time with and without cavitation. Negative pressures are registered for the model with no cavitation.

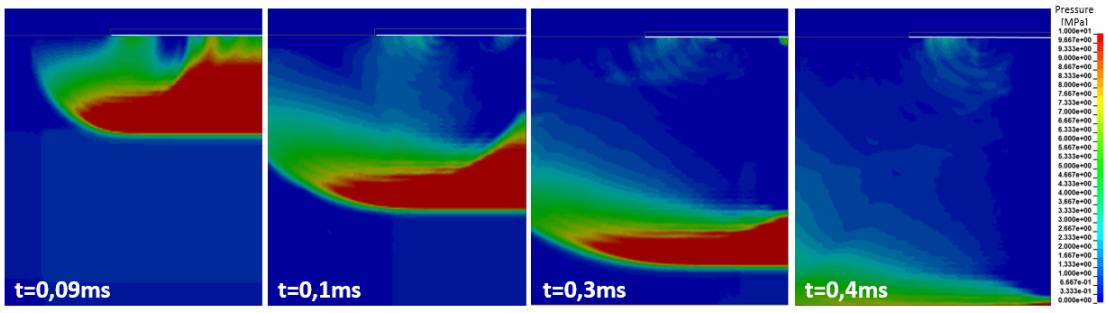

Figure 67: Pressure distribution over the first instant of the impact. The shock wave propagation can be observed.

The local pressures measured at the middle of the plate and at $100mm$ away from the midpoint are presented in Fig. 68. Highly accentuated peak pressures characteristic of flat-plate slamming are observed on both experimental and numerical results. Even though

the simulation produces a good distribution in terms of shape, the magnitudes are not well captured. Values estimated numerically are more than ten times higher the maximum experimental pressures.

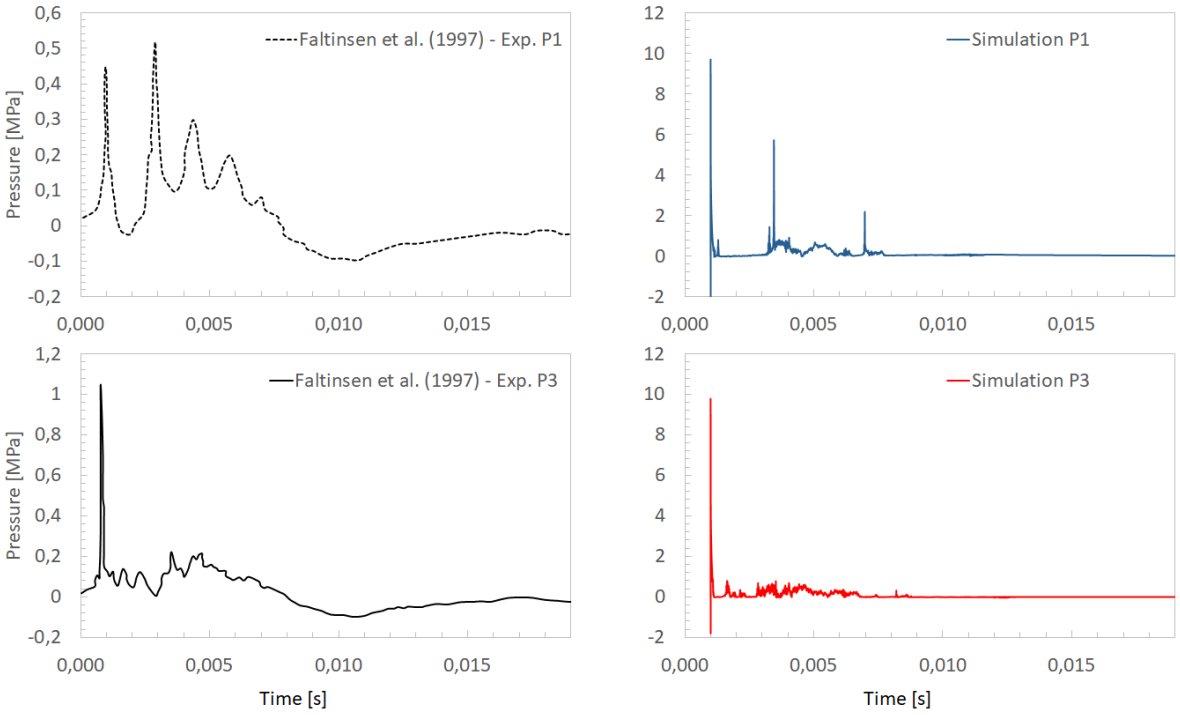

Figure 68: Comparison of obtained local pressure over time measured on mid-plate (P1) and $100mm$ from mid-plate (P3). Left: Experimental results from Faltinsen et al. (1997) [49]; right: numerical results.

It proved very difficult to correctly obtain the local pressure distributions in *LS-DYNA*. This may be associated to the way the pressures are calculated within the numerical algorithm. By applying sensors on the elements of a small region and assessing the average pressure on the local instead of measuring on a single element, the quality of results improved slightly. However, the magnitudes were still far from the expected.

Furthermore, according to Faltinsen et al. (1997) [49], the measurements of peak pressures during wetdeck slamming do not provide useful information about maximum stresses on the plate. The peak pressures are highly concentrated in time and space and were difficult to be accurately measured on the experiment. External conditions have great influence on the pressure distribution, which resulted in considerable dispersion of the experimental results (see Fig. 10).

And finally, when the peak pressures are very sharp compared to the natural period of the structure, as in this case, the response is mainly governed by the pressure impulse. Pressure magnitudes will have a negligible effect on the structure. The impulse is related to the momentum of the plate and can be estimated by integrating the pressure distribution

curve, which is a better way to estimate the maximum structural response (Yu Z., personal communication, September 28, 1998).

7.6.3. Hydro-elastic Behaviour of the Plate

A comparison of numerical and experimental results for the deflection over time measured on the middle of the plate is presented in Fig. 69.

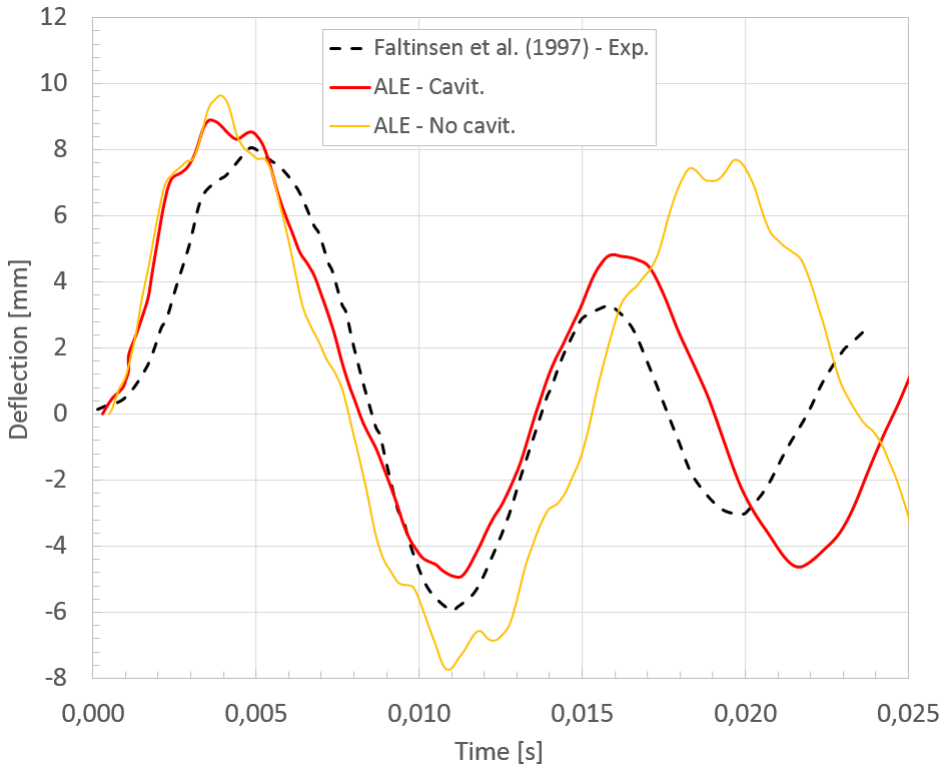

Figure 69: Comparison of the deflection registered on the middle of the plate.

The maximum deflection and oscillation period are in good agreement during the first oscillation. However, it is possible to observe a significant difference for the second oscillation period. According to Faltinsen et al. (1997) [49], the reduction of the oscillation period on the experiment is most likely related to the occurrence of air cushioning. Even though cavitation is generated in the numerical model, there is no coupling between the air domain and the Lagrangian structure, and the effect of air cushioning is not completely reproduced. For the case where no cavitation is present, it is possible to observe that the oscillation period remains fairly constant. Further models will take into account the cavitation.

In Fig. 70 the deflection velocity post-processed at the middle of the plate is compared to Faltinsen's experimental results. Although high levels of numerical fluctuations are present, results appear to be fairly well matched up to the first oscillation period. Similarly

to the results obtained for the deflection, a phase lag appears from around $15ms$ due to the same effects explained before.

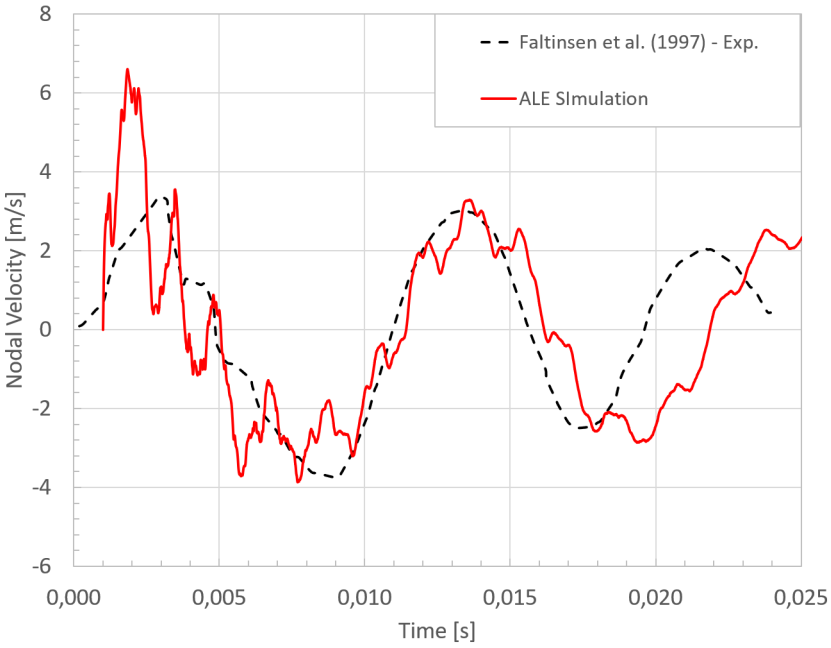

Figure 70: Comparison of the nodal velocity registered a the middle of the plate.

Regarding the fluctuations on the curve, Faltinsen et al. (1997) [49] explains that the first and second symmetric vibration modes combine in the analyzed impact response, which results in this complex wave and becomes evident in particular for the numerical model. However, some numerical noise is likely also present and increasing damping might improve results.

Overall, the model works well and is validated to be applied in other hydro-elastic slamming simulations.

8. Case Study 4: FRC Sonar Dome

Case Study 4 is proposed by the company Calcul-Méca. The numerical models presented in Sections 5, 6 and 7 are used as basis for the development of a slamming simulation for the fiber reinforced composite sonar dome shown in Fig. 71.

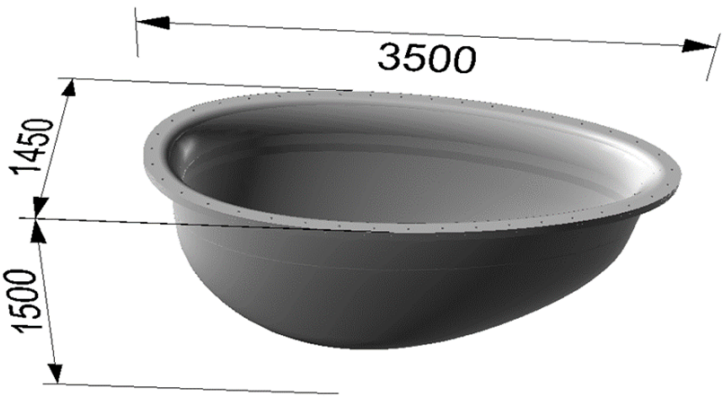

Figure 71: CAD model of the presented sonar dome.

The main goals are to assess the slamming loads and structural response of the component. Additionally, the Tsai-Wu failure criteria is observed. Results for the structural response will be compared against a quasi-static FE model developed by the company. This comparative model uses a pressure profile estimated with the Original Logvinovich analytical formulation (Logvinovich, 1969 [81]).

Preliminarily, a two-dimensional version is developed for a quicker and more practical overview of the problem and for the initial calibration of the contact algorithm. Once reasonable results are obtained, the configuration can be extended to a more costly 3D case.

It is noted that even though the final objective of this study was the development of the 3D slamming model for the composite sonar dome, issues associated to the limitations of the ALE method were encountered in the preliminary phase. The 3D model was not implemented since no conclusive results were found during the available time for the project. This matter will be further discussed.

In the next sections, the problem statement, the preliminary calibration and troubleshooting process is presented. These developments can be used as reference for further work.

8.1. Model Geometry and Boundary Conditions

In order to simplify the 3D model, the geometry of the sonar dome is approximated to an elliptical paraboloid, as illustrated in Fig. 72. This simplified shape is symmetric on

planes x-y and x-z, and can be modeled simply as a quarter of the full geometry, which allows for a significant reduction in computational cost.

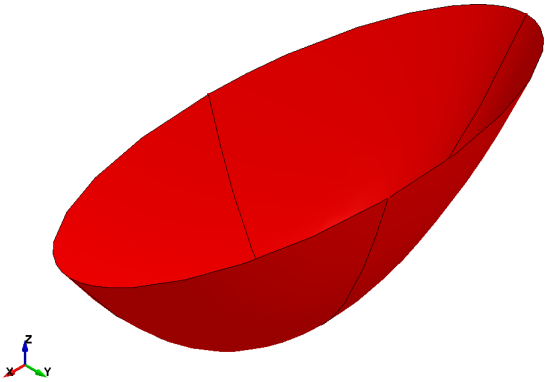

Figure 72: Sonar dome approximation with an elliptical paraboloid.

The general dimensions of the paraboloid are given in Fig. 73.

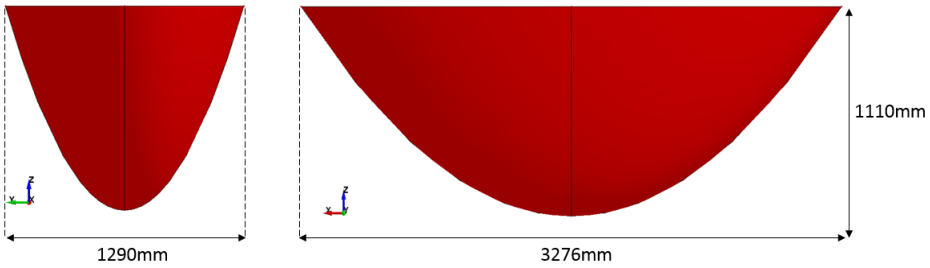

Figure 73: General dimensions of the elliptical paraboloid.

The preliminary 2D model is presented in Fig. 74.

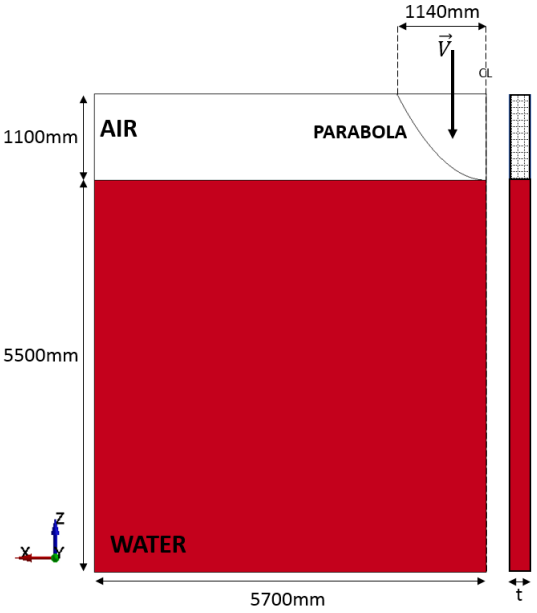

Figure 74: Two-dimensional model of the sonar dome. t is the minimum mesh size.

The size of the fluid domains is chosen according to the notions obtained in the sensitivity study performed in Sec. 5.7.7. The dimensions of the 2D parabola were provide by the company, where the height is the same as the 3D geometry and the breadth is roughly an average of the major and minor breadths of the elliptical paraboloid.

Boundary conditions are defined similarly to the previous models for the wedge and the plate (Sections 5.2 and 7.2). However, in this case, there is no previous knowledge of the masses involved in the impact. Therefore, instead of a free-fall with initial velocity and applied mass, as for the wedge and the plate models, a constant velocity $V = 10m/s$ is imposed on the sonar dome (parabola).

8.2. Material Properties and Equations of State

For both the fluids, material properties and EOS are described in Sec. 5.3. For the sonar dome, the composite laminate is modeled with *LS-DYNA* material MAT054 (Material Enhanced Composite Damage). The laminate has a total thickness of approximately $20mm$, with 32 plies of unidirectional E-glass fiber/epoxy alternating 0° and 90° directions. The main characteristics of the laminate are summarized in Table 14.

Table 14: Composite material of the sonar dome.

Type	Unidirectional
Matrix	Epoxy
Fiber	E-Glass Fiber
Stack-up Sequence	$[0°; 90°]_{32}$
Thickness	19,98 mm

Detailed properties for the matrix, fiber, ply and laminate are provided in Tables 17, 18, 19, 20 and 21 in Appendix C.

The configuration of the *LS-DYNA* card MAT054 is shown in Fig. 75.

```
*MAT_ENHANCED_COMPOSITE_DAMAGE
$      MID        RO         EA         EB         EC       PRBA       PRCA       PRCB
         1 1.7790E-9      33974       9286       9286      0.082      0.082      0.409
$      GAB        GBC        GCA         KF       AOPT       2way         ti
      2779       3295       2779                    2
$#                                        A1         A2         A3
                                         1.0        0.0        0.0
$       V1         V2         V3         D1         D2         D3     DFAILM     DFAILS
                                         0.0        0.0        0.0      0.000      0.000
$    TFAIL       ALPH       SOFT       FBRT      YCFAC     DFAILT     DFAILC        EFS
                                          1                 0.0000     0.0000
$       XC         XT         YC         YT         SC       CRIT       BETA
      579        892       95.1       55.9       32.2         55
```

Figure 75: Configuration of the *LS-DYNA* card MAT054.

Main assumptions for the composite material are:

- Intra-laminar degradation is the only energy dissipation mechanism considered.
- The Maximum Stress criterion governs the fiber rupture, BETA=0.
- Strain failure criteria is not used (DFAIL). That means no element deletion occurs.
- Softening reduction factor in the crash front is not considered.
- Time step criterion for element deletion is not used.
- Softening for fiber tensile or compressive strength after matrix compression failure (FBRT or YFAC) is not used.
- Effective failure strain (EFS) for element deletion is not used.

Additionally, simulations using the rigid and isotropic elasto-plastic materials described in Sections 5.3 and 7.3 are also performed for comparison.

8.3. Selection of Mesh

Preliminary simulations with the 2D sonar dome are performed with $20mm$ and $10mm$ uniform meshes for a more practical overview of the functioning of the model and calibration of contact parameters. The Eulerian parts are composed of solid elements and the Lagrangian structure is composed of shell elements. For the final 2D model, a minimum element size of $2,5mm$ is used in a structured mesh (see Fig. 76). Details are summarized in Table 17.

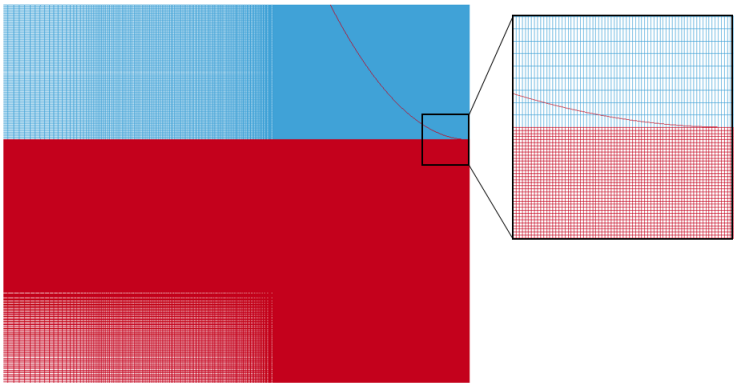

Figure 76: Detail of the $2,5mm$ structured mesh used in the final 2D model. The mesh is refined close to the impact region on the parabola/fluid interface.

Table 15: Details of the used meshes for the 2D model.

Min. Element Size [mm]	20	10	2,5	2,5 (Comp.)
Number of Elements	94133	350664	615729	615729
CPU Time	47min	3h 27min	86h 36min	126h 39min

CPU times shown refer to the simulations with the elastic isotropic material, except for the last one on the right, which refers to the model with the composite material implemented. A 32GB 3,7GHz workstation with 4 cores is used.

8.4. FSI Settings

Initial FSI configurations are summarized in Table 16. Parameters are further calibrated depending on the obtained fluid-structure interaction.

Table 16: FSI parameters used in the model.

PFAC	DAMP	NQUAD
0,1	0,5	2

8.5. Results and Discussion

Simulations with the presented 2D sonar dome are firstly performed on a full scale model. On the second stage, in order to test a more refined mesh whilst maintaining a practical computation time, a scaled version is developed.

8.5.1. Full Scale 2D Model

Results presented in this section refer to the full scale 2D parabola model performed with $20mm$ and $10mm$ meshes. Figure 77 shows the free surface behavior with a rigid parabola.

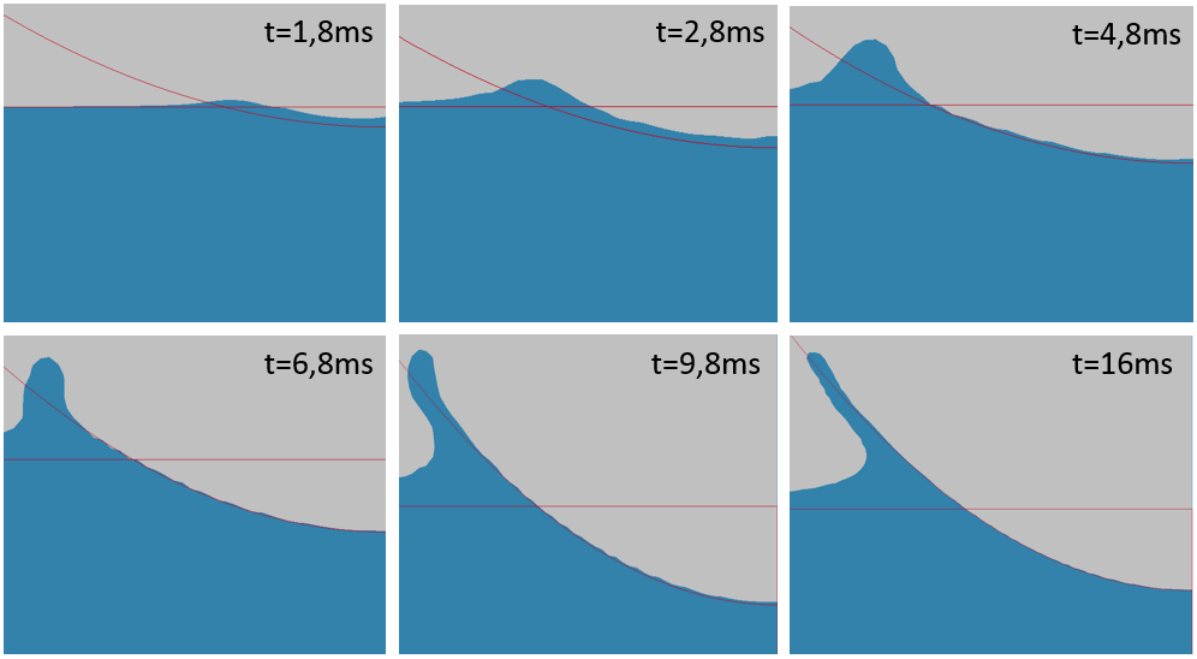

Figure 77: Development of the free surface for the water entry of a rigid parabola.

Severe leakage can be observed on the Lagrangian structure, specially on the fluid pile-up region, where expected pressures are higher. It starts on the very beginning of the impact and stabilizes closer to the end, as pressure gradients decrease.

The leakage is likely associated to the high imposed constant velocity ($V = 10m/s$) combined with the low deadrise angle of the parabola, resulting in large contact forces. In order to mitigate this issue, the contact algorithm is recalibrated by increasing the penalty factor until almost no fluid penetration is observed. Other strategies, such as increasing the number of coupling points and enabling the leakage control parameter ILEAK (described in *LS-DYNA* Keyword User's Manual [44]) are also used.

However, fluid leakage is only reasonably reduced with an extremely high penalty factor ($PFAC=9$), which leads to another issue: numerical instability. The vertical slamming force over time is shown in Fig. 78.

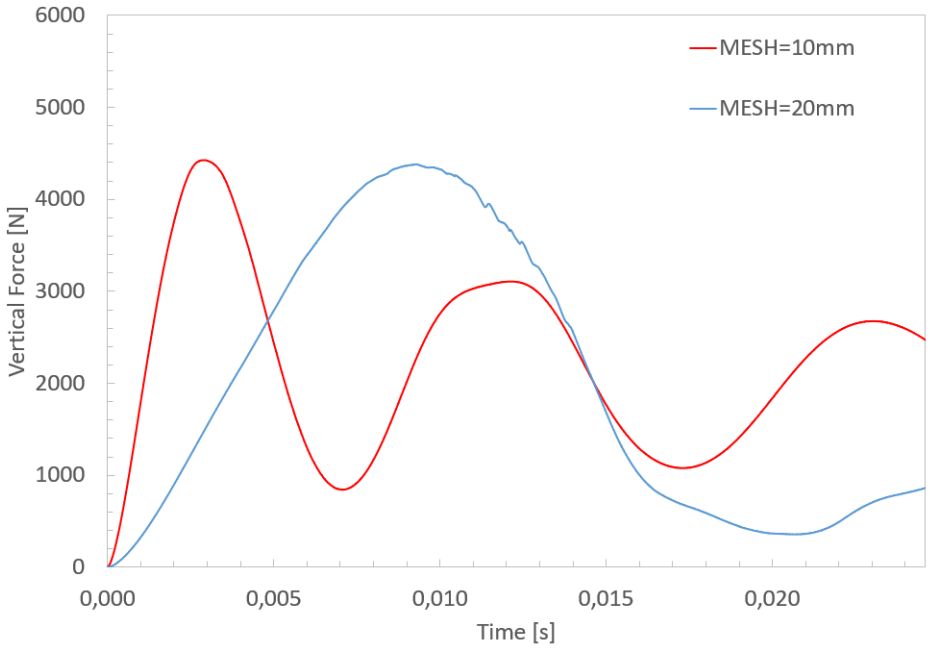

Figure 78: Vertical slamming force obtained for the parabola. Two different mesh sizes were applied.

For the $20mm$ mesh, the peak force is reached at around $9ms$, gradually decreasing until almost zero. It then starts to rise again at around $20ms$. For the $10mm$ mesh, a similar oscillating behavior is observed, but with a higher frequency. It is also noted that the amplitude seems to decrease over time.

A certain amount of high frequency oscillations associated to the virtual contact springs is expected. However, in the current simulation, for both mesh sizes, the vertical force oscillates with a low frequency and drops unexpectedly to almost zero. This indicates that the mesh is not refined enough to capture the actual physical behavior of the fluid-structure interaction. The solution to improve convergence and decrease the need for a high penalty factor is, therefore, applying smaller size elements.

Since the $2,5mm$ structured mesh (see Fig. 76) is very costly for this preliminary stage of the analysis, a scaled version is prepared. This smaller model enables the use of a finer mesh while maintaining practicality in terms of computation time. Results are presented in the following section.

Additionally, results for the full size 2D flexible parabola are presented in Appendix D. These results are not conclusive and, therefore, are not presented in the main part of this report.

8.5.2. Scaled 2D Model

The scaled version of the model is presented in Fig. 79. This version allows a quicker and more practical way of observing the behavior of the parabola under slamming and calibrating the contact algorithm. The minimum mesh size is $2,5mm$.

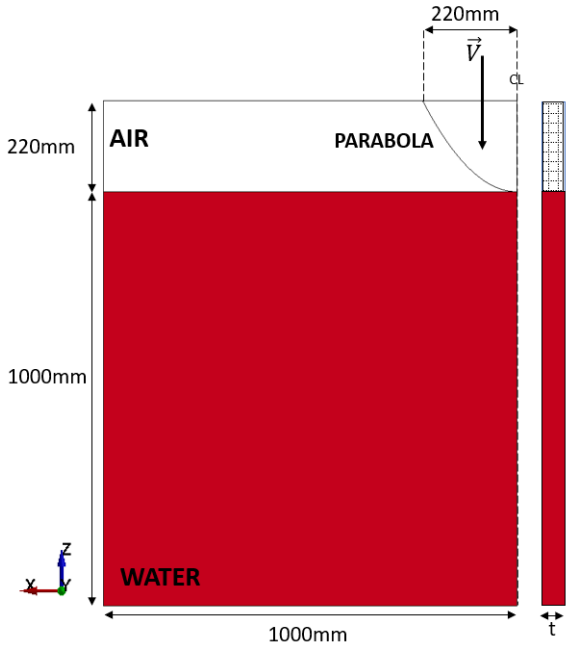

Figure 79: Two-dimensional scaled model of the sonar dome. Minimum mesh size $t = 2,5mm$.

Even with a finer mesh, difficulties were encountered to control the leakage problem with a velocity $V = 10m/s$. A $PFAC = 2$ was required to prevent reasonably the issue.

The influence of the structure velocity on the slamming vertical force over time for different constant velocities is shown in Fig. 80.

The same non-physical oscillating behaviour is observed, even though the penalty factor could be decreased for lower velocities. Amplitude and oscillation frequency increase with higher velocities. The orange curve for $V = 3m/s$ is not complete, because the simulation was terminated prematurely. However, a similar profile can be expected.

Results for the full size and the scaled parabola are not coherent and decreasing the impact velocity does not yield improvements. This might indicate that the issue is related to the application of an imposed constant velocity, instead of the initial velocity and mass configuration used on the wedge and plate models. Moreover, further refining the mesh could help improve results.

Given the presented complications with the current model, it was not considered reasonable to proceed with the 3D sonar dome simulation. Further analysis on the effectiveness and accuracy of the ALE method and the penalty contact algorithm is required for this specific

geometry. This was not possible on the time-frame of this project. Suggestions for future developments on the subject are presented in Sec.10.

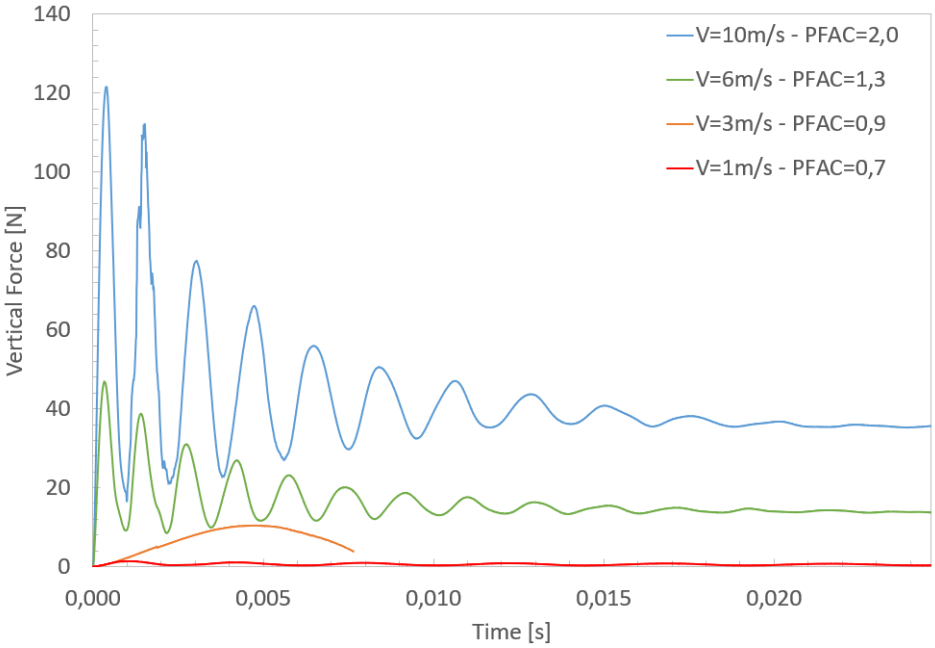

Figure 80: Vertical slamming force obtained for the scaled parabola with different imposed constant velocities.

9. Conclusion

Models for slamming on wedges and flat horizontal plates have been developed in this study with the use of ALE algorithm on *LS-DYNA*. The idea is to prepare basic models that could be validated by comparison with experimental results present in the literature. These models will be further applied to more complex marine structures and materials.

One of the main difficulties in modelling fluid-structure interaction is calibrating the contact algorithm. In this case, the penalty factor method is used with *LS-DYNA's* contact card CONSTRAINED_LAGRANGE_IN_SOLID.

As a first approach, a 2D model of a wedge slamming is developed and compared against experimental results from Zhao et al. (1996) [72]. The focus is on adjusting properly the FSI parameters, mainly the penalty factor, damping coefficient and number of coupling points. Several tests are performed with different combinations of parameters. The influence of the Equations of State and the geometry of fluid domains is also observed. Overall, results are good. An overestimation of 9% is observed for the slamming force, which can be explained by the fact that the two-dimensional model does not represents 3D flow effects. The resulting free-surface behaviour and overall pressure distribution are well reproduced.

The second stage is the development of a three-dimensional model of the wedge experiment. The objective is to assess the influence of the 3D flow effects on the slamming force and prepare a model capable of reproducing realistically the directional dependent structural response of composite material. Results for the slamming force, free-surface behaviour and pressure distribution are in very good agreement with experimental results.

Third, the drop-test of a flat deformable plate performed by Faltinsen et al. (1997) [49] is simulated with a similar 2D model. The goal is to assess the suitability of the model to elasto-plastic materials. Good results are obtained for the elastic behaviour of the plate in terms of deflection over time. But measuring local pressures proved very difficult in *LS-DYNA* and important discrepancies between numerical and experimental results are observed. However, it is worth to note that, according to the author, local pressures measured by Faltinsen et al. (1997) [49] are questionable, as large variations in peak levels have been documented.

Lastly, a slamming model for a fiber reinforced composite sonar dome is proposed. The first approach is to perform the calibration of the contact algorithm in a simplified two-dimensional rigid body version before implementing the three-dimensional composite material model. However, severe fluid leakage is observed in the structure and an unexpected behavior is obtained for the vertical slamming force. An oscillatory profile that does not appear to be physically coherent is found. This result is likely associated to the low deadrise angle of the parabola combined with the high imposed constant impact

velocity, a specific configuration that leads to high tangential fluid velocities. The penalty contact algorithm is ineffective for this situation and a kinematic contact method would probably work better.

In an attempt to correct the issue within a practical computational cost for this preliminary stage, a refined mesh is implemented in a scaled version of the 2D sonar dome. Nonetheless, the same behavior is encountered even for lower impact velocities. Conclusive results were not found and the implementation of the final 3D model with composite materials was not possible.

Overall, the study yields a reasonable outcome. A detailed investigation of the implementation of *LS-DYNA* to slamming is done. Models here developed are validated and can be applied to further studies in which the deadrise angle is not too small.

10. Further Work

Possible future developments on the subjects presented in the current work are suggested:

- Sensitivity study on the mesh size and parameters of the penalty contact algorithm for the 2D parabola in order to confirm the limitations of the contact method under the specific conditions presented.
- A comparison between the penalty contact and the kinematic method can be performed on the validated wedge model.
- Once the issues encountered in the current work can be solved, the 3D simulation of the fiber reinforced composite sonar dome can be performed. In the framework of the SUCCESS project, the major objective of such simulations is to obtain the strain field of the composite structure. This numerical model will be use as a preliminary study in preparation for the future slamming experimental tests.
- Implementation of the composite material model MAT054 on the wedge. The numerical simulation can be compared against experimental and numerical results obtained respectively in Stenius et. al (2013) [29] and Hassoon et. al (2017) [22].

11. Acknowledgements

Firstly, I would like to express my gratitude to professor Hervé Le Sourne, from ICAM. It was a pleasure to work under his supervision, being guided and supported with great care and cordiality. It really is an honour to have learned so much from your experience and knowledge. I am also very grateful to Yeye, Ph.D. student at the ICAM/GeM Institute, who always had the patience and generosity to help with whatever problem or question I encountered. I see a great future ahead of you.

I would also like to thank Jean Christophe Petiteau and Alexis Bloch, who cordially assisted me on my internship in Méca. It was a great experience to work with such highly prepared professionals.

Throughout this academic trajectory so full of learning that was the EMSHIP program, I've crossed the path of a number of persons that shared not only technical knowledge on Naval Architecture, but also life experiences. I thank professor Rigo and all the staff of the EMSHIP for all the hard work invested on this excellent program. Professor Kaeding and Thomas Lindemann, from the University of Rostock, thank you so much for all the kind assistance. A very special thank you goes to all my colleagues from the M120. You are true warriors and I sincerely admire all of you.

For all the friends, the old and the new ones, even though you are spread all over the world, I carry you wherever I go. You make everything lighter. I've lost count of how many different couches I've occupied in these last two years of nomadic life. It's amazing to have all these brothers and sisters all over. I am so lucky.

Finally, I am very grateful for the support of my beloved family, unconditionally present through joy and hardship. To my father, eternal admiration for your integrity, generosity and dedication. You've taught me that the search for perfection brings meaning to existence. To my mother, you're the strongest being on Earth. No more needed. To my brother, you've become such an amazing individual. I feel very lucky to walk by your side. Without you three none of this would be possible.

Icaro Ladeira

References

[1] Bereznitski A. “Slamming: the role of hydroelasticity”. In: *International Shipbuilding Progress* 48.4 (2001), pp. 333–351.

[2] Bergan A., Dávila C., Leone Frank., Awerbuch J., and Tan T. “A Mode I cohesive law characterization procedure for through-the-thickness crack propagation in composite laminates”. In: *Composites Part B: Engineering* 94 (2016), pp. 338–349.

[3] Cherniaev A., Butcher C., and Montesano J. “Predicting the axial crush response of CFRP tubes using three damage-based constitutive models”. In: *Thin-Walled Structures* 129 (2018), pp. 349–364.

[4] Kamath A., Bihs H., and Arnsten O. A. “Study of Water Impact and Entry of a Free Falling Wedge Using CFD Simulations”. In: *ASME 2016 35th International Conference on Ocean, Offshore and Arctic Engineering*. American Society of Mechanical Engineers. 2016, V002T08A020–V002T08A020.

[5] Korobkin A. “Analytical models of water impact”. In: *European Journal of Applied Mathematics* 15.6 (2004), pp. 821–838.

[6] Tassin A. “These de Doctorat de l’Université de Bretagne Occidentale (Doctoral dissertation, Université de Bretagne Occidentale)”. PhD thesis. Citeseer, 2011.

[7] Tassin A., Jacques N., El Malki Alaoui A., Nême A., and Leblé B. “Hydrodynamic loads during water impact of three-dimensional solids: modelling and experiments”. In: *Journal of Fluids and Structures* 28 (2012), pp. 211–231.

[8] Donguy B., Peseux B., and Fontaine E. “Numerical and experimental investigations of a rigid cone striking the free surface of an incompressible fluid”. In: *ASME Pressure Vessel and Piping Conference*. 2001.

[9] Laney C. B. *Computational gasdynamics*. Cambridge university press, 1998.

[10] Peseux B., Gornet L., and Donguy B. “Hydrodynamic impact: numerical and experimental investigations”. In: *Journal of Fluids and Structures* 21.3 (2005), pp. 277–303.

[11] Wade B., Feraboli P., and Osborne M. “Simulating laminated composites using LS-DYNA material model MAT54 part I:[0] and [90] ply single-element investigation”. In: *FAA JAMS: Baltimore, MD, USA* (2012).

[12] Wu B., Chen Z., Zhang X., Liu Y., and Lian Y. “Coupled Shell-Material Point Method for Bird Strike Simulation”. In: *Acta Mechanica Solida Sinica* 31.1 (2018), pp. 1–18.

[13] Campbell F. C. *Structural composite materials*. ASM international, 2010.

[14] Smith C. and Stojko S. "The application of fluid structure interaction techniques within finite element analyses of water-filled transport flasks". In: *Packaging, Transport, Storage & Security of Radioactive Material* 15.3-4 (2004), pp. 231–238.

[15] Livermore Software Technology Corporation. *LS-DYNA Theory Manual*. 2006.

[16] Bae D. and Zakki A. F. "Comparisons of multi material ALE and single material ALE in LS-DYNA for estimation of acceleration response of free-fall lifeboat". In: *Journal of the Society of Naval Architects of Korea* 48.6 (2011), pp. 552–559.

[17] Gay D. *Composite materials: design and applications*. CRC press, 2014.

[18] Howison S. D., Ockendon J. R., and Wilson S. K. "Incompressible water-entry problems at small deadrise angles". In: *Journal of Fluid Mechanics* 222 (1991), pp. 215–230.

[19] Jackson K. E., Littell J. D., and Fasanella E. L. "Simulating the Impact Response of Composite Airframe Components". In: (2014).

[20] Yettou E., Desrochers A., and Champoux Y. "Experimental study on the water impact of a symmetrical wedge". In: *Fluid Dynamics Research* 38.1 (2006), p. 47.

[21] Paris F and Jackson K. E. "A study of failure criteria of fibrous composite materials". In: (2001).

[22] Hassoon O. H., Tarfaoui M., and El Moumen A. "Progressive damage modeling in laminate composites under slamming impact water for naval applications". In: *Composite Structures* 167 (2017), pp. 178–190.

[23] Le Sourne H., Couty N., Besnier F., Kammerer C., and Legavre H. "LS-DYNA applications in shipbuilding". In: *4th European LS-DYNA users conference*. 2003, pp. 1–16.

[24] Luo H., Wang S., and Guedes Soares C. "Numerical prediction of slamming loads on a rigid wedge subjected to water entry using an explicit finite element method". In: *Advances in marine structures* (2011), pp. 41–47.

[25] Wagner H. "Über Stoß-und Gleitvorgänge an der Oberfläche von Flüssigkeiten". In: *ZAMM-Journal of Applied Mathematics and Mechanics/Zeitschrift für Angewandte Mathematik und Mechanik* 12.4 (1932), pp. 193–215.

[26] Stenius I. "Finite element modelling of hydroelasticity in hull-water impacts". PhD thesis. KTH, 2006.

[27] Stenius I. and Rosén A. "FE-Modelling of Hydrodynamic Hull-Water Impact Loads". In: *6th European LS-DYNA Users' Conference, Gothenburg, Sweden*. Citeseer. 2007.

[28] Stenius I., Rosén A., and Kuttenkeuler J. "Explicit FE-modelling of fluid–structure interaction in hull–water impacts". In: *International Shipbuilding Progress* 53.2 (2006), pp. 103–121.

[29] Stenius I., Rosén A., Battley M., and Allen T. "Experimental hydroelastic characterization of slamming loaded marine panels". In: *Ocean Engineering* 74 (2013), pp. 1–15.

[30] Watanabe I. "Analytical expression of hydrodynamic impact pressure by matched asymptotic expansion technique". In: *Transactions of the West-Japan Society of Naval Architects 71*. The Japan Society of Naval Architects and Naval Engineers. 1986, pp. 77–85.

[31] Barbero E. J. *Introduction to composite materials design*. CRC press, 2017.

[32] Day J. *Guidelines for ALE modelling in LS-DYNA (draft)*. Tech. rep. Technical report, LSTC, 2010.

[33] Huera-Huarte F. J., Jeon D., and Gharib M. "Experimental investigation of water slamming loads on panels". In: *Ocean Engineering* 38.11-12 (2011), pp. 1347–1355.

[34] Kvalsvold J. and Faltinsen O. "Hydroelastic modelling of slamming against wetdecks". In: *8th Intern. Workshop on Water Waves and Floating Bodies, Saint Johns, Canada*. 1993.

[35] Lavroff J., Davis M. R., Holloway D. S., and Thomas G. A. "Slamming of high-speed catamarans in severe sea conditions investigated by hydroelastic segmented model experiments". In: *Symposium on Naval Hydrodynamics*. 2010, pp. 1–12.

[36] Kapsenberg G. K. "Slamming of ships: where are we now?" In: *Philosophical Transactions of the Royal Society A: Mathematical, Physical and Engineering Sciences* 369.1947 (2011), pp. 2892–2919.

[37] Kapsenberg G. K., Van't Veer A. P., Hackett J. P., and Levadou M. M. D. "Aftbody slamming and whipping loads". In: *Transactions-Society of Naval Architects and Marine Engineers* 111 (2003), pp. 213–231.

[38] Ochi M. K. and Motter L. E. "Prediction of slamming characteristics and hull responses for ship design". In: (1973).

[39] Bisplinghoff R. L. and Doherty C. S. "Some studies of the impact of vee wedges on a water surface". In: *Journal of the Franklin Institute* 253.6 (1952), pp. 547–561.

[40] Chuang S. L. *Investigation of impact of rigid and elastic bodies with water*. Tech. rep. David W. Taylor Naval Ship Research and Development Center, Bethesda MD, 1970.

[41] Chuang S. L. *Slamming of rigid wedge-shaped bodies with various deadrise angles*. Tech. rep. David Taylor Model Basin Washington DC, 1966.

[42] Olovsson L. "LS-DYNA Training Class in ALE and Fluid-Structure Interaction". LSTC training-class course hand-outs. Linköping, Sweden, 2003.

[43] Vincent L., Xiao T., Yohann D., Jung S., and Kanso E. "Dynamics of water entry". In: *Journal of Fluid Mechanics* 846 (2018), pp. 508–535.

[44] LSTC. "LS-DYNA Keyword User's Manual". In: *Livermore: Livermore Software Technology Corporation (LSTC)* (2007).

[45] Andersson M. and Liedberg P. "Crash behavior of composite structures". In: *Master's Thesis in Applied Mechanics, Department of Applied Mechanics, Division of Material and Computational Mechanics, Chalmers University of Technology, Goteborg, Sweden* (2014).

[46] Faltinsen O. M. *Hydrodynamics of high-speed marine vehicles*. Cambridge university press, 2005.

[47] Faltinsen O. M. "Hydroelastic slamming". In: *Journal of Marine Science and Technology* 5.2 (2000), pp. 49–65.

[48] Faltinsen O. M. "Slamming". In: *Encyclopedia of Maritime and Offshore Engineering* (2017), pp. 1–12.

[49] Faltinsen O. M., Kvålsvold J., and Aarsnes J. V. "Wave impact on a horizontal elastic plate". In: *Journal of Marine Science and Technology* 2.2 (1997), pp. 87–100.

[50] Farsi M. and Ghadimi P. "Simulation of 2D symmetry and asymmetry wedge water entry by smoothed particle hydrodynamics method". In: *Journal of the Brazilian Society of Mechanical Sciences and Engineering* 37.3 (2015), pp. 821–835.

[51] Galal M. *Intoduction to Composite Modelling in LS-DYNA*. Last accessed 16 September 2017. 2018.

[52] Guida M., Moccia A., and Marulo F. *Study, Design and Testing of Structural, Configurations for the Bird-strike Compliance of Aeronautical Components*. CUEN, 2008.

[53] Osborne M. "Single-element characterization of the LS-DYNA MAT54 material model". PhD thesis. 2013.

[54] Scolan Y. M. and Korobkin A. A. "Three-dimensional theory of water impact. Part 1. Inverse Wagner problem". In: *Journal of Fluid Mechanics* 440 (2001), pp. 293–326.

[55] Souli M. and Benson D. J. *Arbitrary Lagrangian Eulerian and fluid-structure interaction: numerical simulation*. John Wiley & Sons, 2013.

[56] Tenzer M., Moctar O., and Schellin T. E. "Experimental investigation of impact loads during water entry". In: *Ship Technology Research* 62.1 (2015), pp. 47–59.

[57] Vezina M. and Firoozrai A. "Drop Test into Water and Wave Impact Simulations of a Novel 7-Meter Plastic Boat with LS-DYNA". In: *11th International LS-DYNA Users' Conference, Dearborn, MI, USA*. 2010.

[58] Aquelet N. "Modélisation de l'impact hydrodynamique par un couplage fluide-structure". In: *Villeneuve d'Ascq, France* (2004).

[59] Aquelet N. and Souli M. "ALE Incompressible Fluid in LS-DYNA®". In: *FSI/ALE* 21 (2012).

[60] Aquelet N. and Souli M. "Damping effect in fluid-structure interaction: Application to slamming problem". In: *ASME 2003 Pressure Vessels and Piping Conference*. American Society of Mechanical Engineers. 2003, pp. 175–184.

[61] Aquelet N., Souli M., and Olovsson L. "Euler-Lagrange coupling with damping effects: Application to slamming problems". In: *Computer methods in applied mechanics and engineering* 195.1-3 (2006), pp. 110–132.

[62] Marine Nationale. *Le MSC Napoli échoué à Lyme Bay*. 2007. URL: `https://www.meretmarine.com` (visited on 07/02/2019).

[63] Faltinsen O. *Sea loads on ships and offshore structures*. Vol. 1. Cambridge university press, 1993.

[64] Feraboli P., Wade B., Deleo F., Rassaian M., Higgins M., and Byar A. "LS-DYNA MAT54 modeling of the axial crushing of a composite tape sinusoidal specimen". In: *Composites Part A: Applied Science and Manufacturing* 42.11 (2011), pp. 1809–1825.

[65] Ghadimi P., Feizi C., Mohammad A., and Dashtimanesh A. "A numerical investigation of the water impact of an arbitrary bow section". In: *ISH Journal of Hydraulic Engineering* 19.3 (2013), pp. 186–195.

[66] Cointe R. "Two-dimensional water-solid impact". In: *Journal of Offshore Mechanics and Arctic Engineering* 111.2 (1989), pp. 109–114.

[67] Hedayati R. and Sadighi M. *Bird strike: an experimental, theoretical and numerical investigation*. Woodhead Publishing, 2015.

[68] Hedayati R. and Ziaei-Rad S. "A new bird model and the effect of bird geometry in impacts from various orientations". In: *Aerospace Science and Technology* 28.1 (2013), pp. 9–20.

[69] Messahel R. and Souli M. "SPH and ALE formulations for fluid structure coupling". In: *CMES: Computer Modeling in Engineering & Sciences* 96.6 (2013), pp. 435–455.

[70] Panciroli R., Pagliaroli T., and Minak G. "On Air-Cavity Formation during Water Entry of Flexible Wedges". In: *Journal of Marine Science and Engineering* 6.4 (2018), p. 155.

[71] Zhao R. and Faltinsen O. "Water entry of two-dimensional bodies". In: *Journal of Fluid Mechanics* 246 (1993), pp. 593–612.

[72] Zhao R., Faltinsen O., and Aarsnes J. "Water entry of arbitrary two-dimensional sections with and without flow separation". In: *Proceedings of the 21st symposium on naval hydrodynamics*. (Trondheim, Norway, 1996). , Washington, DC, USA: National Academy Press, pp. 408–423.

[73] Hwang S., Khayyer A., Gotoh H., and Park J. C. "Simulations of incompressible fluid flow-elastic structure interactions by a coupled fully Lagrangian solver". In: *The Twenty-fifth International Ocean and Polar Engineering Conference*. International Society of Offshore and Polar Engineers. 2015.

[74] Okada S. and Sumi Y. "On the water impact and elastic response of a flat plate at small impact angles". In: *Journal of marine science and technology* 5.1 (2000), pp. 31–39.

[75] Selvaraju S. and Ilaiyavel S. "Applications of composites in marine industry". In: *J. Eng. Res. Stud., II* (2011), pp. 89–91.

[76] Vepa K. S., Van Nuffel D., and Van Paepegem W. "Pressure predictions during water entry of a 2D rigid cylinder using SPH method". In: *26th International Workshop on Water Waves and Floating Bodies (IWWWFB)*. 2011, pp. 197–200.

[77] Belytschko T. and Neal M. O. "Contact-impact by the pinball algorithm with penalty and Lagrangian methods". In: *International Journal for Numerical Methods in Engineering* 31.3 (1991), pp. 547–572.

[78] Tveitnes T., Fairlie-Clarke A. C., and Varyani K. "An experimental investigation into the constant velocity water entry of wedge-shaped sections". In: *Ocean Engineering* 35.14-15 (2008), pp. 1463–1478.

[79] Von Karman T. "The impact on seaplane floats during landing". In: (1929).

[80] Photographer unknown. *Photo ID: DN-SD-05-00213*. 2004. URL: `http://www.navsource.org/archives/04/1163/040163.htm` (visited on 06/25/2019).

[81] Logvinovich G. V. *Hydrodynamics of flows with free boundaries*. 1969.

[82] Mei X., Liu Y., and Yue D. K. "On the water impact of general two-dimensional sections". In: *Applied Ocean Research* 21.1 (1999), pp. 1–15.

[83] Chen N. Z., Sun H. H., and Soares C. G. "Reliability analysis of a ship hull in composite material". In: *Composite structures* 62.1 (2003), pp. 59–66.

[84] Yu Z., Amdahl J., Greco M., and Xu H. "Hydro-plastic response of beams and stiffened panels subjected to extreme water slamming at small impact angles, part II: Numerical verification and analysis". In: *Marine Structures* 65 (2019), pp. 114–133.

Appendices

A. Wedge with Low Deadrise Angle

Results on the influence of the penalty contact parameters on the vertical slamming force for a 5° wedge are presented in Fig. 81.

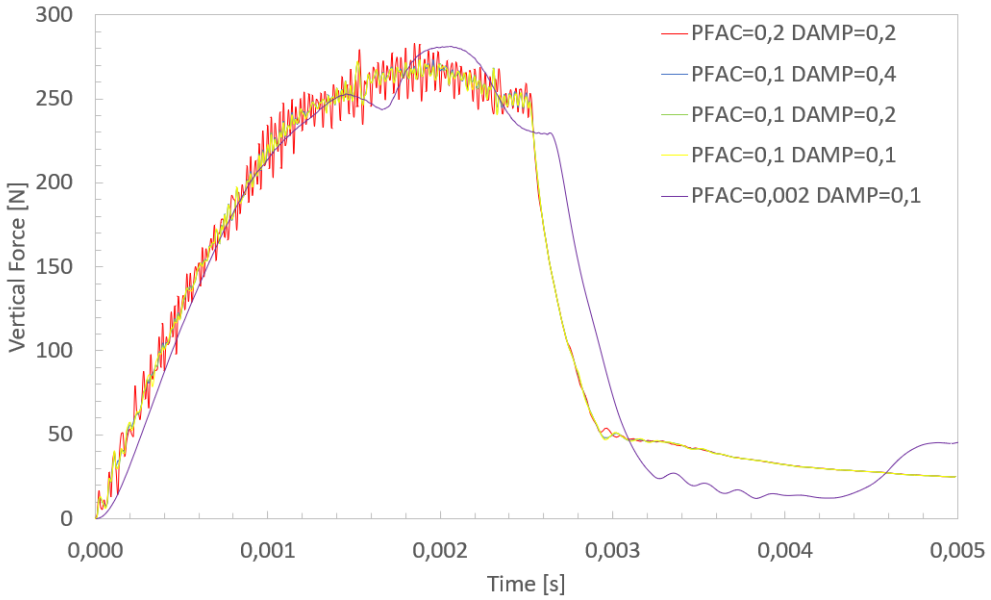

Figure 81: Sensitivity analysis of the penalty contact parameters for a 5° wedge.

B. Prescribed Constant Velocity and Initial Velocity

A comparison of the slamming force for an applied prescribed constant velocity and an initial velocity in a 30° wedge is shown in Fig. 82.

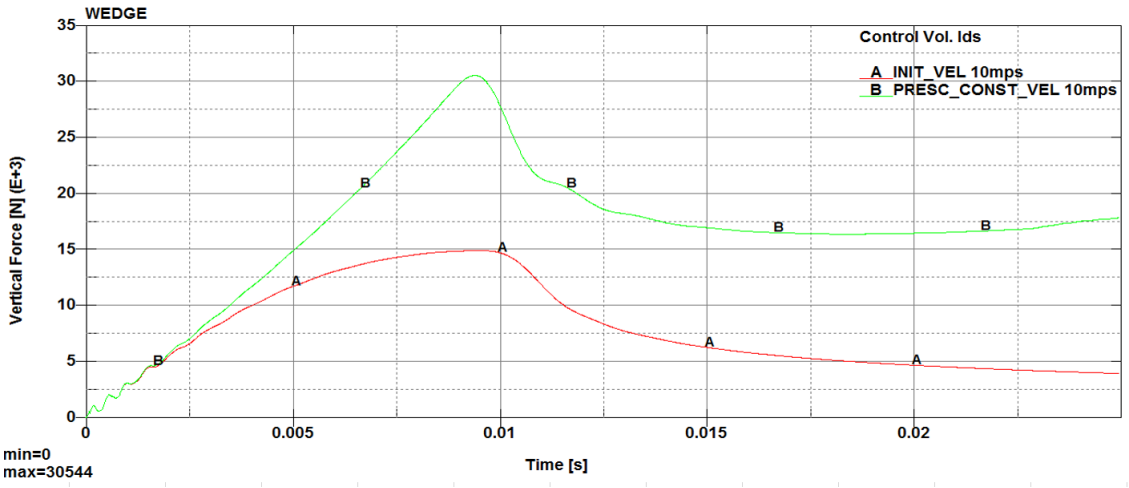

Figure 82: Comparison of applied prescribed constant velocity and initial velocity in a 30° wedge.

C. Properties of the composite laminate

Table 17: Properties of the matrix (Epoxy).

Physical properties at 23°C		
Density	1200	kg/m^3
Glass transition temperature	120	°C
Thermal expansion	68	µm/m/°C
Thermal conductivity	0,20	W/m/°C

Stiffness		
Young modulus	3200	MPa
Poisson ratio	0,37	

Strength		
Tensile	74,4	MPa
Compressive	126,5	MPa
Shear	43,0	MPa

Table 18: Properties of the fiber (E-Glass).

Density		
Density	2540	kg/m3
Thermal expansion	5,30	µm/m/°C
Transverse thermal expansion	5,30	µm/m/°C
Thermal conductivity	1,05	W/m/°C
Transverse thermal conductivity	1,05	W/m/°C

Stiffness		
Axial Young modulus	73000	MPa
Axial Poisson ratio	0,22	
Transverse Young modulus	73000	MPa
Transverse Poisson ratio	0,22	
Axial shear modulus	29900	MPa
Transverse shear modulus	29900	MPa

Strength		
Tensile	1916	MPa
Compressive	1155	MPa
Shear	1155	MPa

Table 19: Properties of the ply.

Volumetric properties		
Volume fiber fraction	44,1%	
Density	1779	kg/m^3
Thickness for 100g/m²	0,089	mm

Stiffness		
Young Modulus X	33974	MPa
Young Modulus Y	9286	MPa
Young Modulus Z	9286	MPa
Shear Modulus XY	2779	MPa
Shear Modulus XZ	2779	MPa
Shear Modulus YZ	3295	MPa
Poisson Ratio XY	0,300	
Poisson ratio XZ	0,300	
Poisson Ratio YZ	0,409	

Strength		
Tensile strength X	891,7	MPa
Compressive strength X	579,2	MPa
Tensile strength Y	55,9	MPa
Compressive strength Y	95,1	MPa
Tensile strength Z	55,9	MPa
Compressive strength Z	95,1	MPa
Shear strength XY	32,2	MPa
Shear strength XZ	32,2	MPa
Shear strength YZ	32,2	MPa

Table 20: Stack-up sequence of the laminate.

Id	Ply	Angle	Weight	Thickness
-	-	°	g/m^2	mm
1	UD_E-Glass_Epoxy	0	700	0,624
2	UD_E-Glass_Epoxy	90	700	0,624
3	UD_E-Glass_Epoxy	0	700	0,624
4	UD_E-Glass_Epoxy	90	700	0,624
5	UD_E-Glass_Epoxy	0	700	0,624
6	UD_E-Glass_Epoxy	90	700	0,624
7	UD_E-Glass_Epoxy	0	700	0,624
8	UD_E-Glass_Epoxy	90	700	0,624
9	UD_E-Glass_Epoxy	0	700	0,624
10	UD_E-Glass_Epoxy	90	700	0,624
11	UD_E-Glass_Epoxy	0	700	0,624
12	UD_E-Glass_Epoxy	90	700	0,624
13	UD_E-Glass_Epoxy	0	700	0,624
14	UD_E-Glass_Epoxy	90	700	0,624
15	UD_E-Glass_Epoxy	0	700	0,624
16	UD_E-Glass_Epoxy	90	700	0,624
17	UD_E-Glass_Epoxy	0	700	0,624
18	UD_E-Glass_Epoxy	90	700	0,624
19	UD_E-Glass_Epoxy	0	700	0,624
20	UD_E-Glass_Epoxy	90	700	0,624
21	UD_E-Glass_Epoxy	0	700	0,624
22	UD_E-Glass_Epoxy	90	700	0,624
23	UD_E-Glass_Epoxy	0	700	0,624
24	UD_E-Glass_Epoxy	90	700	0,624
25	UD_E-Glass_Epoxy	0	700	0,624
26	UD_E-Glass_Epoxy	90	700	0,624
27	UD_E-Glass_Epoxy	0	700	0,624
28	UD_E-Glass_Epoxy	90	700	0,624
29	UD_E-Glass_Epoxy	0	700	0,624
30	UD_E-Glass_Epoxy	90	700	0,624
31	UD_E-Glass_Epoxy	0	700	0,624
32	UD_E-Glass_Epoxy	90	700	0,624
				19,98

Table 21: Properties of the laminate.

Volumetric properties		
Area density	35556	g/m^2
Thickness	19,98	mm

In-plane stiffness		
Young Modulus X	21787	MPa
Young Modulus Y	21787	MPa
Shear Modulus XY	2779	MPa
Poisson Ratio XY	0,129	

Flexural stiffness		
Young Modulus X	21787	MPa
Young Modulus Y	21787	MPa
Shear Modulus XY	2779	MPa
Poisson Ratio XY	0,129	

In-plane strength		
Tensile strength X	125	MPa
Compressive strength X	213	MPa
Tensile strength Y	125	MPa
Compressive strength Y	213	MPa
Shear strength XY	32	MPa

Flexural strength		
Tensile strength X	129	MPa
Compressive strength X	143	MPa
Tensile strength Y	143	MPa
Compressive strength Y	129	MPa
Shear strength XY	32	MPa

D. Results for the 2D Full Size Elasto-plastic Parabola Model

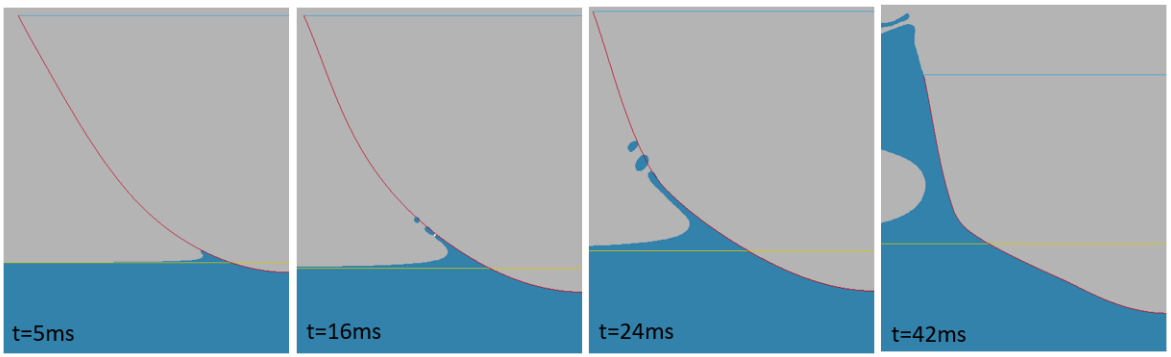

Figure 83: Development of the free surface for the water entry of an elasto-plastic parabola. The deformation of the structure can be observed.

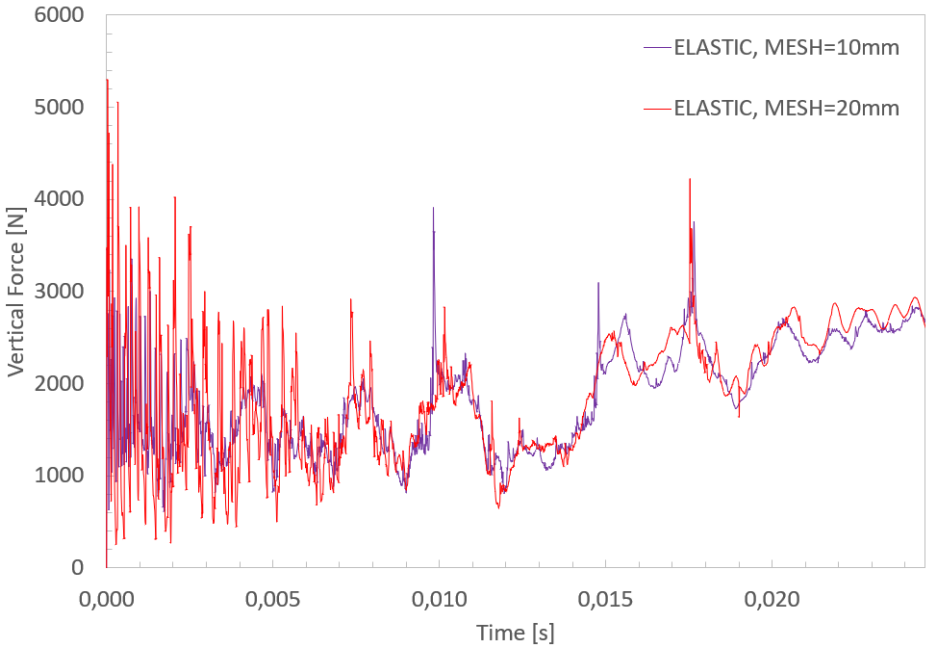

Figure 84: Vertical slamming force obtained for the elasto-plastic parabola. Two different mesh sizes were applied.